Direct X-Ray Studies of Epitaxial Semiconductor Quantum Dots

by

Divine Philip Kumah

A dissertation submitted in partial fulfillment
of the requirements for the degree of
Doctor of Philosophy
(Applied Physics)
in The University of Michigan
2009

Doctoral Committee:

Professor Roy Clarke, Chair
Professor Jasprit Singh
Associate Professor Cagliyan Kurdak
Associate Professor Joanna Mirecki-Millunchik
Associate Professor David Reis

To Meme, Sue, Paulina, Angela and Samuel.

ACKNOWLEDGEMENTS

First of all I would like to thank God for his gracious guidance and wisdom.

My heartfelt thanks goes to my advisor, Roy Clarke, for his guidance and financial support through my time here at Michigan. I would also like to thank my thesis committee for their advise and guidance with my dissertation. I would also like to thank my labmates Dr Codrin Cionca and Naji Husseini for making my experience fun and exciting. I would like to thank Brad Orr, Charles Sutton and Cyndia Macnabb and the rest of the Applied Physics program for their support.

I would also like to extend my gratitude to Yizhak Yacoby at the Hebrew University for his kind help and advise.

Life as a doctoral student has been bearable, thanks to the support of my friends and family. Thank you Erika, for being a part of this journey. A big thanks goes to Mama Jean, for having her door always open to me and countless other students who have passed through the department.

This work would not have been possible without the help of collaborators at the Advanced Photon Source(APS) and the Swiss Light Source(SLS). Thanks goes to Phil Willmott, Stephan Pauli, Matts Bjorck and Chris Schlepuetz at the SLS and Don Walko, Dohn Arms, Eric Dufresne, Paul Zschack and Zhan Zhang at the APS for their help and expertise in collecting data for this thesis.

TABLE OF CONTENTS

LIST OF TABLES

Table

LIST OF FIGURES

Figure

ABSTRACT

Quantum dots have sparked a remarkable amount of interest in device development and the understanding of fundamental laws of nature. The peculiar properties of quantum dots arise from the confinement of charge carriers in three dimensions resulting in discrete energy states. Using the coherent Bragg Rod Analysis x-ray phase retrieval technique, electron density maps obtained close to the x-ray absorption edges of the constituent elements are compared to directly determine the morphology and the atomic structure and composition of the systems studied. Results on ultrathin layers of nominal GaAs on InGaAs show how an interplay between surface coarsening and chemical intermixing lead to a relaxation of strain from the nominal 3.7% tensile misfit strain. The strain is found to increase continuously from the interface, where most of the strain is relieved due to Indium incorporation into the GaAs film, to a maximum at the top of the film of 0.7%($T_{deposition}(GaAs)$=480^o C) and 1.0%($T_{deposition}(GaAs)$=520^o C). The structure of uncapped epitaxial InAs quantum dots grown using the Stranski-Krastanow method on GaAs(001) reveal that the dots contain significant amounts of Ga with the Ga concentration decreasing from 50% at the base of the dots to 0% at the top of the dots. A contraction of the out-of-plane lattice constant at the dot-substrate interface to about 3.5 Å is observed. The out-of-plane lattice spacing in the dot region is found to be GaAs-like. It is inferred from the folded structure that the atomic planes are curved to partially relax strain with the most relaxation occurring at the top of the dots. The nominal

InSb dots grown on GaAs(001) using the droplet heteroepitaxy method are found to contain very little Indium resulting in dots that have a GaAs core with an outer GaSb shell. A vertical stacking shift is observed in the dots relative to the substrate structure. The dot structure is shown to extend about 2 nm below the substrate surface. The advantage of the characterization technique developed here is that it provides a direct quantitative non-invasive determination of the three-dimensional structure and composition of epitaxial systems with atomic-scale resolution.

CHAPTER I

Introduction

1.1 Introduction and Motivation for Project

Novel technologically important systems usually consist of layers of different crystalline materials with thicknesses as low as a few atomic layers. The applications of these ultra-thin systems range from medical diagnostic tools to information storage and high speed data processing to high efficiency solar cells.

The miniaturization of devices not only leads to improved device performance but has also led to the discovery of new and exciting electronic, magnetic, optical and mechanical phenomena. These effects observed in nanoscale systems stem from the fact that the properties of the materials comprising them vary remarkably from their bulk properties when their dimensions are reduced. Due to the amplified effects of structural distortions, so called meta-materials emerge when the dimensions of these systems are on the order of the nano-scale in one or more dimensions. The properties of these systems are determined to a large extent, by the structure of the surfaces and interfaces present where effects such as strain relaxation and preferential atomic segregation may lead to alterations in composition and the positions of atoms from their nominal bulk values.

Low dimensional systems require precise atomic scale growth control. The art of

growing nanoscale heterostructures using growth techniques such as Molecular Beam Epitaxy (MBE), Metal-organic Chemical Vapor Deposition (MOCVD) and Pulsed Laser Deposition (PLD) has developed tremendously over the past two decades.

The need to develop non-destructive techniques to characterize these systems cannot be over-emphasized. Growers need to know the optimum growth parameters that would be required to produce these structures with the highest quality. From the point of view of fundamental sciences, characterizing these novel structures provides information vital to the understanding of both microstructural growth and the unique and novel properties these systems exhibit.

While much research attention has been focused on a wide range of nanoscale systems recently, many details about their growth and physical properties are not very well understood, particularly, how the interplay between strain relaxation and chemical segregation affect the final states of these systems. This study is focused on solving the structure of a novel technologically important class of systems: epitaxial, semiconductor quantum dots. Here 'epitaxial' refers to a surface structure in which the atoms are in coherent registry with the supporting substrate.

1.1.1 Quantum Dots

Quantum dots (QDs), also known as artificial atoms, are of scientific and technological interest because of their fully quantized electronic states, high radiative efficiencies, tunable band gaps and their near zero dimensional properties [1, 2]. Their opto-electronic properties may be tuned by varying the shape, size and composition of the dots.

From a device point of view, they have numerous benefits because they can be manufactured as buried structures in thin film semiconductor devices. Devices have

been either proposed or fabricated involving single dots as in the case of two-level systems for quantum computing[3, 4], single electron transistors (SETs) [5, 6] and single photon sources[7, 8]. Collectively, ensembles of QD's have been successfully used in the development of mid-infrared detectors, semiconductor lasers[9, 10, 11] and solar cells[12, 13, 14] due to the low threshold currents, low temperature sensitivity of their threshold current and high differential quantum efficiency.

The electronic structure of QDs are directly related to their shape and sizes. The dimensions of QD's are less than the electron (or hole) deBroglie wavelength of the material from which they are made. In the case of InGaAs with a deBroglie wavelength of about 50 nm, the QD's have been observed to have widths on the order of 20 nm and heights on the order of 5 nm. The shapes of these dots may be lenticular, conical, truncated conical, pyramidal or truncated pyramidal depending on the growth conditions. QD's are usually capped to prevent contamination and oxidation. The presence of a capping layer affects the composition and shape of the dots as well as the strain states within the dots[15].

Significant deviations from nominal compositions have been observed in both capped and free-standing quantum dot systems. Studies on the composition of nominally pure InAs dots on GaAs substrates [16, 17, 18, 19, 20] have shown a significant presence of Ga in the dots with In more concentrated in the the centers of the dots. The Ga in the dots comes from diffusion from the substrate. Atomic segregation and interdiffusion are strongly dependent on the substrate temperature during the QD growth and the strain gradients in the vicinity of the dot. This non-uniformity in the composition of the dots leads not only to an effective reduction in the size of the quantum dots but also has a strong effect on the opto-electric and magnetic properties.

The alterations in the structure and composition observed in quantum dot structures are not peculiar to these systems. Similar modifications occur in a wide class of epitaxial systems and may be driven by strain, electrostatics, kinetics and thermodynamics which depend, to a large extent, on the growth conditions.

The mechanisms of these deviations are complex and not very well understood and the goal of this thesis is to provide a non-invasive direct structural characterization tool to study the internal structure and composition of the dots and their interfaces with sub-atomic resolution to provide a better understanding of how they form and how specific growth conditions affect the final structures of the dots.

Strain Relaxation and Self Assembled Quantum Dots

When thin films are epitaxially grown on a substrate, they may grow layer-by-layer as 2D planar films (Frank-van der Merwe (FM) growth mode)[21, 22] with no dislocations if the lattice mismatch with the substrate is small($< 1\%$ or so). In this situation, the film layers are strained such that the in-plane lattice constant is the same as the substrate. Below a critical thickness, the film remains pseudomorphic with a homogeneous distribution of strain. When the critical thickness is exceeded, strain may be partially or fully relaxed by the formation of misfit dislocations.

A second growth method called the Volmer-Weber (VW)[21, 23, 24] growth mode is possible for high lattice mismatched films where the deposited atoms prefer to stick to each other rather than to the crystal surface on which they are deposited due to the high strain energy. In this mode, 3D islands form on the onset of film deposition to minimize surface and interfacial energy.

For films with intermediate lattice mismatches, a different growth mode called the Stranski-Krastanow (SK) growth mode may occur. SK growth involves the

spontaneous formation of 3D islands to relieve strain energy when a critical 2D film thickness is attained with or without the formation of dislocations to accommodate strain. SK growth lies between 2D and 3D film growth. The critical thickness where the 2D to 3D transition occurs depends on the lattice mismatch and chemical potentials of the deposited atoms.

Under the right growth conditions, the 3D islands in the SK growth mode form quantum dots since their dimensions are on the order of tens of nanometers and they are usually accompanied by a highly strained thin wetting layer(WL) of the grown film between the dots and the substrates.

Intermixing can occur during the deposition of the wetting layer before the dots form, and thus reduces the effective mismatch which forms the basis of the theory of SK growth[20]. Furthermore, the total volume of the dots grown has been found to be greater than the amount of deposited material further evidencing that the current SK model is too simplistic to correctly model the growth of self-assembled dots.

Droplet Heteroepitaxy III-V Quantum Dots

The Droplet Heteroepitaxial (DHE) [25, 26] technique provides an alternate way to grow QDs. The DHE method involves the deposition of metal group III liquid droplets on a substrate surface followed by the subsequent exposure of the liquid droplets to a flux of Group V atoms resulting in the formation of high quality crystalline dots. The DHE method extends the type of epitaxial dots which can be grown to lattice-matched systems such as InAs dots on GaSb substrates. The DHE method also permits the growth of dots without the presence of a wetting layer [26] which has been shown to affect the optical properties of QD systems. The technique also makes it possible to place the dots in well defined positions since it is possible to

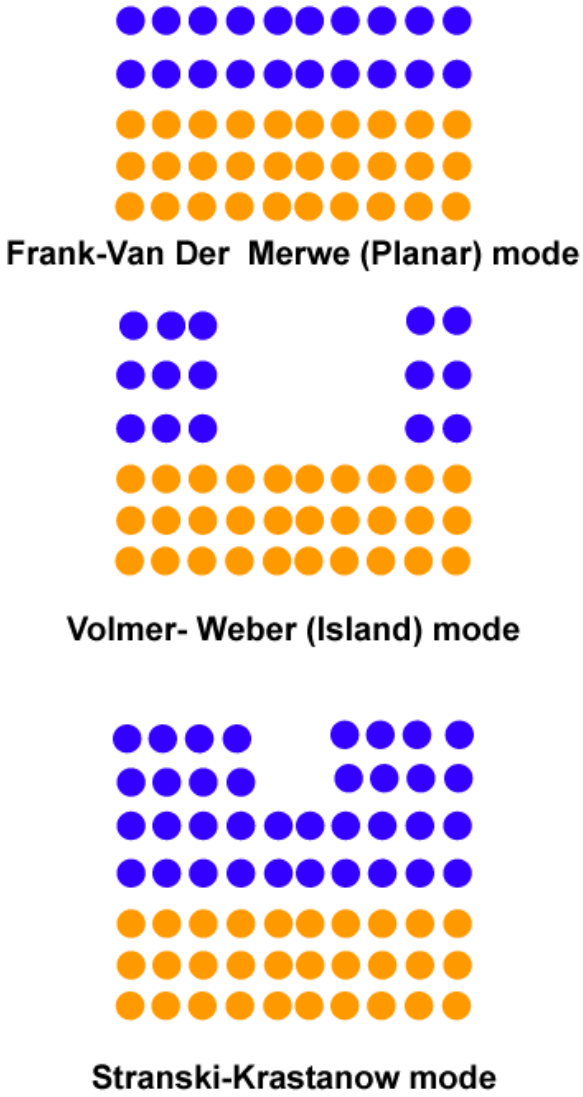

Figure 1.1: Illustration of epitaxial film growth modes.

control where the droplets are placed. For example, the surface can be patterned by lithography to define locations where droplets will form.

1.1.2 Probing the Structure of Nanoscale systems

A major experimental goal is to be able to determine the final structures of nanoscale systems either by imaging them directly or by indirectly studying their physical effects.

The traditional techniques for studying the structural properties of surface and

buried nanostructures include in-situ techniques such as Reflection High Energy Electron Diffraction (RHEED) and Scanning Tunnelling Microscopy(STM) and ex-situ methods such as Atomic Force Microscopy (AFM), Transmission Electron Microscopy(TEM) and Small Angle X-ray diffraction. RHEED and AFM are well suited for studying surface morphology and are not very effective for buried structures such as embedded QDs. Cross sectional STM is useful for studying buried interfaces but is limited to the study of cleavage planes. High Resolution TEM can image atomic arrangements, however, it is limited by sample preparation since thin sections ($\approx$10 nm) are required to allow electrons to penetrate the sample. Muller *et al.* [27] have used Electron Energy Loss Microscopy to provide atomic scale images of heterostructural interfaces to study chemical interdiffusion.

X-ray diffraction (XRD) characterization techniques are advantageous for studying buried structures due to the relatively larger penetration power of x-rays. The availability of third-generation synchrotron x-ray sources has opened new doors as far as the study of nanostructures are concerned. The high flux, and more importantly high brightness, available at synchrotron sources makes it possible to obtain appreciable diffraction signals from nanostructures with excellent signal to noise ratios and fast scan times.

The concurrent development of two-dimensional pixel array detectors such as the Pilatus 100K detector has considerably sped up the collection of reliable diffraction data. In comparison to point detectors which measure a single point in reciprocal space per measurement, 2D pixel array detectors provide access to large range in reciprocal space since each pixel effectively acts a as a point detector assuming it has a zero-point spread function (as is the case with the Pilatus 100K detector). Another benefit of using 2D detectors is that it permits a more accurate subtraction of the

background from the main diffracted signal of interest [28] .

The interpretation of diffraction data obtained by most x-ray methods usually requires the refinement of an initial model determined using *a-priori* knowledge about the system. In most situations where complex deviations from the nominal system may occur, it is difficult to determine rapidly the correct structure and one may not even arrive at the correct structure because of the large number of variables that need to be refined.

1.1.3 The X-Ray Phase Problem and the Coherent Bragg Rod Analysis Method

The limitations of XRD lies in the fact that the measured intensities only provide part of the information required to directly solve the structure of the system. To fully solve the structure of a given system from diffraction experiments recorded in reciprocal space, the phases and amplitude of a quantity called the complex structure factor (CSF) need to be known. The CSF provides the Fourier components of the real space structure, thus, a direct Fourier transform of the CSFs would give a real space image of the system.

Unfortunately, the measured diffraction intensities provide only the square of the amplitudes of CSFs and consequently, all phase information is lost.

The task of determining the phases of the CSF's is called the 'phase problem'. Various methods have been devised and they are generally referred to as "direct methods" in x-ray crystallography. The problem has largely been solved for 3D periodic crystals; however only recently has the 2D case been addressed. Such 2D systems, sometimes referred to as epitaxial heterostructures, are periodic in the plane of the substrate but aperiodic in the direction normal to the substrate. This leads to a special characteristic of the diffraction pattern: rather than a set of discrete

peaks arranged in a 3D periodic pattern, epitaxial materials show Bragg rods along which the scattered intensity is continuous. This has important implications for the determination of the phases of the CSFs.

One way to reconstruct the lost phases from measured intensities, and hence, solve the structure, is using the coherent Bragg rod analysis (COBRA) technique. The COBRA technique is a powerful model independent x-ray phase retrieval method which can be used to directly obtain three dimensional electron density maps of epitaxial or semi-epitaxial thin films [29] by extracting phase information from reciprocal space x-ray diffracted intensities sampled along substrate defined Bragg rods.

COBRA was first used to study the atomic structure of Gd_2O_3 grown on (100)GaAs by Yacoby et al[30, 29]. Gd_2O_3 is an excellent passivation oxide for GaAs. They found out that the Gd_2O_3 stacking order was different from the bulk and similar to the stacking order of the underlying substrate as shown in Figure 1.2.

Ferroelectricity in perovskites such as $PbTiO_3$ and $SrTiO_3$ have been also extensively studied using the COBRA method [31, 32] to determine domain structure and the atomic displacements which lead to polarization.

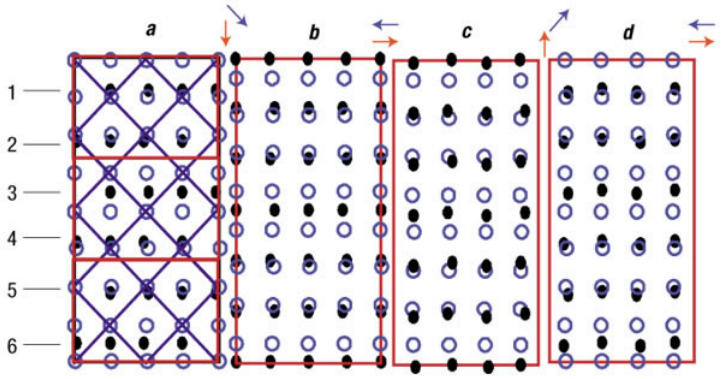

Figure 1.2: In-plane Gd positions (dots) in four consecutive layers of the Gd_2O_3 film. Each large rectangle represents one 2D super-cell composed of 3 Gd_2O_3 cells (red) and 16 GaAs cells (blue). The positions of the substrate Ga/As atoms (circles) in four consecutive layers are shown superimposed. [30]

Cionca et al. [33] have studied the composition at the interfaces of both the InAs film grown on GaSb(001) and GaSb grown on InAs(001) using COBRA as a first step to study III-V heterostructures and superlattices. By considering the sub-system close to the interface as a $Ga_mIn_{1-m}Sb_nAs_{1-n}$ quaternary, minimal segregation has been evidenced in InAs/GaSb(001); This sample was grown by MBE(molecular beam epitaxy) to have a greater degree of "GaAs-like" bonds at the interface with the GaSb substrate by depositing the InAs film under As(2) dimer concentration rather than the tetramer form of As, As(4). Significant In and As interdiffusion is seen in the GaSb/InAs(001) also with a high degree of "GaAs-like" bonds at the interface.

Interesting and new insights into the origins of the quasi-two dimensional electron gas at the interface between insulating $LaAlO_3$ and $SrTiO_3$[34] were obtained by directly solving the structure of the interface using COBRA. The COBRA analysis directly revealed that cationic intermixing at the interface resulted both in the dilation of the interface and the formation of metallic $La_{1-x}Sr_xTiO_3$.

Implementing the COBRA method for new systems such as quantum dots would hopefully result in helping us understand these systems in much more detail with sub-angstrom resolution.

Information Provided by COBRA

The 3D electron density map determined by COBRA provides the folded structure of the system, i.e., all the atoms in the system are folded laterally into a substrate-defined unit cell column using substrate defined unit cell vectors as shown in Fig 1.3. If an atom is in registry with the substrate unit cell, when folded, it would result in a well defined 3D Gaussian peak at the corresponding lattice point. If the atom has a different in-plane periodicity but is still commensurate with the substrate, the

folded structure would lead to a broadened peak localized at its average lattice site. Thus the folded structure can give useful information (e.g., in-plane lattice relaxation and reconstruction) even when the structure is not fully ordered. In the situation where an atom is disordered, its folded structure would lead to a constant delocalized electron density.

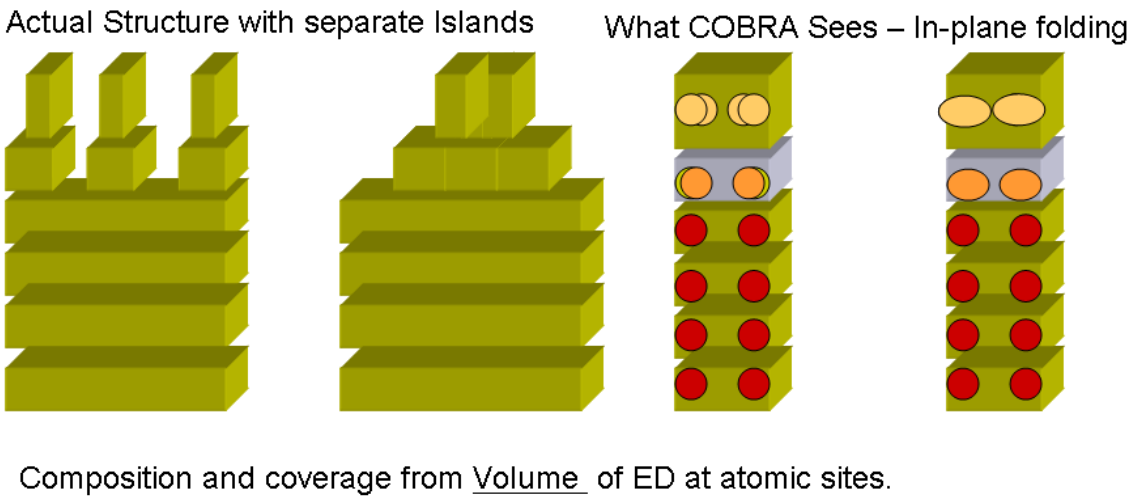

Figure 1.3: Illustration of folded structure provided by COBRA.

A three dimensional integration of the observed electron density peaks can be used to determine the composition. The integral of each peak corresponds to the effective number of electrons which scatter x-rays at that lattice point. The effective number of electrons depends on the x-ray wavelength and the relative amounts of atomic species occupying that point in the unit cell.

For example, Indium has an effective number of electrons of 49 at 10.365 keV while Gallium is 19 electrons at the same energy. For a 50-50 alloyed layer of In and Ga, the calculated integrated ED at the lattice points where In and Ga reside is $(49 * 0.5 + 19 * 0.5) = 34$ electrons. If the layer has a coverage of only 40%, then the calculated integrated ED becomes 13.6 electrons.

The layer coverage could be more or less than 100% if the layer is reconstructed or if the layer is not continuous. For systems in which no intermixing (alloying) occurs, it is a straightforward matter to determine the composition directly from the peak volume integral. However, when intermixing occurs, as in the case of QD's, and layers are not fully occupied due to island formation, it is not trivial to directly determine the composition of the system. Below, we show how to do this using the fact that the electron density peaks are strongly dependent on the x-ray energy, in the vicinity of the species-specific x-ray absorption edge. This approach is called "anomalous diffraction" or "resonant diffraction" and it was originally developed to aid in x-ray phase determination for 3D crystals (Multiple Anomalous Dispersion -MAD phasing)[35]. In principle, the lattice spacings may be used to derive the composition, however, this assumes the system is in equilibrium and that Vegard's law is valid i.e., there is a direct relationship between lattice spacings and composition.

1.1.4 An Anomalous Extension to COBRA

In this thesis, a more spectroscopic extension of the COBRA method is investigated to determine the composition of alloyed systems directly by taking into account the x-ray wavelength dependence of the effective number of electrons of a particular atomic species. The effective number of electrons of a given atom can vary by as much as 20% or more when the x-ray energy is set to be close to the absorption edge of the atom compared to when the energy is far away from the edge.

The hypothesis to be investigated in this thesis is that if electron maps are obtained close to and away from the absorption edges of one of the constituent elements, the differences in the maps would directly give the relative amounts of the different constituent elements. This deconvolution makes it possible to directly determine the

composition profiles and morphologies of non-planar systems such as quantum dots without having to rely solely on the measured lattice parameters. The strain profiles can then be more accurately determined by combining the independently determined composition and lattice spacing profiles.

1.2 Organization of Thesis

This thesis is organized as follows: The second chapter provides a background review of the current advances in the growth and characterization of self-assembled quantum dots, an introduction to the Coherent Bragg Rod Analysis technique and a review of some of the current results which have been obtained using this technique.

In chapter 3, the synchrotron experimental setup will be described.

In chapters 4 and 5 respectively, results obtained using the method described on ultrathin islands of GaAs/InGaAs and Stranksi-Krastanow InAs dots on GaAs substrates will be presented and discussed. In Chapter 6, results on InSb quantum dots grown by Droplet Heteroepitaxy would be presented. Finally, in chapter 7, the conclusions of this study and possible future directions will be outlined.

CHAPTER II

Background

2.1 X-ray diffraction

Diffraction from an atom

Classically, the total scattering cross section of an atom which interacts with an x-ray photon is given by

$$f^0(q) = \int \rho(\vec{r})_{atom} e^{i\vec{q}\cdot\vec{r}} d\vec{r} \tag{2.1}$$

where $\vec{q}$ is the wavevector transfer and $\rho_{atom}(\vec{r})$ is the a function representing the distribution of electrons in the atom. $f^0(q)$ is referred to as the atomic form factor. The $\vec{q}$ dependence can be determined analytically using equation. 2.2

$$f^0(\vec{q}) = \sum_{i=1}^{4} a_i \exp(-b_i |\vec{q}|^2) + c \tag{2.2}$$

where the coefficients a_i's ,b_i's and c can be found in the International Tables for Crystallography Volume C[36].

At energies much greater than the binding energies of the electrons in the atoms, the electrons may be considered as free particles and equation. 2.1 is valid. In the limit where $\vec{q}$ goes to 0, f^0 goes to Z, the atomic number of the atom.

In reality, the atoms are quantum mechanical particles with the electrons occupying discrete energy levels around the nucleus. Electron transitions may be excited

when the incident x-ray energies are close to the electronic binding energies. When the energy of incident x-rays on a material is just sufficient to excite electrons between energy levels in the atom the energy is said to be at the absorption edge. In the vicinity of the absorption edge, there is a rapid variation in the absorption and scattering behavior and hence, a rapid variation of the atomic scattering factor. This is referred to as anomalous dispersion. Corrections have to be applied to the atomic form factor to take into consideration the response of the electrons close to their resonant energies. These corrections may be understood by considering the system to be a damped harmonic oscillator with associated resonant frequency ω_s and damping constant Γ driven by the x-ray electric field with equation of motion:

$$\ddot{x} + \Gamma\dot{x} + \omega_s^2 = \frac{eE_o}{m}e^{i\omega t} \tag{2.3}$$

The dispersion corrections has a real part f' and an imaginary, phased shifted part f'' given by:

$$f' = \frac{\omega_s^2(\omega^2 - \omega_s^2)}{(\omega^2 - \omega_s^2) + \omega_s\Gamma)^2} \tag{2.4}$$

$$f'' = \frac{\omega_s^2(\omega\Gamma)}{(\omega^2 - \omega_s^2) + (\omega\Gamma)^2} \tag{2.5}$$

Due to the electronic response close to the the resonant edge, the atomic form factor would have a reduction in its real part given by f' and an additional phase-lagged dissipation term, f''. These terms go to zero when the x-ray energy is far from the absorption edge.

The modified atomic form factor including the dispersion correction terms is given by:

$$f(\vec{q}, \lambda) = f^0(\vec{q}) + f'(\lambda) + f''(\lambda) \tag{2.6}$$

where λ is the wavelength of the incident x-rays.

The anomalous response is element specific, thus, it is possible to tune the response of different elements in a system by changing the x-ray wavelength. For example, the real part and imaginary parts of the scattering factors for Ga and As as a function of x-ray energy are shown in Fig. 2.1. The Ga K-edge occurs at 10.367 keV and the As K-edge is at 11.867 keV.

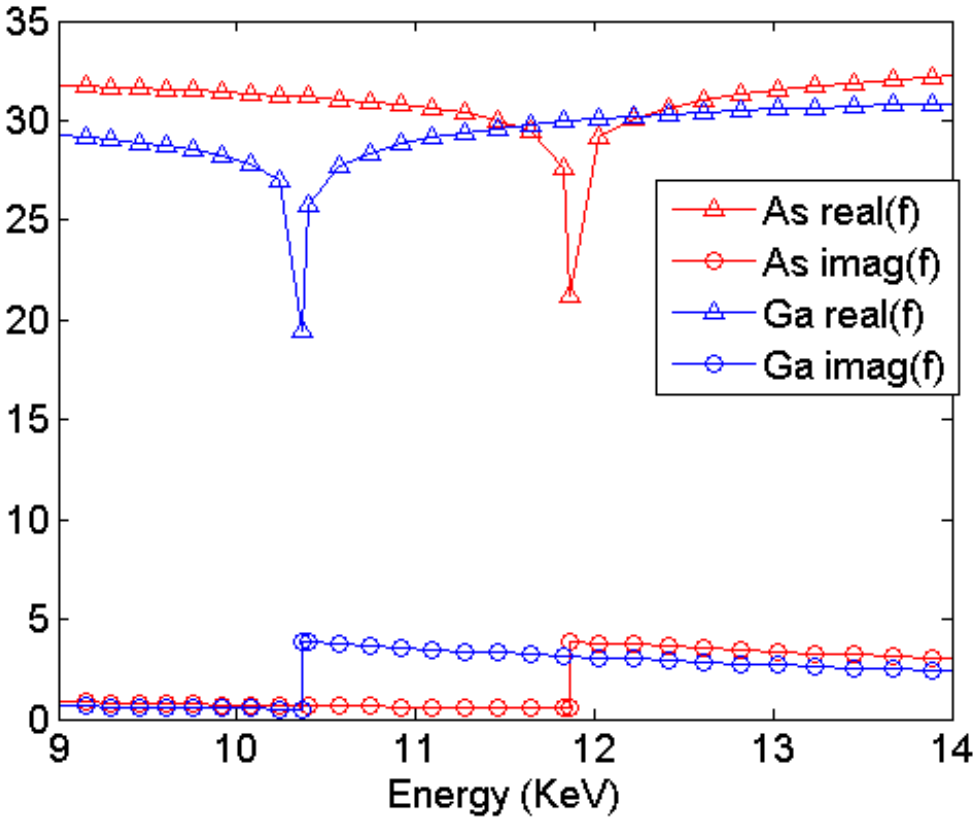

Figure 2.1: Variation of the real and imaginary parts of the atomic form factors for Ga and As. The Ga K-edge occurs at 10.367 keV and the As K-edge occurs at 11.867 keV

Scattering from a unit cell

The scattering factor, $F^{uc}(\vec{q})$, of a unit cell is given by the sum of the form factors of all the atoms in the unit cell multiplied by their corresponding phase terms and

an additional exponential term referred to as the Debye-Waller factor, is included to account for thermal vibrations of the atom.

$$F^{uc}(\vec{q}) = \Sigma_j f_j(q,\vec{\lambda}) e^{i\vec{q}\cdot\vec{r_j}} e^{M_j} \tag{2.7}$$

where r_j is the position of the j'th atom, M_j is the Debye-Waller factor of the j'th atom.

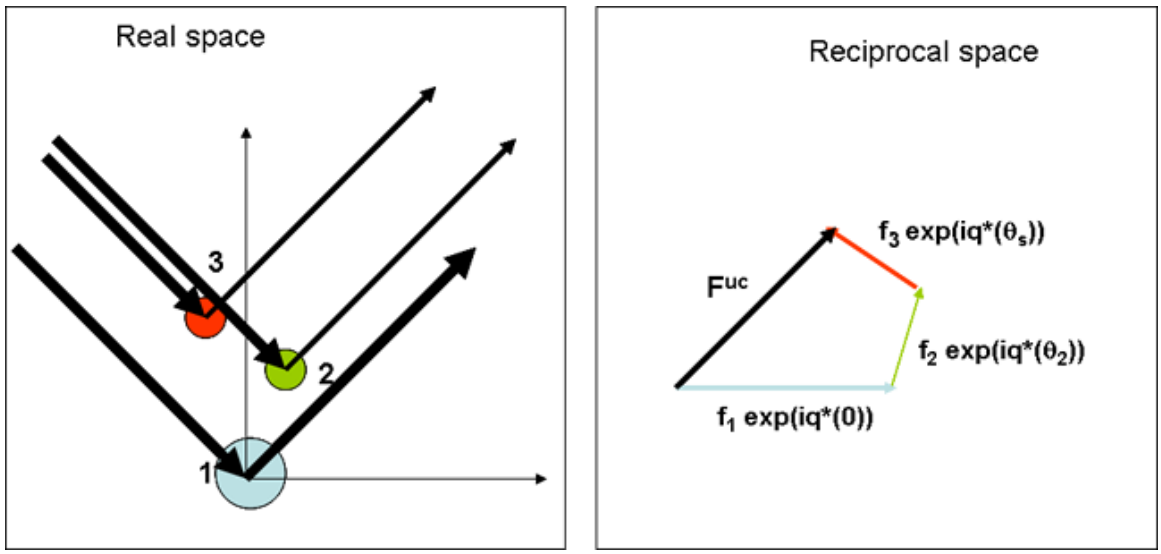

Figure 2.2: Illustration of unit cell structure factor for a unit cell containing 3 atoms. The structure factor in reciprocal space is a vector sum in a complex plane of the contributions of the 3 atoms. The magnitude of each vector corresponds to the amplitude of the atomic form factor, f_j, of the corresponding atom. The direction of each vector is given by the phase, θ_j, which is equal to the dot product of the momentum transfer vector $\vec{q}$ and the position of the atom relative to the origin of the unit cell.

Scattering from a crystal

Crystalline materials can be described in terms of a pattern which repeats itself in one, two or three dimensions. The basic structure which repeats is the unit cell. The n-dimensional grid which defines this pattern is referred to as the crystal lattice. The lattice points are defined by a periodic lattice vector $\vec{R_n}$.

The scattering factor of the entire crystal may be considered as a vector sum of the structure factors over all the N unit cells with each unit cell containing N_{uc}

atoms.

$$F_{cryst}(\vec{q}) = \Sigma_n^N \Sigma_i^{N_{uc}} f_i(\vec{q}) exp(-2\pi i \vec{q} \cdot (\vec{r_i} + \vec{R_n})) \tag{2.8}$$

$$= \Sigma_n^N exp(-2\pi i \vec{q} \cdot \vec{R_n}) \Sigma_i^{N_{uc}} f_i(\vec{q}) exp(-2\pi i \vec{q} \cdot \vec{r_i}) \tag{2.9}$$

$$= \vec{F}_{uc}(\vec{q}) \Sigma_n^N exp(-2\pi i \vec{q} \cdot \vec{R_n}) \tag{2.10}$$

$$\vec{F}_{cryst}(\vec{q}) = |\vec{F}_q| exp^{-\phi_q} \tag{2.11}$$

where $|\vec{F}_q|$ and ϕ_q are the amplitudes and phases of the crystal structure factor.

Another way to consider the crystal structure factor is to consider scattering from all the atoms in the system represented by an electron distribution function $\rho_{cryst}(\vec{r})$;

$$F_{cryst}(\vec{q}) = \int \rho(\vec{r}) exp(-2\pi i \vec{q} \cdot \vec{r}) d(\vec{r}) \tag{2.12}$$

It is clear that the crystal structure factors represent the Fourier components of the system's structure expressed as a three-dimensional electron density distribution function $\rho(\vec{r})$. If one could measure the all the $|F_q|$'s and their corresponding ϕ_q's, a direct Fourier transform would yield the electron distribution function and hence, the structure would be uniquely solved.

One does not have to measure every single $\mathbf{F_q}$ to solve a structure. It will be shown in the next section that for specific systems, the intensities are only non-zero along certain directions in reciprocal space and zero elsewhere.

Crystal Truncation Rods

If the crystal is periodic and infinite in all three dimensions, the equation above is reduced to δ-function like peaks at integer values of h,k and l with no scattering between the peaks. When the system is confined in one direction, the sum in that direction is no longer infinite resulting in diffuse scattering in the confined direction. This is the situation for thin films and surfaces where the size in the vertical direction

is on the order of tens of unit cells compared while the in-plane dimensions are on the order of 10^6 unit cells. Bragg rods arise as a result of the superposition of diffuse scattering from the quasi-2D film and the strongly peaked Bragg diffraction from the 3D substrate. All the information about the film is contained in the diffuse scattering between the substrate Bragg Peaks.

2.2 The Phase Problem and Structural Determination

X-ray detectors are photon counters i.e. they measure intensities by counting by counting the number of incident photons on an active region(sometimes referred to as a 'pixel') of the detector. The measured intensities I_{hkl} correspond to the modulus square of the complex structure factors and thereby all the phase information is lost.

$$I_{hkl} = |\vec{F}_q| exp^{-\phi_q} |\vec{F}_q| exp^{\phi_q} = |\vec{F}_q|^2 \tag{2.13}$$

The ability to retrieve lost phase information during x-ray diffraction measurements is essential in structure determination and is the main challenge in x-ray crystallography. Structures are determined from measurements of large sets of intensities by attempting to reconstruct the lost phase information. In principle, there are an infinite number combinations of phases and amplitudes which would reproduce a given set of intensities. However, by imposing constraints on the phases, a unique physical solution can be achieved.

Structural Refinement

Structural refinement methods are routinely used to determine the lost phases. An initial model of the system is guessed using all the information known about the system. The diffraction intensities of this model are calculated and compared with experimental data. If the fit to the data is not good, the reference structure is

modified iteratively until a structure is obtained whose calculated diffraction intensities fit the experimental data. This approach usually involves modifying numerous free parameters depending on the complexity of the system whose structure is being determined. Fitting using least square fitting grid search algorithms in real space is also usually computationally intensive and may give a false structural solutions which lie in local minimal. Convergence on the correct solution is thus, strongly dependent on the quality of the initial model.

In general, fitting and refinement methods alone are inadequate for solving complex epitaxial structures because there are just too many variables in the problem to find a reliable, unique solution.

Direct Methods

Direct methods make use of the measured intensities in retrieving the lost phases by assuming statistical relationships between the measured intensities. The assumption is that for a given set of measured diffraction intensities, there is a *unique* set of phases which can be combined the measured amplitudes to give a physically sound structure with a real and positive electron density confined to a fixed volume in space. By iteratively imposing constraints in both real and reciprocal spaces, it is possible to converge on the correct physical solution from the myriad of possible solutions. The reciprocal space constraint is that the calculated diffraction intensity of the system matches the experimentally recorded intensities. The use of direct methods avoids the critical dependence of the starting model converging on the correct solution. A number of direct phase retrieval methods have been developed including the recently developed Coherent Bragg Rod Analysis (COBRA) procedure[29, 31], the Phase and Amplitude Recovery and Diffraction Image Generation Method (PARADIGM) [37]

and the Multiple-wavelength Anomalous Diffraction method (MAD)[35].

2.3 Coherent Bragg Rod Analysis

The Coherent Bragg Rod Analysis(COBRA) is a powerful direct method applicable to solving the structure of epitaxial and semi-epitaxial thin film systems. COBRA assumes the measured total scattering factor $\vec{T}$ to be a coherent sum of scattering from a known reference electron density $\vec{S}$ and an unknown electron density $\vec{U}$. The reference may be the known substrate and a simple model for the film. The unknown electron density may be viewed as a perturbation to the reference which would yield the correct structure. The method is based on the approximation that along substrate-defined Bragg rods, the contribution of scattering from the unknown electron density intensity is continuous and slowly varying.

This condition is reasonable in view of the fact that the 'unknown' CSF is normally localized to a narrow region in real space (the thin film and its interface with the substrate) and therefore should be broad in reciprocal space; however, this condition is only an approximation and one has to iterate to solve the structure. Each successive iteration produces a more refined reference which is then used as a starting point for the next iteration. Once the correct structure is obtained, additional iterations do not modify the structure further.

At two adjacent points along a Bragg rod differing by $\Delta\vec{q}$.

$$\vec{S}(\vec{q}-\frac{\Delta\vec{q}}{2})+\vec{U}(\vec{q}-\frac{\Delta\vec{q}}{2})=\vec{T}(\vec{q}-\frac{\Delta\vec{q}}{2}) \tag{2.14}$$

$$\vec{S}(\vec{q}+\frac{\Delta\vec{q}}{2})+\vec{U}(\vec{q}+\frac{\Delta\vec{q}}{2})=\vec{T}(\vec{q}+\frac{\Delta\vec{q}}{2}) \tag{2.15}$$

Since the film is confined in the one direction, it can be assumed that the CSF varies continuously along the Bragg rod if $\vec{U}$ varies slowly relative to $\vec{S}$. Thus one

has the approximation:

$$\vec{U}(\vec{q}-\frac{\Delta\vec{q}}{2})=\vec{U}(\vec{q}+\frac{\Delta\vec{q}}{2})\approx\vec{U}(\vec{q})_a \tag{2.16}$$

and

$$|\vec{S}(\vec{q}+\frac{\Delta\vec{q}}{2})+\vec{U}(\vec{q})_a|=|\vec{T}(\vec{q}+\frac{\Delta\vec{q}}{2})| \tag{2.17}$$

$$|\vec{S}(\vec{q}-\frac{\Delta\vec{q}}{2})+\vec{U}(\vec{q})_a|=|\vec{T}(\vec{q}-\frac{\Delta\vec{q}}{2})| \tag{2.18}$$

The above assumption can be made if the reference system is chosen such that the scattering factors are of the same order of magnitude as the measured intensities and if the origin of the real space coordinate system is close to to the part of the unknown electron density and far from the part with the known electron density. The solution to equations 2.17 and 2.18 which gives the minimum change in $\vec{U}$ for two adjacent points in reciprocal space gives the correct unknown complex scattering factor since U is assumed to vary slowly along the Bragg rods. The total scattering factor is then recalculated using 2.14 and 2.15 and Fourier transformed to obtain the three dimensional electron density in real space.

By using the substrate as a reference, Bragg rod measurements and COBRA can be used to determine the unknown electron density distributions for epitaxial and semi-epitaxial thin films. The films are assumed to have two-dimensional periodicity within the plane of the film and aperiodicity in the perpendicular direction. Since the films studied in COBRA are epitaxial, the assumption can also be made that the first few monolayers of the film have 2D periodicity coherent with that of the underlying substrate. However, in the case where the film has a multiple period commensurate with the substrate, the film can be assumed to be folded in plane by moving all atoms into one 2D substrate defined unit cell using using unit cell vectors [30, 29].

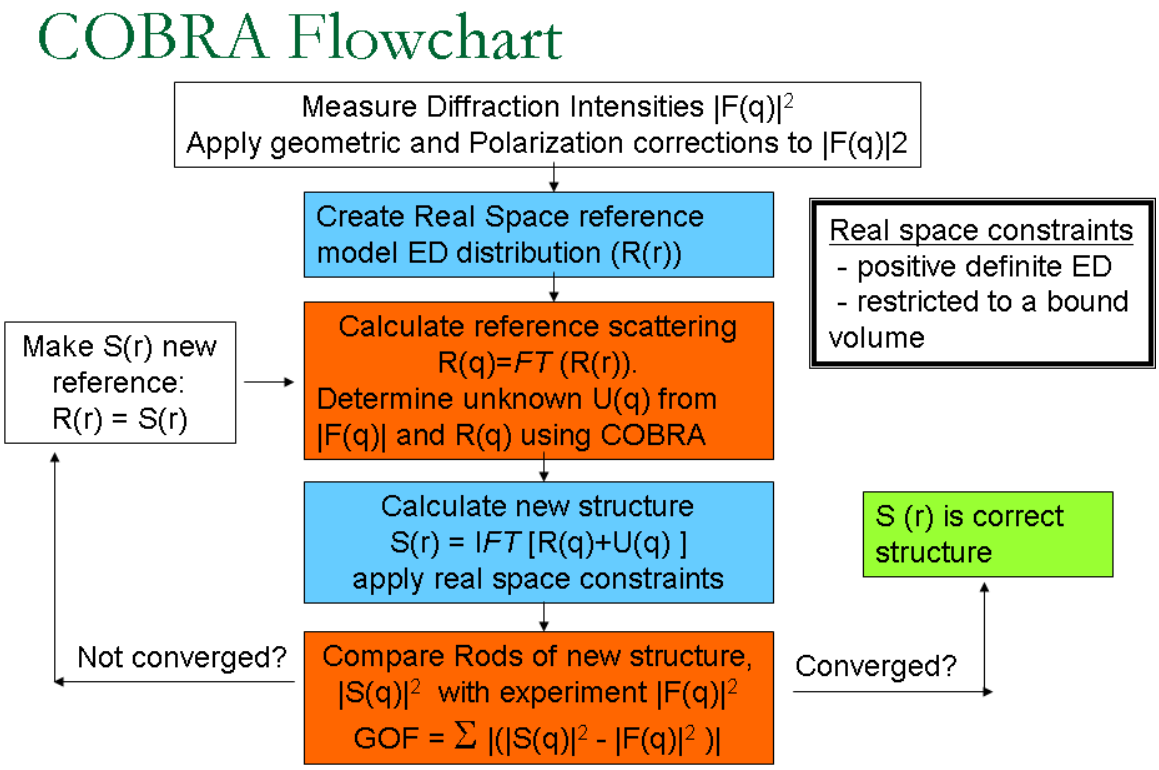

Figure 2.3: Structure determination using COBRA.

Figure 2.3 provides an outline of the COBRA method.

Phase Calculation in COBRA

The phase calculation in COBRA involves four steps:

1. The replacement of the 'lost' data with data from the refined reference to ensure continuity of the rod.

2. The calculation of the unknown scattering factor, $\vec{U}$. using the amplitude of the 'filled' measured data ($i.e.|T_{hkl}|$) and the amplitude, $|R_{hkl}|$, and phase, ϕ_R, of the reference

3. The application of a Hanan filter to filter high-frequency noise from the calculated $\vec{U}$

4. A smooth interpolation of the points with large uncertainties around the Bragg peak for $\vec{U}$.

After the interpolation and filtering steps, the phase and amplitude of the unknown $\vec{U}$ have to be adjusted so that $|\vec{U} + \vec{R}| = |\vec{T}|$. This is achieved using the equation below and is illustrated in Fig. 2.4 where $\vec{U}'$ is the renormalized unknown scattering.

$$\vec{U}'_{hkl} = (\vec{U}_{hkl} + \vec{R}_{hkl}) \cdot \frac{|\vec{T}_{hkl}|}{|\vec{U}_{hkl} + \vec{R}_{hkl}|} - \vec{R}_{hkl} \tag{2.19}$$

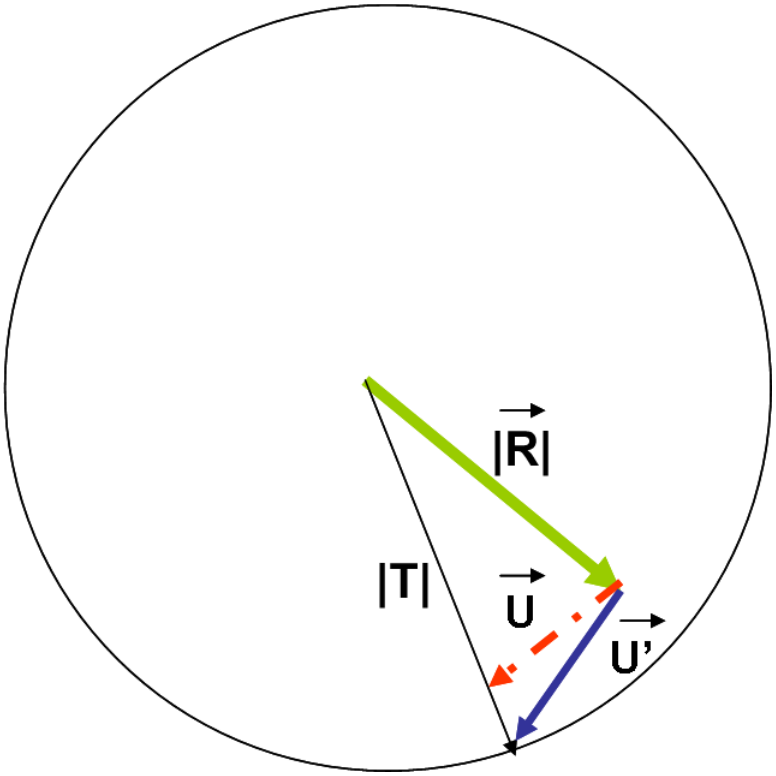

Figure 2.4: Recalculating the unknown contribution to the total CSF after filtration and interpolation

This correction is minimal and is refined in subsequent phasing iterations.

2.3.1 Optimizing the real-space origin

As stated earlier, the COBRA ansatz is valid if the real space origin is close to the unknown region i.e., the region which deviates the most from the chosen reference. This optimum origin results in an unknown ED whose corresponding CSFs are slowly varying.

The structure factor for a given *hkl* in reciprocal space is given by

$$F_{hkl} = \sum f_i exp^{2\pi i \tilde{r}\cdot\tilde{q}} \tag{2.20}$$

A shift in real space by $\vec{s}$ is given by

$$F_{hkl}^{shift} = \sum f_i exp^{-2\pi i(\tilde{s}+\tilde{r})\cdot\tilde{q}} \tag{2.21}$$

$$F_{hkl}^{shift} = exp^{-2\pi i\vec{s}\cdot\vec{q}} F_{hkl} \tag{2.22}$$

Since the shift is only in the z direction *i.e*,, $\vec{s} = s\vec{z}$ and $\vec{r}\cdot\vec{q} = s\cdot l$, thus, the expression simplifies to

$$F_{hkl}^{shift} = exp^{-2\pi\cdot i\cdot s\cdot l} F_{hkl} \tag{2.23}$$

The amplitude of the shifted structure factor for a given *hkl* is

$$|F_{hkl}^{shift}| = |exp^{-2\cdot\pi\cdot i\cdot s\cdot l} F_{hkl}| = |F_{hkl}| \tag{2.24}$$

Thus, shifting the origin in real space shifts the phase for each F_{hkl} but keeps the amplitude unchanged.

During the COBRA analysis, a parameter (n_shift) to vary the number of layers to shift the origin in a direction normal to the sample surface is optimized after the initial reference has been obtained.The phase error, Φ_{err}, corresponding to a given n_shift is given by the equation

$$\Phi_{err} = \frac{1}{Nrods\cdot N_q} \sum_{i=}^{Nrods} \sum_{i=1}^{N_q} |\vec{U}_{hk}(l_i) - \vec{U}_{hk}(l_{i-1}))| \tag{2.25}$$

where N_q is the number of data measured points.The value of n_shift which gives the minimum error is chosen and fixed for the rest of the analysis (In theory, this can be optimized for each phasing iteration).

2.4 Convergence

The correct structure should reproduce the experimental data as best as possible within the experimental errors. Experimental constraints and systematic errors may affect the quality of the measured data and hence, the 'confidence' level of the final structure.

The high intensity data points close to and at the Bragg peaks are considered to be unreliable because errors in filter calibration are amplified and the detector response may also be non-linear in this high flux regime. Also, only a limited volume of reciprocal space can be sampled due to experimental constraints. The resolution in real space in the vertical direction is given by $\frac{a}{2q_z^{max}}$. For a system with a GaAs substrate with $a = 5.65045$ and $q_z^{max} = 4.5$, the resolution is 0.6282 Å. By zero-padding the measured data, the density of points is increased, however, this does not increase the resolution.

The COBRA approximation relies on the condition that the structure factor is continuous, thus these gaps have to be filled either by interpolating the data or by iteratively filling those points with information from the reference structure.

Convergence is assessed based on the following conditions:

1. The electron density should be confined and real and positive definite with little or no negative parts.
2. The sum of square of intensities given by $\frac{\Sigma(|F_{hkl}^{calc}|^2-|F_{hkl}^{meas}|^2)^2}{\Sigma|F_{hkl}^{meas}|^2}$ should converge
3. The sum of squares of amplitudes, $\frac{\Sigma(|F_{hkl}^{calc}|-|F_{hkl}^{meas}|)^2}{\Sigma|F_{hkl}^{meas}|}$ should converge

2.5 Refining with the Iterative Projection Difference Map Algorithm (IPDM)

It should be noted that although direct methods converge on the correct solution, this solution is only approximate to the true structure of the system and further refinement can be done to to obtain more numerically precise parameters of the system.

In most of the systems studied using COBRA alone, the atomic positions have been resolved to less than 0.1 Å.The error in determining composition is usually on the order of 5-10% and sufficient to differentiate between atoms in the system if they have a large variation in Z. When more accurate results are required, the approximate results from COBRA may be used as a starting point for structural refinement programs like FIT [38, 39] or the iterative projection difference map algorithm[40].

The iterative projection difference map (IPDM) method proposed by Elser[40] was used to refine the structure of the QD systems in this study after COBRA was applied.

The IPDM method starts off with an electron density ρ_0 , which could be arbitrary in the absence of any better information about the structure. In this case, the COBRA-derived electron density was used as the starting point.

Two operations (or projections) are performed in each IPDM iteration:

1. Projection 1, $\prod^{real}$, involves constraining the electron density in real space. The real space support constraints include zeroing out negative ED and confining the ED to a bounded region in space. This constrained ED would be defined as ρ^{p1}.

2. A second projection, $\prod^{recip}$, involves constraining the structure factors of a given

ED to have amplitudes equal to the amplitudes of the measured data, i.e.,

$$\prod^{recip}(\rho) = FT^{-1}(\frac{|T|}{|FT(\rho)|}FT(\rho)) \tag{2.26}$$

Let the ED resulting from taking the inverse Fourier transform of the second projection be ρ^{p2}. An electron density ρ_{sol} is said to be converged when

$$\rho_{sol}^{p1} = \rho_{sol}^{p2} = \rho_{sol} \tag{2.27}$$

To achieve this convergence from an initial ED, an iterative set of projections are carried out until a difference map is minimized. The difference map for each iteration is calculated from

$$\rho_n^{diff} = (\gamma - 1)[\prod^{real}\prod^{recip}\rho_n)] + (\gamma + 1)[\prod^{recip}\prod^{real}\rho_{n+1})] - \gamma(\prod^{recip}(\rho_n) + \prod^{real}(\rho_{n+1})) \tag{2.28}$$

where ρ_n is the starting ED for iteration n and $\rho_{n+1} = \rho_n + \rho_n^{diff}$ for the $(n+1)^{th}$ iteration. The parameter γ is optimized to give the least solution time, however, there is currently no theoretical way of determining its value. We use $\gamma = \frac{1}{0.7}$ which was found by Elser *et al.* [40] to be the optimum.

Convergence is assessed by the norm of the difference map:

$$\epsilon_n = \|\rho_n^{diff}\| \tag{2.29}$$

After the COBRA analysis converged, the final ED output, ρ^{COBRA}, was used as the initial input for the IPDM method which was run without the atomicity constraint. This resulted in a final ED which gives significantly better agreement with the measured data than when COBRA is used alone. Using ρ^{COBRA} as the DMA input, results in a fast convergence after less than 30 iterations (about 10 iterations in some cases). For some of the tests carried out, convergence occurred in less than 10 IPDM iterations with results which were almost indistinguishable from

the measured data. This is in contrast to published results which required > 1000 iterations to obtain a solution when a random ED is chosen as the starting point[40].

2.6 Anomalous scattering and COBRA

For element specificity, the anomalous response of the CSF to the incident x-ray wavelength can be used together with COBRA in situations where the multiple atomic species may occupy the same lattice site as in the case of alloys. The exact relative amounts of these elements at each lattice site can be determined from the difference between COBRA derived ED maps taken at multiple wavelengths where the energies are selected to be close to the absorption edges of the constituent elements. Fig. 2.5 compares rods simulated for a system comprising of 2 ML GaAs on an $In_{0.53}Ga_{0.47}As$ substrate to illustrate the differences in the measured intensities when the x-ray wavelength is selected to be 10.362 keV (5 eV below the Ga K-edge) and 11.862 keV (5 eV below the As K-edge).

The integration of the ED 3D Gaussian peaks gives a quantity proportional to the effective number of electrons at that site. This effective volume, V, at that x-ray wavelength, λ, is determined by the the relative fractions of the probable elements which would occupy that site. The value of V at a given lattice site can be expressed as:

$$V(\lambda) = \Sigma_{i=1}^{N} x^i Z_{eff}^i(\lambda) \tag{2.30}$$

$$x^i = c^i \theta_n \tag{2.31}$$

where

$N = \#$ of atom types at lattice site

$Z_{eff}^i =$ effective number of electrons of i'th atom

$x^i =$ fractional occupation of the i'th atom

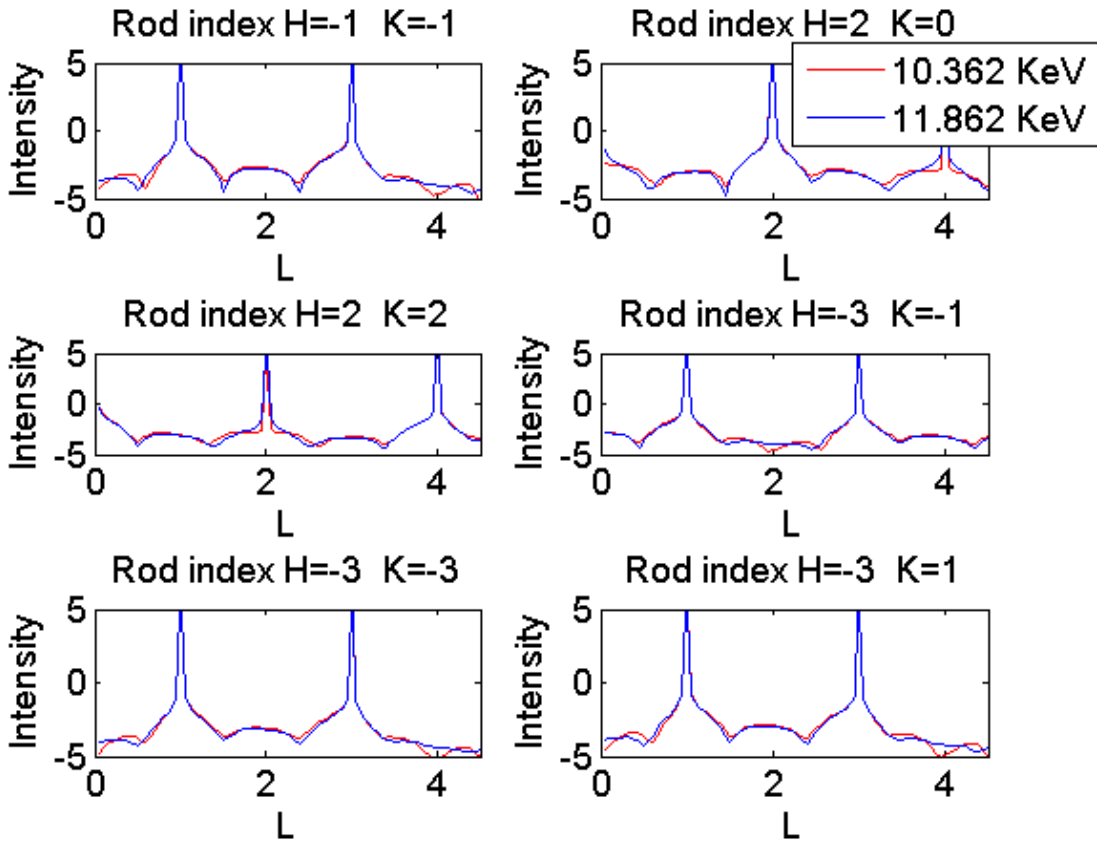

Figure 2.5: Comparison of simulated Bragg rods for 2 ML GaAs on an $In_{0.53}Ga_{0.47}As$. The intensity is plotted on a logarithmic scale.

θ_n = coverage of the n'th layer

c^i = concentration of i'th atom

The number of unknowns can be reduced by measuring close to the resonant edges of the elements which may occupy a single lattice site. The minimum number of energies required to deconvolute the composition of a given system is equal to the number of elements in the system which could occupy a given lattice site.

For example, in the case of InGaAs, in the absence of anti-site defects, alloying would be expected only at the group III(G-III) sites. To determine the fractions of In and Ga in each layer it is only necessary to measure at and well away (at least 10

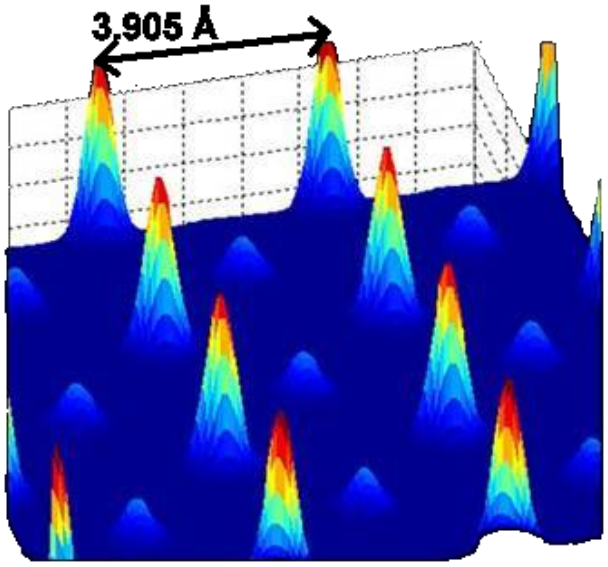

Figure 2.6: Two dimensional slice through electron density. The peaks in the figure represent atoms. The intensities of the peaks are a function of the chemical composition.

eV) from the Ga edge.

The integrated volume at a given G-III site for an ED map obtained at at the Ga edge (λ_A) for N=2 is

$$V(\lambda_A) = x^{In} Z^{In}_{eff}(\lambda_A) + x^{Ga} Z^{Ga}_{eff}(\lambda_A) \tag{2.32}$$

and away from the Ga edge(λ_B) is

$$V(\lambda_B) = x^{In} Z^{In}_{eff}(\lambda_B) + x^{Ga} Z^{Ga}_{eff}(\lambda_B) \tag{2.33}$$

The Z_{eff}'s correspond to the real part of the atomic form factor for $\vec{q} = 0$. This value may be obtained directly from literature since the x-ray wavelengths are well defined. Alternatively, they may be measured more precisely during the data acquisition by scanning through the K-edge and analyzing the resulting x-ray fluorescence spectrum. Either way, they are well defined values and one is left with two equations which may be directly solved for the 2 unknowns: x^{In} and x^{Ga}. The

coverage of that layer can be determined by $\theta = x^{In} + x^{Ga}$

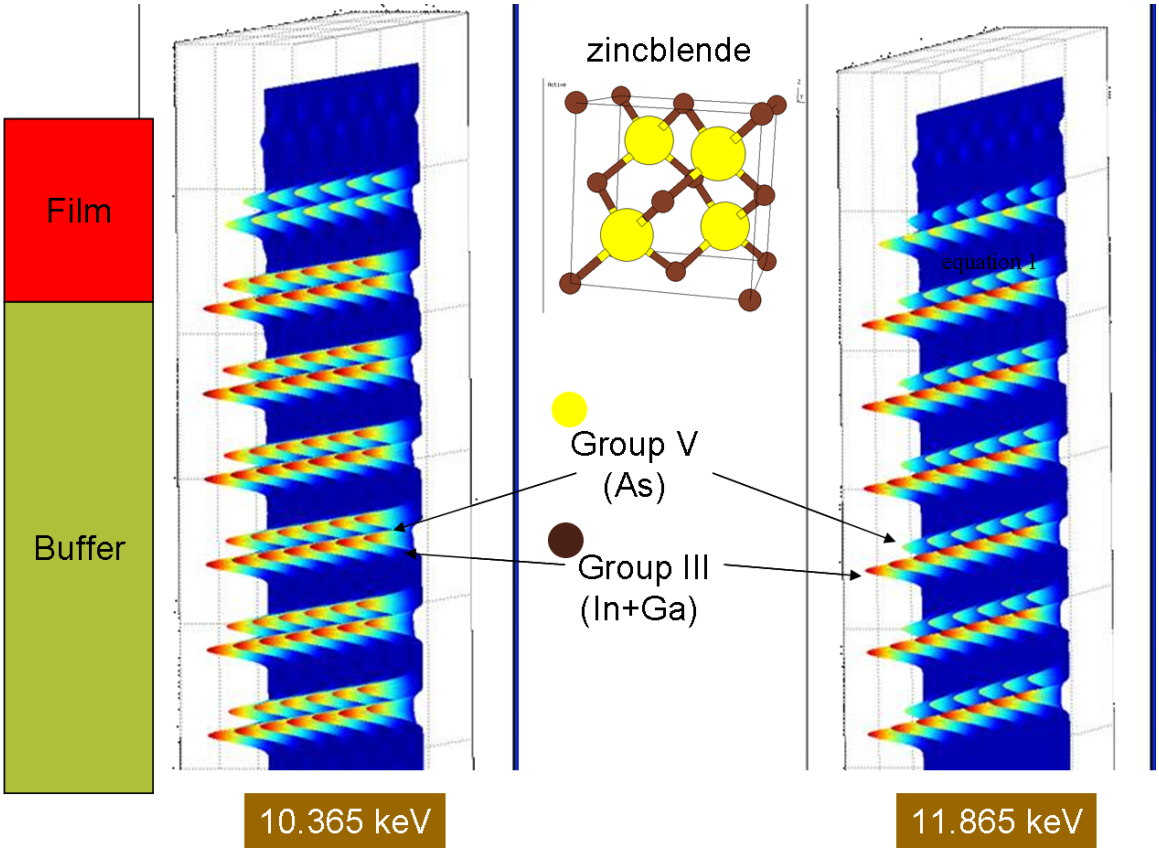

Figure 2.7: Comparison of 110 slices through ED maps determined from Bragg rods measured at (a)10.365 keV (b)11.865 keV for GaAs deposition temperature of 480^oC The difference in the peak heights at the 2 energies is due to the anomalous wavelength dependence of the atomic scattering factors of As and Ga.

By choosing λ_B to be close to the As edge, self-consistent checks may be made in the results, especially in rough samples where the layer coverages would be less than unity.

First, since the same sample is measured under the same conditions at the two wavelengths, the fractional occupancies for As calculated at the Ga(λ_A) and As(λ_B) edges should be equal assuming no G-III, G-V intermixing, i.e.,

$$x^{As}(\lambda_A) = x^{As}(\lambda_B) \tag{2.34}$$

Once this is verified, bilayer growth (i.e. each G-III layer has a corresponding adjacent G-V layer of equal coverage) would be confirmed if the following condition is true for the previously calculated fractional occupancies for each atomic species in each layer: $x^{As} = x^{Ga} + x^{In}$.

The determination of the fractional occupations requires an accurate integration of the ED peak volume with errors within a few percent. Layers with less than 50% coverage are more sensitive to errors in the integrated ED's and care must be taken to reduce the inclusion of noise in the peak integral.

2.6.1 Determining the Integrated Electron Density

In this work, two methods were tested for obtaining the peak integral: Fitting the peaks as 3D Gaussian and integrating the fits and summing up the intensities in the pixels around the peak.

The first method assumes that the peaks are Gaussian-like and the volume is found from a 1D out-of-plane Gaussian fit and a 2D Gaussian in-plane fit. The peak volume is:

$$V = A \cdot H \cdot \sigma_x \cdot \sigma_y \cdot \sigma_z \tag{2.35}$$

where H, σ_x, σ_y and σ_z are the fitted peak height, x width, y width and z width respectively and A is a normalization constant obtained by normalizing to a peak deep inside the substrate where no deviations from the nominal composition are expected.

The advantage of this method is that, assuming the peaks are Gaussian, performing a fit effectively increases the resolution in the vicinity of the fitted peak. Thus, parameters like the peak widths, which are related to the DW factor and disorder, and the peak centers, which determine the lattice positions, can be determined to

about 0.02 Å.

The second method involves summing up all the pixels in a defined 3D box around the centered on each peak maxima. The disadvantage of this approach is that noise, which would otherwise be discarded when the peaks are fit with a Gaussian, are now included in the summation.

The results presented in this thesis were obtained using the fitting approach to determine the integrated electron densities.

2.7 Self Assembled Quantum Dots

Self assembled quantum dots, (SAQD) can be grown effectively by Molecular Beam Epitaxy (MBE) by the Stranski-Krastanow growth mode. SAQDs spontaneously form when epitaxial thin films are deposited on substrates with a large lattice mis-match [41, 42, 43, 44]. An example is the case of InAs on GaAs substrates where there is a 7% lattice mismatch between the film and the substrate. The islands spontaneously form to relieve mismatch strain when the thickness of the film becomes greater than a critical thickness which is dependent on a number of factors including the shape and elastic modulus of the quantum dot, and the growth conditions. This results in the transition of the 2D film to an array of quantum dots. For example, in the case of InAs on GaAs, the critical thickness for QD formation can be as low as 1.7 monolayers(ML) [45, 46].

Relaxation in thin films may be plastic or elastic depending on the growth conditions. Plastic relaxation results in defects such as stacking faults and threading dislocations. The mechanism leading to the creation of coherent (i.e., in epitaxial registry with the substrate) SAQD's arises from the elastic relaxation of stress without the formation of misfit dislocations[42]. These stress relieving islands were in

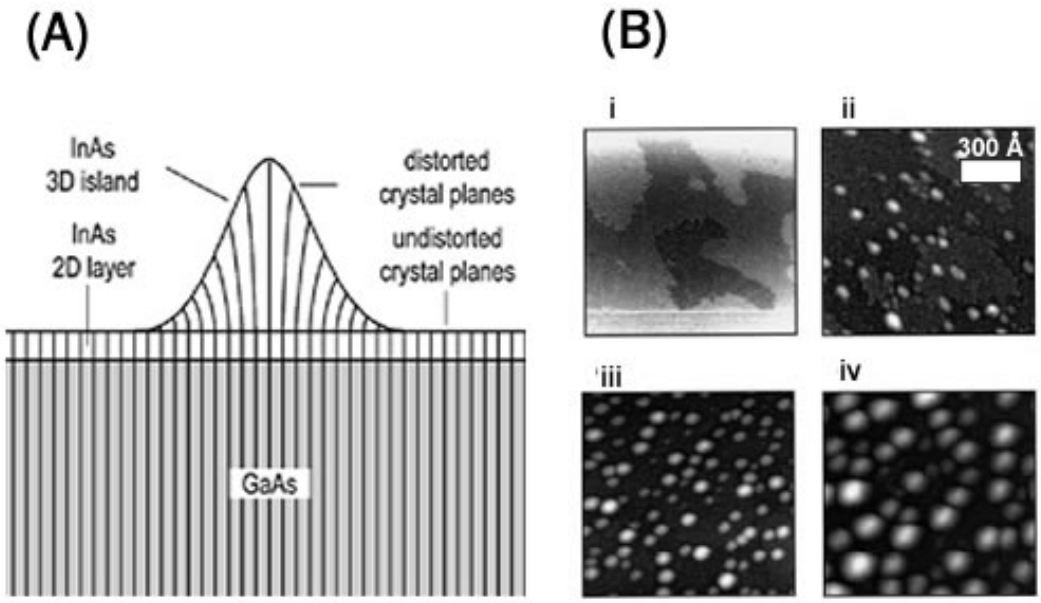

Figure 2.8: (A) shows a schematic of the lattice distortion in a 3D InAs island. (B) shows STM (1000 x 1000 Å) images corresponding to a range of InAs depositions at 450^o C for i)1.4 ML ii)1.7 ML iii)2.0 ML and iv)2.7 ML clearly showing the 2D to 3D transition after 1.4 ML.[16]

the past considered a nuisance because they led to roughening of epitaxial films. In contrast to fully strained epitaxial thin films, the in-plane lattice parameter within the dots may relax continuously along the growth direction allowing for relaxation at the free surfaces.

To attain the theoretically determined superior characteristics of QD structures, stringent control of the strain, size, shape, composition and crytallinity of the dot-matrix environment is required. Ideally, the dots would have a narrow distribution in the composition, shape and sizes with no plastic relaxation in the case of strained dots. The emission properties of the dots are strongly determined by these factors which affect the dot-substrate potential barriers and impurity levels and consequently, the confinement of charges within the dots. The growth parameters strongly influence these properties and many studies have been devoted to studying the ef-

fect of growth conditions for QDs grown using two main growth methods - Stranski Krastanow and Droplet Heteroepitaxy.

Although total control of the growth of SAQD's has not yet been achieved, it is possible to obtain correlated dots with less than 10% dispersion in their size, shape and composition[47, 48]. Tersoff *et al.* have demonstrated experimentally and theoretically that when successive layers of dots are grown, the island size and spacing become more uniform evolving into a more regular three-dimensional arrangement[49].

2.7.1 Composition and Strain in Stranski-Krastanow In(Ga)As/GaAs Quantum Dots

In addition to the morphological change to partially relieve strain, stress induced segregation[50] occurs in the formation of quantum dots from strained 2D films resulting in a composition of the islands very different from the nominally deposited material.

In Tersoff's theoretical model for the nucleation of dislocation-free islands[50] from an alloy film such as $In_xGa_{1-x}As$, segregation of the larger misfit component (in this case, InAs) at the initial stages of nucleation leads to an In rich core. This strain driven segregation occurs to minimize the free energy of the system. If the incident flux is turned off after nucleation, the islands continue to grow at the expense of the depleted film resulting in the dots having an enriched core with less In in the outer layers of the dot. This leads to what is described as an effective 'self-capping' of the dots.

Galluppi *et al.*[51] also suggest that in InAs/GaAs quantum dot systems, In and Ga interdiffusion as well as In segregation occur as mechanisms to relieve mismatch strain. For example, in the growth of InAs on GaAs, Ga atoms diffuse into the InAs islands with Ga concentration varying continuously from 100% at the dot-substrate

interface to 0% at the apex of the dot[17].

To account for the diffusion of Ga into InAs dots, Rosenauer *et al.*[52] propose, based on TEM and photoluminescence measurements, that the segregation of In leads to the generation of vacancies within the metal sublattice. These vacancies are filled by the Ga atoms which diffuse from the GaAs buffer layer.

Lattice spacings and strain profiles have been found to be consistent with compositional variations and have been used indirectly in STM and x-ray measurements to determine concentration profiles within quantum dots. By studying the lattice spacings within nominal $In_{0.5}Ga_{0.5}As/GaAs$ QDs, Liu *et al.* [53] determined using XSTM that the dots possessed In-rich cores with an inverted triangular shape and an In fraction decreasing from center to edge and top to bottom of the dots.

Blokland *et al.*[54] recently used X-STM to infer the compositional profile of nominal InAs/GaAs QDs. By enhancing the topographical contrast of the cleaved sample due to outward relaxation in the strained regions (the higher the In content, the higher the strain) using a high tip voltage of -3.0 V, they determined an vertically and laterally graded composition of In with 100% In at the top of the dots and about 70% at the base of the dots. Based on finite element calculations to simulate their measured relaxation profile, they determined the wetting layer to be as large as 7 ML thick with a composition of $In_{0.225}Ga_{0.775}As$.

Kegel *et al.*[17] have carried out surface x-ray diffraction isostrain mapping studies and reported results on shape, interdiffusion and strain profiles of free standing InAs/GaAs quantum dots with nanometer scale resolution. Their results were averaged over a $1mm^2$ area of free standing dots. They infer the interdiffusion of Ga into the dots from the curvature of isostrain areas. Their conclusion of lateral composition homogeneity within the dots is in contrast with the "inverted-cone In-profile"

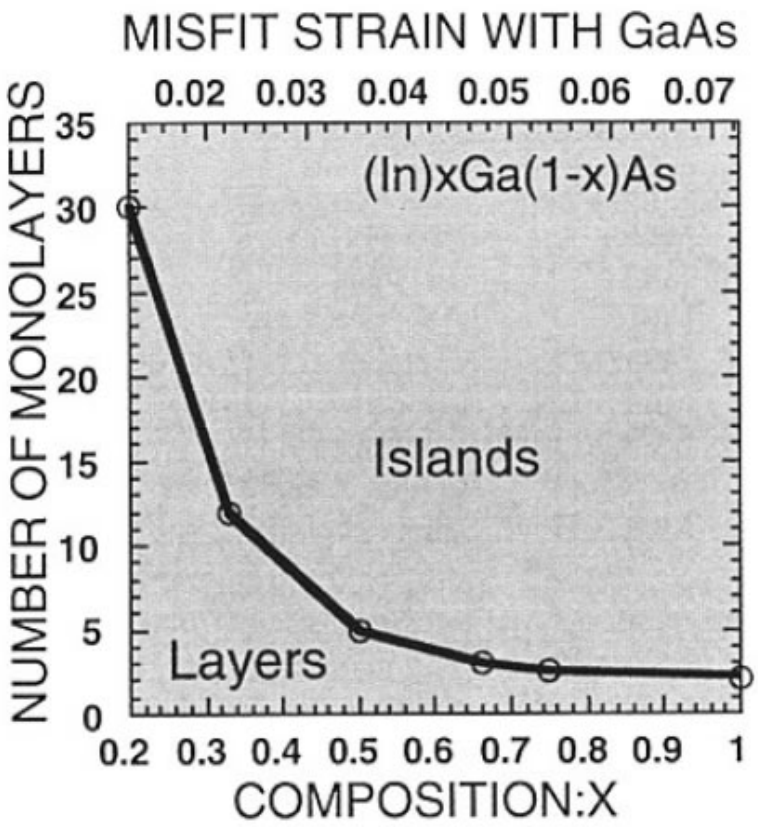

Figure 2.9: Plot showing the number of $In_xGa_{1-x}As$ monolayers required for the transition from 2D to 3D growth as a function of composition for MBE deposited structures [46]

presented by Liu *et al.*[53].

AFM and STM can be used to determine the shape and sizes of uncapped islands. Kolosov *et al.* [55] have developed a modification of AFM called Ultrasonic Force Microscopy which makes the method also sensitive to strain and composition with 5 nm spatial resolution. The tunnel current in STM is sensitive to material composition and strain; however, only conductive samples can be imaged. High resolution Cross Sectional STM (XSTM) of cleaved samples can be used to imaged buried structures with resolutions on the atomic scale. Lita *et al.* [43] report significant In-Ga intermixing within InAs dots due to In surface segregation.

TEM is also used to image planar sections of buried heterostructures. The main

limitations here again are that the island sizes measured may be inaccurate due to interaction of diffracted electrons with strain fields. The preparation of the sample for TEM is destructive and can disturb the structure and strain fields one is trying to measure. It is also not sensitive to chemical composition, unless some kind of analysis technique is used in conjunction with the TEM imaging (e.g. x-ray fluorescence or electron energy loss spectroscopy (EELS). These spectroscopic techniques are becoming common at high resolution, although not yet at the Ångstrom level. Also, cross sectional STM and AFM require cleavage of the sample. Thus only certain planes where cleavage occurs are accessible to XSTM and AFM. Additional outward strain relaxation of the islands does occur due to material removal and thus, the interpretation of results has to be performed with care[48].

Given that segregation and interdiffusion are strongly dependent on the growth conditions, the differences might be accounted for, however; a more direct method for obtaining composition and strain information would lead to a better understanding of the compositions of these structures.

A number of x-ray techniques have been used to study buried nanostructures including grazing incidence small angle x-ray scattering, x-ray reflectivity, grazing-incidence x-ray diffraction and anomalous x-ray scattering. X-rays, as a result of their relatively large penetration power, permit the non-destructive study of buried structures; however, most x-ray techniques suffer from the limitation that since measurements are made in reciprocal space, model fitting, usually with numerous free parameters, [17, 56] is required to reconstruct the real space structures due to the challenges associated with extracting phase information. Robinson *et al.* have successfully used phase reconstruction techniques to determine the shape and sizes of Au nanoparticles by oversampling the reciprocal space diffraction data with coherent

Material	Band Gap (eV)	Lattice constant (A)	Density(g cm^{-3})
GaAs	1.424	5.6533	5.32
InSb	0.17	6.4794	5.77
InAs	0.354	6.0584	5.68
GaSb	0.726	6.0959	5.61

Table 2.1: Bulk physical properties of common III-V semiconductor alloys used in fabricating QD and QW systems

x-rays [57].

2.7.2 Droplet Heteroepitaxy InSb quantum dots

InSb dots are of technological importance as active media for optoelectronic devices operating in the mid-infrared region. They have been proposed as suitable candidates for improved laser performance, mid-infrared detectors and light emitting diodes[58]. The physical properties of bulk InSb and other common III-V quantum dot systems are summarized in table 2.1. QD systems are advantageous over their QW analogues because charge confinement in all three directions makes the absorption of normal-incident light possible.The singular density of states of QDs is also an important factor in the efficiency and sensitivity of these devices. InSb have been deposited on a variety of substrates including GaAs and GaSb.

Shusterman *et al.* have reported the growth of InSb on a variety of substrates [59, 58] using droplet heteroepitaxy (DHE) using MOCVD. The method involves the deposition of Group III droplets on a substrate and the subsequent exposure of the dots to a G-V flux which crystallizes the droplets to form quantum dots. The DHE method is advantageous because unlike the S-K growth mode, it can be used for lattice-matched systems. It is also theoretically possible to produce patterned arrays of dots if one can control the position of the droplets using masks.

An analysis of InSb/GaAs dots by Kelvin Probe Force(KPF) and Photoluminescence Measurements(PL) measurements, has shown that there is considerable

deviation in the composition of the dots from the nominal InSb compound to a graded $InAs_xSb_{1-x}$ alloy composition with the dots containing as much as 80% As [59, 58]. These authors also find enhanced dot properties when the dots are grown on As-terminated surfaces compared with Sb-terminated surfaces. This compositional modification is crucial in enabling a reduction in the strain energy without the formation of misfit dislocations.

The possibility remains that additional effects such as In-Ga exchange and In-segregation which have been observed during the growth of InAs on GaAs, play a non-negligible role in the formation of InSb and InAs dots.

At present, there is no definite theory available in the literature to explain how DHE quantum dots form; insight gained from applying the COBRA technique to these systems is expected to shed more light on this question.

2.8 Anticipated Challenges

A number of challenges arise when conducting diffraction experiments on an ensemble of particles with varying sizes and composition and non-uniform distribution. The probe beams commonly used in COBRA experiments are on the order of hundreds of microns while the average size and dot to dot spacings are on the order of tens of nanometers [42]. Thus, features such as composition and strain variations obtained in COBRA experiments are averaged over the beam coverage area. The ideal situation would be one in which the dots have a high surface density and are identical in shape, size and composition.

However, variations in the dots have to be expected [46]. It is worthwhile to explicitly state that the goal of the project would not be to characterize individual dots, but to obtain information related to the average behavior of the dots.

Synchrotron x-ray beams have a finite transverse coherence length (ie. the length scale on which the x-rays are in phase) due to the slightly divergent nature of the beam. The transverse coherence length is defined by the size of the source and the distance of the source from the sample. The source size, L, is defined by a set of slits with an opening usually on the order of 100 x 100 μm^2 placed a distance D, about 4 meters away from the sample. The effective transverse coherence length, L_T, for a given wavelength λ, is given by the relation:

$$L_T = \lambda \frac{D}{L} \tag{2.36}$$

The transverse coherence length of the x-rays used in this study is on the order of 0.5 μm, and much larger than the dot dimensions, thus, the results provide a statistical average over dots within approximately a 100x100 μ m^2 area. The information provided by COBRA includes the average composition and the average displacement of atoms in the dot relative to positions of the substrate atoms as a function of the distance from the interface.

Although the current advances in microfocusing of x-ray beams down to less than 100 nm [60] exists using Fresnel zone plate optics and Kirkpatrick−Baez reflecting mirrors[61] which would permit single dot studies, the intensity suffers a drastic decrease. Suzuki *et al.* report a 5% x-ray efficiency for producing ∼30 nm spot sizes using the 3rd order focus of zone plates for 8 keV x-rays. Stephenson *et al.* also recently demonstrated focusing of 19.5 keV x-ray beams to ∼30 nm with 44% efficiencies and presented theoretical calculations to support the possibility of reducing the spot size further to 1-5nm using Multilayer Laue Lens optics (MLL) [62]. The latest focusing devices are more efficient. Reliable COBRA measurements require a dynamic range of about 3 orders of magnitude for relatively heavy atomic species such as In, Ga and As[29]. This option would left for future studies as brighter

sources such as free electron lasers become more readily available.

If the variations are expected to be centered around a mean set of parameters going from one particle in the ensemble to another, then it is reasonable to assume that these deviations would be introduced as noise in the data obtained. Thus there would be a direct correlation between the particle variation and the noise. This would impose a limitation to what conclusions can be confidently extracted from the data interpretation. On the other hand, by pushing the COBRA technique to its limit, we would be gaining insight into the strengths and inherent limitations of the technique.

CHAPTER III

Experimental Section

3.1 Experimental Section

3.1.1 Introduction

Surface diffraction experiments involve scattering from a few atomic layers and therefore require high intensity x-ray sources to obtain appreciable signals. Conventional laboratory based x-ray sources such as rotating anodes and sealed tube sources can provide brilliance up to 10^3 photons/s/mrad^2/mm^2/per 0.1% bandwidth and are well suited for studying thick films and bulk materials. Third generation synchrotron sources on the hand, are designed to produce x-ray brilliances more than 10^{15} times that of conventional lab sources. This makes them more suitable for the experiments performed in this study. Synchrotron sources are also advantageous due to the tunability of the x-ray wavelength to accuracies less than a fraction of an electron volt with a narrow bandwidth over a large x-ray energy range.

Two synchrotron sources were used for the measurements presented in this thesis: the 7 GeV Advanced Photon Source located at the Argonne National Laboratory in Argonne, IL and the 2.8 GeV Swiss Light Source located at the Paul Scherrer Institute in Villigen, Switzerland.

The basic principle of operation of third generation sources is as follows. Electrons are accelerated by bending magnets in a circular storage ring until they attain speeds

of about 99.999% the speed of light. At these relativistic speeds, the electrons emit x-ray radiation in a narrow cone around the forward motion of the electron beam. The opening angle of the cone is inversely proportional to the relativistic gamma factor. For an undulator, the cone angle is even narrower. The production of x-rays occurs either directly at the bending magnet dipoles, or in insertion devices such as wigglers and undulators located in the straight sections between the bend magnets. The insertion devices consist of alternating magnetic fields which force the electrons to follow oscillatory paths.

The x-ray beam produced is then monochromated and focused further before it reaches the sample.

3.1.2 Diffraction Experiments with the Pilatus

To speed up the sample alignment, and increase the signal to noise ratio of the measured diffraction intensities and increase the accuracy of the removal of background prior to data analysis, the Pilatus 100K two-dimensional pixel detector [28, 63] was integrated for Bragg rod measurements.

The Pilatus detector is a single photon counting detector which directly converts single x-ray photons into electric charge. It is composed of a 2D array of silicon-based p-n diodes connected directly to an array of readout channels by microscopic indium balls ($18\mu m$ diameter) by a novel process called microbump-bonding. This design is advantageous in that no dark current or readout noise is produced; short readout times less than 3ms and framing rates as high as 200 Hz are permissible and the detector has a high dynamic range of 10^6 (20 bits). The use of silicon allows a counting rate of $2x10^6$ counts/pixel/s for high flux at synchrotron sources.

A schematic of the Pilatus pixel is shown in Fig 3.1. Incident x-rays produce

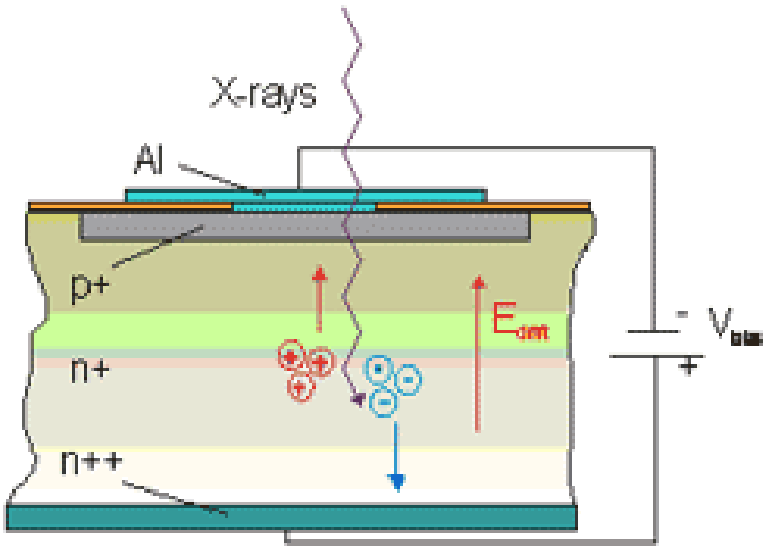

Figure 3.1: Pilatus pixel schematic

electron-hole pairs in the p-n diode active region. These electron-hole pairs are separated by a bias applied to the p-n diode and read out by the readout channels.

Threshold settings with the Pilatus

Experiments were carried out close to the K-edges of the constituent elements of the samples we studied. These energies lie a few eV above fluorescence lines. To avoid including the sample fluorescence in the integrated diffracted intensity, the Pilatus detector was gated to count photons only above a threshold energy which was set to be above the fluorescence energy of the sample but below the energy of the elastically scattered photons. This was achieved by adjusting the bias on each pixel.

The detector is usually calibrated at a set of energies by exposing the detector to scattered x-rays at the desired energy and adjusting the thresholds on each pixel till it no longer records any counts. Once the calibration is complete, the threshold can be set for any energy by interpolating between the calibrated points.

All the pixels in the detector may not have a uniform response due to dead pixels, accidental exposure to the direct beam etc and it is critical that a flatfield is obtained before and after each dataset is collected. This flatfield is obtained by exposing the detector to a uniform field of x-rays. This is usually done by exposure to uniform diffuse elastic scattering from a polycrystalline source such as lead glass. To obtain good statistics, we average 100 images each exposed for 10 seconds. The flatfield correction is obtained by normalizing the average image obtained to the mean pixel intensity. An example of a flatfield obtained at 10.365 keV with threshold set to 10 keV is shown in Fig.3.2. The prominent vertical and horizontal streaks observed in the flatfield occur at the boundaries between the detector modules.

3.1.3 Experimental Setup

For a careful measurement of diffraction intensities, it is essential that the sample, diffractometer (device which rotates the sample and detector to satisfy diffraction conditions) and detector are aligned as accurately as possible to within a few μradians. The diffraction experiments begin with an initial alignment which involves:

1. an initial determination of the goniometer rotation axes
2. aligning the sample and detector with respect to the incident beam
3. determining the orientation matrix i.e., the angular coordinates which define the crystal orientation of the sample relative to the axes of the diffractometer.

Once the alignment procedure was completed, Bragg rods were recorded by moving the sample and detector to satisfy diffraction conditions along the Bragg rods and recording the diffraction intensities at each point.

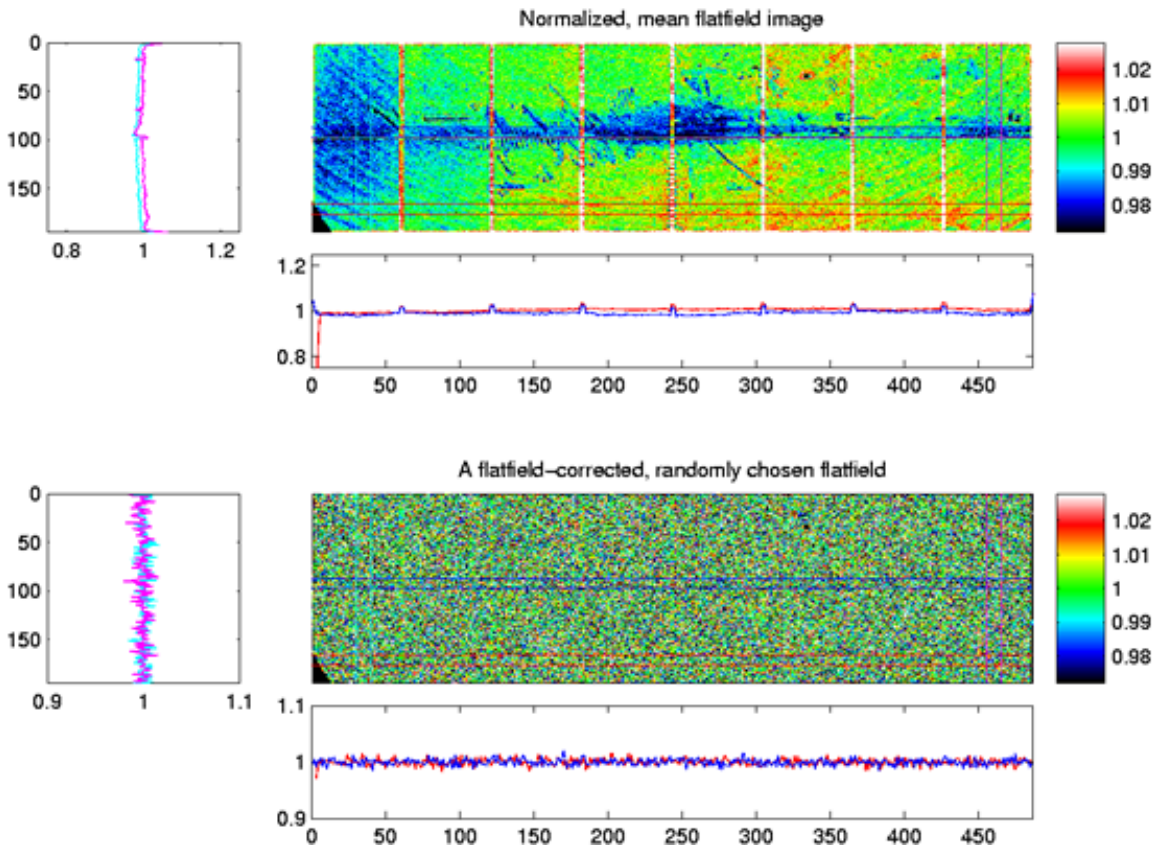

Figure 3.2: Flatfield of Pilatus detector response obtained at 10.365 keV with a threshold set to 10 keV. The top panel shows the normalized flatfield correction image obtained by normalizing 100 10sec exposures to the mean intensity. The image in the bottom panel shows a randomly chosen flatfield image corrected with the image in the top panel.

Sample alignment

The sample is aligned such that in its zero position, the sample surface is parallel to the incident beam and the sample cuts the diffracted beam in half. The sample surface is aligned as follows: With the diffractometer positions set to zero, the sample is mounted on the goniometer head and phi rotated so that the kozu arcs lie in the horizontal and vertical planes. A HeNe laser is set up so that it reflects off the sample onto a screen.

The reflection is marked on the screen and the sample is rotated 180^o about the

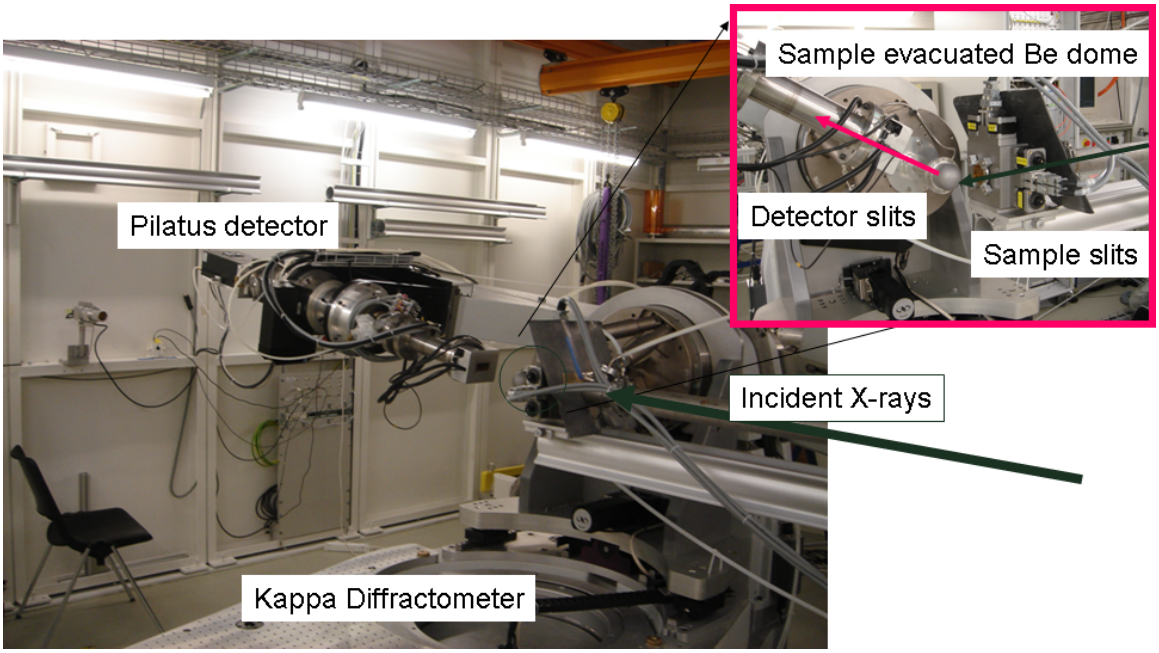

Figure 3.3: Diffraction Experimental setup at the material science beamline, Swiss Light Source

ϕ axis. The new position on the screen is noted and a point halfway between the original and final reflection is determined by drawing a line from the two points and measuring the point halfway. The sample kozu arcs are adjusted to tilt the sample so that the reflected beam goes to the new center position. Rotating phi back 180^o should result in the reflected beam staying in the same position. If it moves, the procedure is repeated for a finer adjustment.

The sample surface should now be parallel to the x-ray beam. The next step is to adjust the sample height so that the sample cuts the incident beam in half. This step requires the beam and the detector are positioned to observe the direct beam. Filters are required when the detector is in the path of the direct beam to avoid radiation damage. Note this assumes that when the angle μ is at zero, the sample surface is parallel to the beam. To check the μ alignment, first adjust the sample height till sample cuts beam in half. Rotate $\mu \pm 0.1^o$ about the zero position. The

maximum should be at the zero position. If it is not, move mu to the position where the intensity is maximum and reset the value of μ to be 0 at this position. Keep it at this position and do the coarse and fine sample height adjustment. Repeat the μ scan and iterate as necessary.

Finding the orientation matrix

The user has to set the x-ray wavelength and initial unit cell parameters. Based on these parameters, an approximate orientation matrix is calculated by SPEC (or LABVIEW). The sample is moved to three non-collinear reflections and the sample and detector angles are optimized to maximize the intensity of the reflections. These refined reflections are then used to calculate a new optimized orientation matrix. The matrix can be optimized further by moving to more reflections and optimizing their angles. Usually, a total of 6-7 reflections are used to determine the final orientation matrix for the sample.

3.1.4 Recording data

Once the sample is aligned and the orientation matrix is obtained, diffraction intensities are measured along Bragg rods using a macro in which one defines the h and k coordinates, the start and end values for l and the integration time per point.

The sample is mounted inside a hemispherical Be dome and evacuated to a vacuum of about 10^{-6} Torr to prevent radiation induced oxidation damage to the sample. Evacuated flight paths are also installed between the sample and detector to reduce background air scattering. A set of slits are also installed after the sample to prevent forward diffuse scattering from the sample, the sample mount and Be dome from reaching the detector.

At each data point, an exposure time (usually about 10 seconds) is chosen to

maximize the signal to noise ratio. An automatic scheme is employed to increase the integration time at points with low diffracted intensities and to automatically adjust filters to increase the effective dynamic range of the detector. The filter material depends on the x-ray wavelength. A series of filters with different thicknesses are used to change the incident beam intensity if the intensity detected by the Pilatus is above a set threshold. The use of the filters also prevents the detector from damage by high flux radiation.

3.1.5 Data extraction

During the data collection, a 2D image is saved for each data point. Post-measurement data extraction involved first normalizing each image to the flatfield mask to correct for the inhomogeneous detector response.

In summary, data extraction involves carefully identifying the background and subtracting the background from the signal of interest. Sources of background noise include diffuse scattering from the sample, air scattering, scattering from the sample holders and from the beryllium dome which is used to keep the sample under vacuum. There is no intrinsic noise (e.g., thermal or electronic readout noise).

Two schemes were used to extract the signal. One involved fitting the background to a 2D linear, constant, or Gaussian function and subtracting this fit from the signal.

A second scheme was to convert the 2D image into a line detector. This involved projecting the image in a rectangle defined around the signal into a single line. The background was fitted to a 1D Gaussian or polynomial function and subtracted. A LABVIEW program was developed for this approach.

3.1.6 Corrections to Data

After the flatfield corrections and background subtraction are carried out, corrections are applied before analyzing the data with COBRA.

Polarization Corrections

The x-rays from synchrotron sources are polarized and the effective I_o depends on the angle of incidence of the beam on the sample. This effective intensity has a cosine dependence and has to be corrected for when determining the structure factors.

Lorentz factors

Lorentz corrections have to be taken into account since the detector intercepts the Eswald sphere differently for different points along the Bragg rod.

Beam footprint

The effective diffraction volume is determined by the angle of incidence of the beam on the sample. This angle is fixed for off-specular rods in constant footprint mode, however, it varies for the specular rod and has to be corrected for. This correction has a $1/sin\theta$ dependence where θ is the angle between the incident x-rays and the sample surface.

CHAPTER IV

Results and Discussion - GaAs temperature study

4.1 Introduction

As a first step to understanding strain relaxation in quantum dot systems, the anomalous response of the atomic x-ray scattering factor was used in conjunction with the Coherent Bragg Rod Analysis phase retrieval algorithm[64] to investigate the strain and composition profiles in moderately tensile strained ultrathin layers of GaAs films grown on InGaAs buffers.The similarity of this system to QDs lies in the fact that island formation also occurs in this system to relieve strain energy. The islands in the GaAs/InGaAs system are thin enough that they would remain pseudomorphic with the substrate. In addition to the expected excellent registry, the possibility of the films being alloyed due to intermixing with the buffer made this system an excellent candidate to test the anomalous-COBRA technique.

The samples were prepared in Prof. Mirecki Millunchick's lab at the University of Michigan. Lee et al. previously studied the surface morphology of this system as a function of GaAs growth temperature using *in vacuo* scanning tunneling microscopy and observed increased coarsening of the surface with increased growth temperature [65, 66, 67]. This trend was attributed to the Asaro-Tiller-Grinfield instability[68]. While surface coarsening relieves strain, the observed tendency of of In to segregate

to the InGaAs buffer surface [69, 70, 71] prior to GaAs deposition means that a deviation in the composition of the as-deposited film should also be expected. This change in composition would also contribute to strain relaxation.

X-ray probes are an excellent tool for characterizing these systems: they are nondestructive and have a high penetration power for studying buried structures and interfaces. Morever, the ability to tune x-ray energies at synchrotron sources also enables element specificity for quantitative studies of intermixing in self-assembled coherently strained systems[72, 73, 74].

COBRA has been applied successfully to provide sub-Ångstrom-resolution information on several epitaxial systems[75, 34] with in-plane periodicity and out-of-plane aperiodicity. The structure of a system is determined from complex scattering factors (CSF) measured along substrate-defined Bragg rods. The measured x-ray intensity provides the amplitude of the CSF but not the phase. The COBRA method is used to retrieve the phase information. The Fourier transform of the COBRA-determined CSFs provides a 3D electron density (ED) distribution function for the system with Gaussian-like peaks representing atomic sites. The structure of the system can be determined from the positions of the ED peaks with sub-Ångstrom resolution. The volume integral of these peaks is proportional to the x-ray energy dependent effective EDs of the atomic species occupying those positions. A normalization factor is usually obtained relative to the ED peaks deep inside the substrate where there are no deviations from the nominal bulk structure; in this way it is possible to determine the chemical distribution in the system.

In the vicinity of the interfaces and close to the top surface where the composition and coverage may not be known *a priori*, it is a non-trivial matter to determine which elements contribute to the ED peak and what their relative fractions are.

Energy	In	Ga	As
10.365 keV	49.05	19.56	31.2
11.865 keV	48.89	29.99	21.5

Table 4.1: Variation of the real part of the atomic scattering factors of In, Ga and As with x-ray energy

To resolve this ambiguity, we compare two COBRA-determined ED maps for the GaAs/InGaAs/InP system obtained from Bragg rod measurements close to, and well above, the Ga K-edge. The second energy was selected to be close the the As edge so that simultaneous sensitivity to the composition of the G-V(group V) layers would be achieved. Table 4.1 shows the complex scattering factors (CSF) of Ga, In and As at 10.365 keV and 11.865 keV.

The difference in the energy-dependent ED maps permits an accurate determination of the relative concentrations of Ga and In as a function of the distance from the interface, independent of the effects of incomplete monolayer coverage. This makes the anomalous-COBRA technique particularly suitable for alloyed systems exhibiting significant compositional intermixing and interfacial/surface roughness. In this chapter, it is shown from the observation of COBRA-derived vertical concentration profiles of this system that, on deposition of two ML of GaAs on the InGaAs buffer, an interplay between In alloying and surface coarsening leads to a reduction of strain.

The buffer layers were nominally latticed matched with InP substrates and the subsequent GaAs growth was compared at two different temperatures: 480^o C and 520^o C. A more detailed determination of the structure of this system using a-COBRA was expected to reveal more information about the composition and strain profiles of the surface islands and the top monolayers of the buffer. It is shown that electron density maps extracted from Bragg rod scans measured close to the Ga and As K-edges can be used to deconvolute roughness and directly determine intermixing.

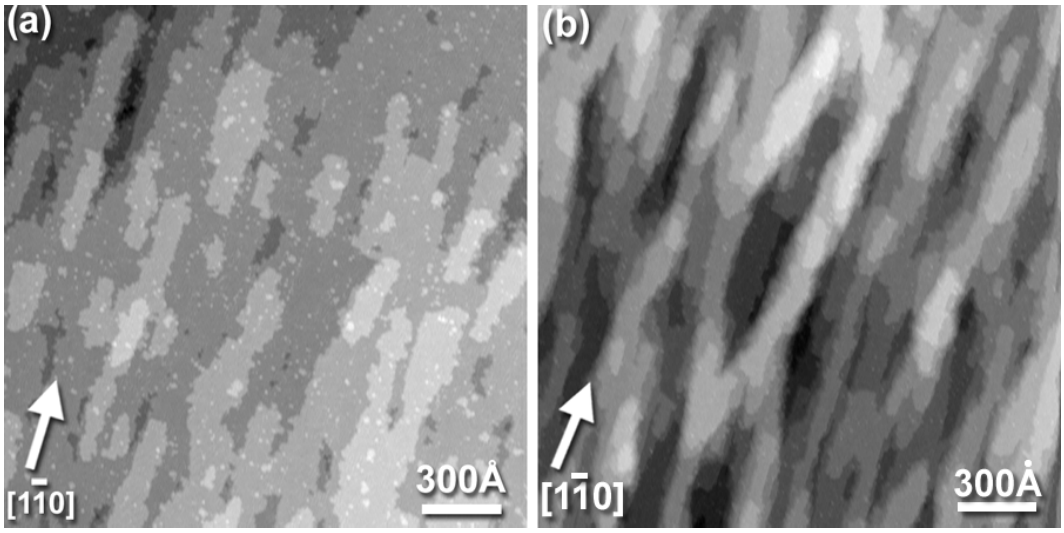

Figure 4.1: STM images for 2 ML thick GaAs films on lattice-matched $In_{0.53}Ga_{0.47}As$/InP grown at (a) 480^o C, and (b) 520^o C[67].

It is found that indium incorporation and roughening lead to a significant reduction of the strain in this system.

4.2 Experimental Details

4.2.1 Sample Preparation

The samples were grown using solid-source molecular beam epitaxy using As_4. The composition, deposition rate, R_{Ga}, and As flux, F_{As} were calibrated using Reflection High Energy Electron Diffraction oscillations, and the growth temperature was measured using an optical pyrometer[67]. $In_{0.53}Ga_{0.47}As$ buffers were grown lattice-matched to InP(001) substrates at 480^o C, followed by the growth of two monolayers(MLs) of GaAs at either 480^o C(R_{Ga} = 0.05 ML/s, F_{As} = 1.5 ML/s) or 520^o C(R_{Ga} = 0.20 ML/s, F_{As} = 1.5 ML/s). For the latter film, the buffer was heated to the desired temperature over 5 minutes under an As_4 flux prior to the deposition of the film.

The RMS roughness of these strained films determined by STM measurements

over 2x2 μm areas, increases with increasing growth temperature, from 0.17 nm at 480^o C to 0.35 nm at 520^o C. At 480^o C (Fig. 4.1(a)) the surface exhibits two-dimensional islands in addition to a terrace structure similar to that of the buffer. At 520^o C (Fig. 4.1(b)), the terrace structure is obscured and the morphology consists of narrow mesas and troughs. The roughening of these films has been attributed to an increase in the group-III adatom population due to the desorption of As from the surface[67].

4.2.2 X-ray Diffraction Experiments

Surface diffraction experiments were carried out at the Material Science beamline at the Swiss Light Source, Paul Scherrer Institute, Switzerland. For each sample, twelve symmetry-inequivalent rods and four equivalent rods were obtained at 10.365 keV and 11.865 keV, with an energy resolution $dE/E = 10^{-4}$. The energies were selected to be 2 eV below the Ga and As absorption edges, respectively, to take advantage of the anomalous dispersion of the respective atomic structure factors with x-ray energy. Diffraction intensities were recorded using a Pilatus 100k pixel detector with appropriate energy threshold settings to suppress the detection of fluorescent photons from the sample[28] and consequently, enhance the signal-to-noise ratio. Samples were placed in an evacuated chamber with a beryllium window during data collection to prevent sample oxidation due to the high x-ray flux.

The angle of incidence of the incoming beam was fixed at 0.5^o, close to the InGaAs critical angle to eliminate the contribution of the InP substrate to the diffraction intensity. The attenuation length of InGaAs for 11.865 keV photons at an incident angle of 0.5^o is $0.17\mu m$. The x-rays would have to pass through 0.5 μm of InGaAs to reach the InP substrate. The transmission through the buffer is $e^{-\frac{0.5}{0.17}} = 0.05$.[1]

[1]On the other hand, if the incident angle is 5^o, the attenuation length of of the InGaAs buffer is about 2 μm

For each sample, an ED map was obtained for each of the selected energies using COBRA. The difference in the ED maps were used to determine, quantitatively, the composition of the two systems. A comparison of the Bragg rods recorded at the 2 energies is shown for the 480^o C sample (Fig. 4.2) and the 520^o C sample (Fig. 4.3).

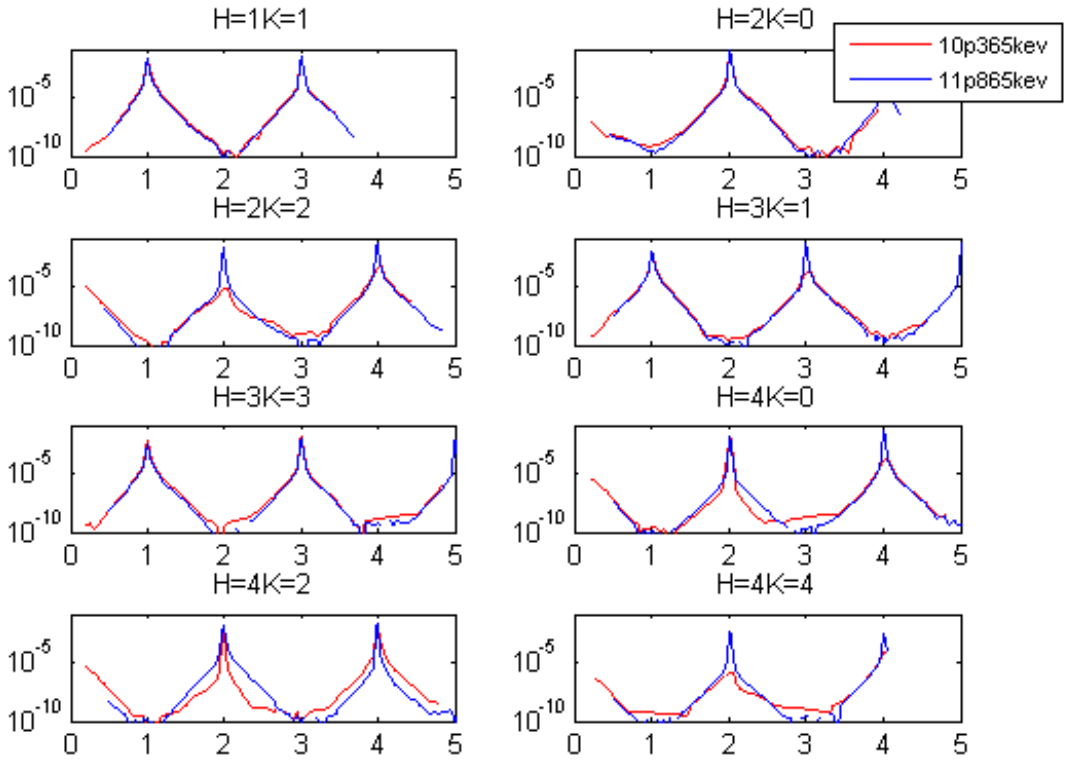

Figure 4.2: Comparison of some of the measured rods at 10.365 keV and 10.865 keV for the GaAs sample deposited at 480^o C.

4.2.3 COBRA Analysis

The angle of incidence was fixed at 0.5^o for the off-specular rods to be close to the critical angle of InGaAs to enhance the contribution of the surface layers to the diffracted intensities and effectively prevent the InP substrate from contributing

and 77% of the incident x-rays interact with the InP. In this situation, the InP substrate contribution is no longer negligible.

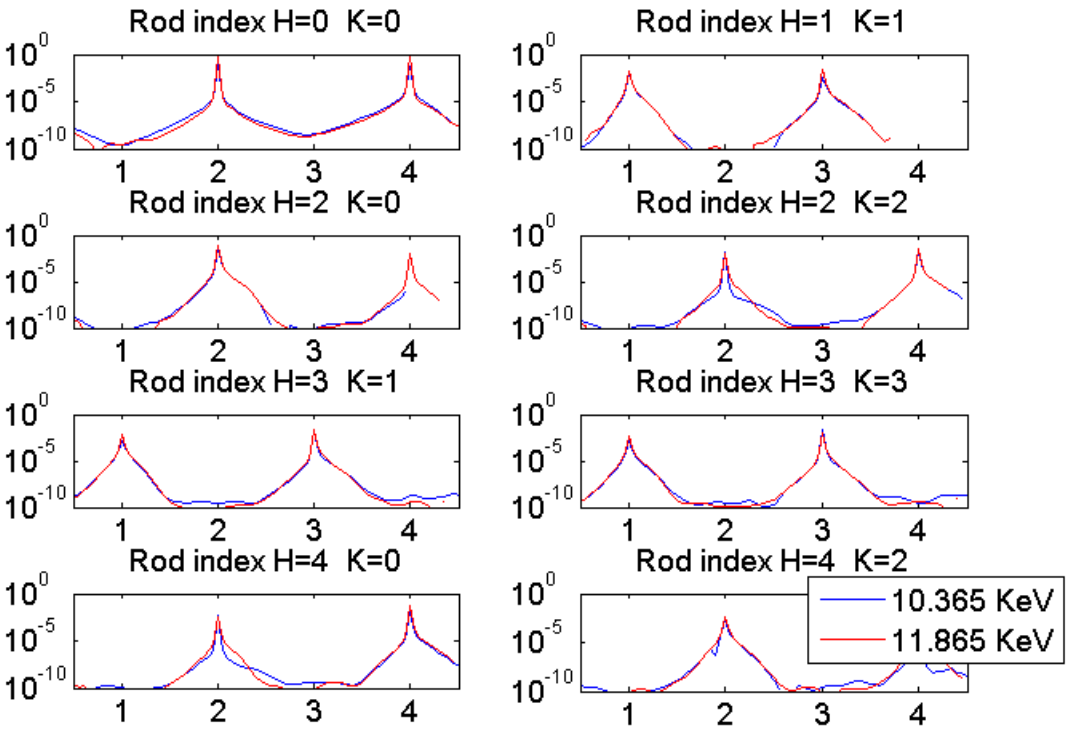

Figure 4.3: Comparison of some of the measured rods at the 10.365 keV and 10.865 keV for the GaAs sample deposited at 520^o C.

to the measurements. Thus, in calculating the reference structure for the COBRA analysis, the system was considered to comprise of a semi-infinite bulk $In_{0.53}Ga_{0.47}As$ substrate with a 2 ML thick GaAs film. The analysis for each energy began with an initial fit of the Debye-waller factors, multiplicative constants and a roughness parameter for the film to determine the initial reference structure. This fitted initial reference does not represent the true structure of the system, however, as a result of the fit, the amplitudes of this reference are on the same order of magnitude as the experimentally measured amplitudes as is required for the COBRA approximation to be valid.

Once a good reference was determined, the COBRA method was iteratively ap-

plied until convergence of the sum of squares of the differences between the COBRA calculated intensities and the measured intensities was achieved and the negative parts of the real space ED were minimized. Convergence was attained for all the samples after 8-10 phasing iterations.

A couple of features emerged after the results converged. First, the rough region at the top surface of the system extended about 4 ML for the 480^o C sample and 6 ML for the 520^o C in contrast with 2 ML in the reference. Secondly, there was a continuous relaxation of the out of plane atomic layer spacings in the 'rough' region. Lastly, while the ratio of the integrated electron densities of the G-III to G-V layers was constant in the substrate region of the system, there was a continuous change in the top monolayers of the system indicative of a compositional gradient.

Large iterations

Each successive phasing iteration inherently introduces some level of noise because the COBRA ansatz is an approximation, which becomes more valid if the initial reference is closest to the ideal. The interpolation of unreliable data points around the substrate Bragg peaks, and the limited volume of reciprocal space experimentally measured, also introduces noise in the system.

Although the noise does not alter significantly the qualitative results obtained, since only high Z elements are present in this system, further refinement was necessary to obtain more accurate quantitative parameters.

The refinement was achieved using what is referred to as a COBRA large iteration. For the large iteration, a new reference model was obtained using the atomic positions and integrated electron densities of the previous COBRA-determined structure. The DW factors were refined again. COBRA phasing iterations were then applied using

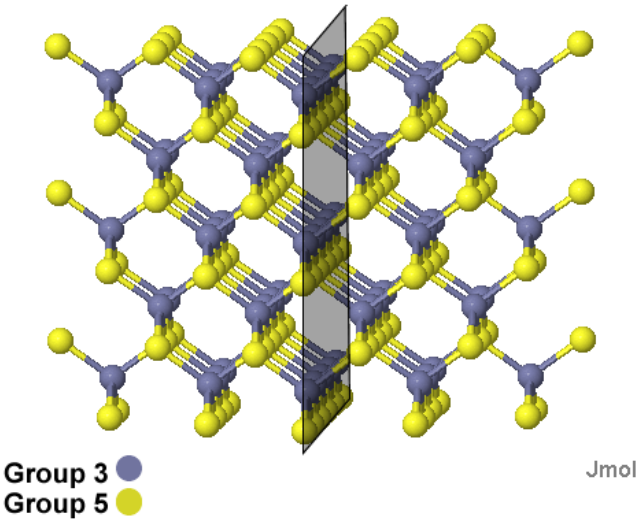

Figure 4.4: Zincblende crystal structure. The shaded cut indicates the [110] plane

the refined model as the initial reference. In this case, convergence occurred after only 2-3 phasing iterations.

4.3 Results and Discussion

For each sample, the layer-by-layer composition and coverage profiles were determined by comparing the ED maps obtained independently for the 2 x-ray energies.

The system has a zincblende structure; thus it can be considered to be alternating layers of group III atoms (InGa) and group V atoms (As). A monolayer (ML) consists of one G-III atomic layer (AL) and one G-V AL [2].

Coverage profile

At each energy, the vertical profile of layer coverage, θ_z, can be obtained by directly normalizing the COBRA-derived As ED peaks to the expected effective number of electrons for As at the respective energy. For each sample, it is found that θ_z, calculated both at the Ga and As edge, are equivalent, indicating that there is

[2]The zincblende structure is defined to have 2MLs per unit cell

no intermixing between the G-III and G-V sublattices, i.e., there is an insignificant density of anti-site defects.

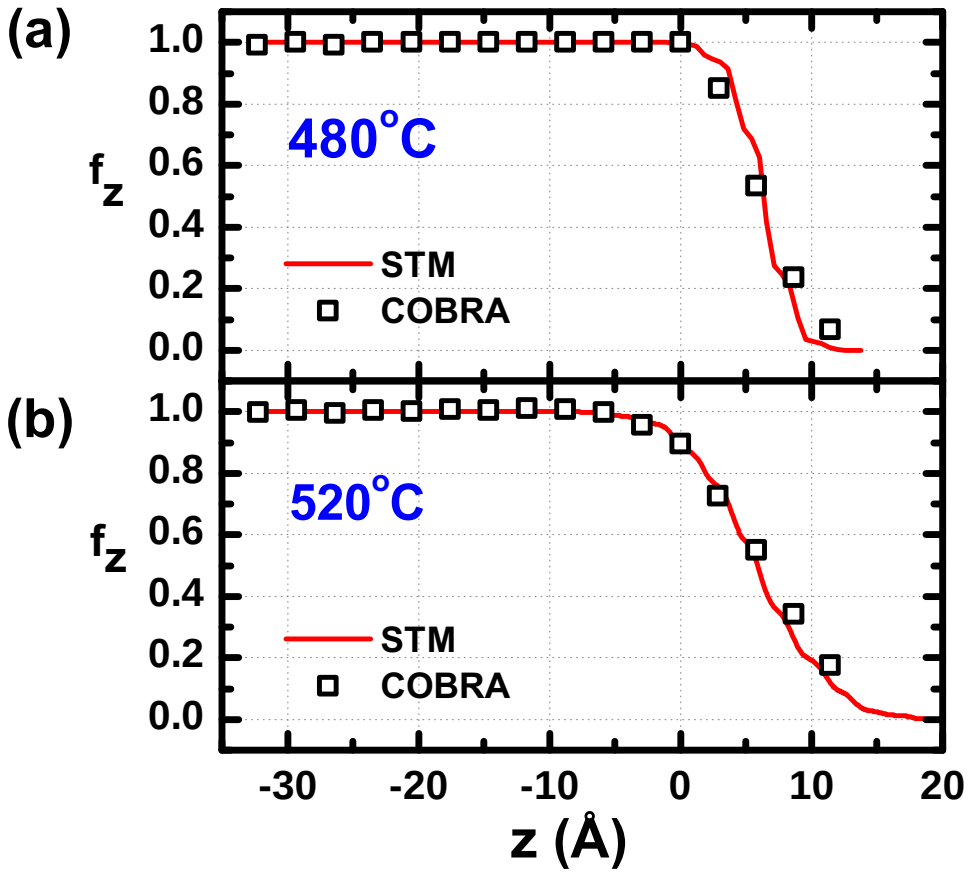

Figure 4.5: COBRA-determined vertical fractional occupancy, f_z, profiles for 2 ML GaAs/InGaAs system grown at (a)480^o C and (b)520^o C . Occupancy profiles extracted from STM images in Fig. 1 are shown for comparison. Note that zero is the nominal position of the interface.

To verify the COBRA derived coverage profile, we compare coverage profiles extracted from the STM images in Fig. 4.1 with the profiles obtained independently from COBRA for the samples grown at 480^o C, Fig. 4.5(a), and 520^o C, Fig. 4.5(b). The regions with $\theta_z < 1$ correspond to roughness at the film surface. The profiles determined by STM and COBRA are in excellent agreement, with any differences attributed to the different effective probe areas, and the fact that the topmost layers observed with STM with low occupancies contribute little to the x-ray intensities,

and therefore are not imaged by COBRA.

Composition Profiles

The composition of each layer can be determined as follows: for each group-III layer comprising both In and Ga, let T_{10} and T_{11} be the total ED for that layer obtained from COBRA at 10.365 keV and 11.865 keV respectively. We can now separate the fractional contributions for a given layer of In, x^{In}, and Ga, x^{Ga}, at the two energies:

$$T_{10} = x^{In} In_{10} + x^{Ga} Ga_{10} \tag{4.1}$$

$$T_{11} = x^{In} In_{11} + x^{Ga} Ga_{11} \tag{4.2}$$

where the subscripts 10(11) refer to the corresponding atomic scattering factors for In and Ga at 10.365 keV(11.865 keV). It is straightforward to solve algebraically for x^{In} and x^{Ga}.

The In content, x^{In}, as a function of depth, is compared for the two growth temperatures in Fig. 4.6(a). The composition deep in the buffer for both samples, is $In_{0.53}Ga_{0.47}As$ as expected, however, both samples show significant In-incorporation into the nominal GaAs film. The In composition[3] of the films at both growth temperatures in Fig. 4.7 is about 40% near the film/buffer interface and close to 20% at the surface.

By integrating the In content shown in Fig.4.6(a) for the two samples, we observe that the 520^o C sample contains a net 0.19 ML less In than does the 480^o C sample, indicative of enhanced In desorption at 520^o C. Using the previously reported[76] Arrhenius-type dependence of the desorption rate, we calculate the amount of In loss

[3]The Indium composition is calculated as $\frac{x^{Ga}}{x^{In}+x^{Ga}} * 100\%$

at 480^o C and 520^oC . For a prefactor $\nu = 2.6 \times 10^{13} s^{-1}$ and desorption activation energy $E_D = 2.57$eV[76], the calculated amount of In desorbed at 480^o C is 0.03 ML and 0.2 ML at 520^o C, consistent with our experimental values.

Strain Profile

Accounting for the Poisson ratio of InGaAs, we can estimate the strain in each ML, based on the measured composition $x_{In}(z)$ and the measured out-of-plane lattice spacing a_{meas}, assuming pseudomorphic growth (i.e., the islands are lattice-matched in-plane with the substrate):

$$a_{In}(z) = (x_{In}(z) * 0.4051) + 5.6563 \tag{4.3}$$

$$strain(z) = -\frac{a_{meas}(z) - a_{In}(z)}{a_{In}(z)} \cdot 100\% \tag{4.4}$$

where a_{In} is the calculated bulk lattice parameter for the measured In content.

Figure 4.6(b) shows profiles of the in-plane strain at the two growth temperatures. The strain is zero deep in the buffer, as expected. Both films are in tension with the strain gradient being more gradual for the 520^o C sample with a maximum strain of 0.68% compared with 1.01% for the 480^o C sample. Note that a much larger strain(3.7%) is expected based on the nominal lattice mismatch between the buffer and GaAs.

4.4 Conclusion

The results obtained by COBRA are averaged layer-by-layer over the coherence length of the x-ray beam which is on the order of 500 nm. Thus, the analysis is not sensitive to lateral variations in composition and lattice spacing. However, we may assume in-plane uniformity in composition and lattice spacing in interpreting the observed composition and strain profiles since excellent film/buffer registry is

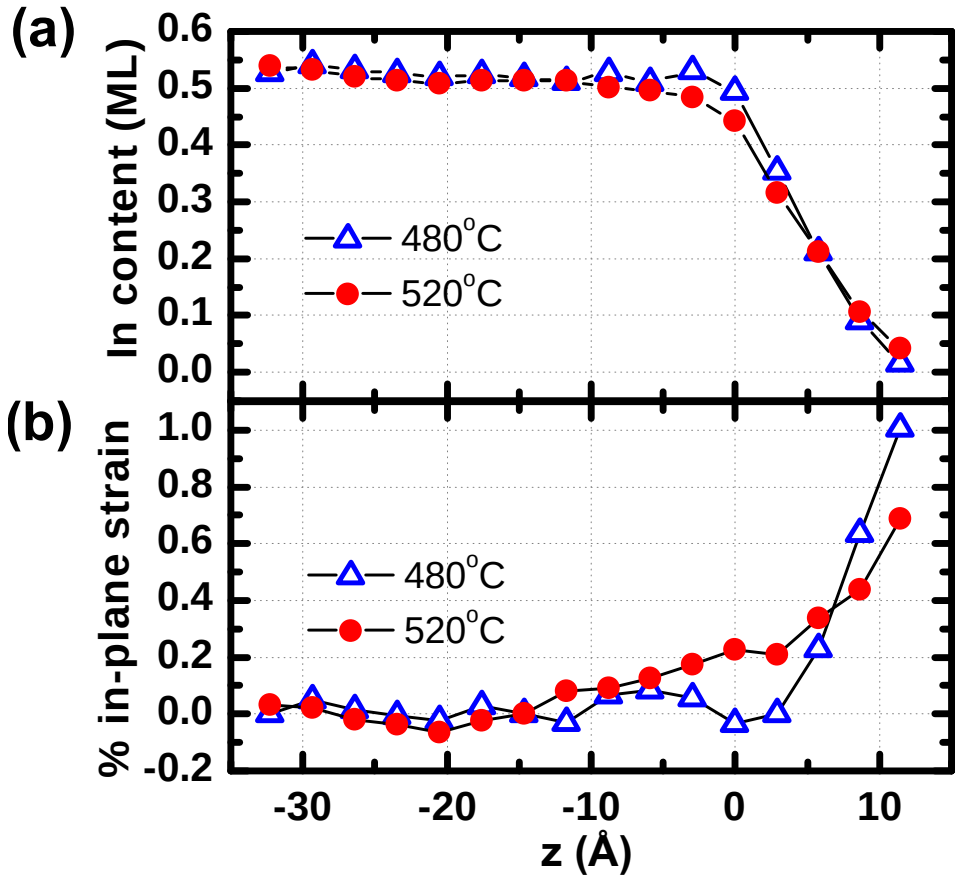

Figure 4.6: COBRA-determined (a)In content profiles and (b)in-plane strain profiles for the 2 ML GaAs/InGaAs system grown at 480^o C and 520^o C.

expected for ultra-thin films.

An In-rich surface has been shown previously to form during the growth of InGaAs due to In surface segregation[77, 69]. During the subsequent growth of the GaAs film this In-rich surface is incorporated into the film to form an InGaAs alloy. The determined strain profile shows that In-incorporation from the InGaAs surface into the film drastically reduces the mismatch strain from 3.7% to less than 1.0% by expanding the unit cell size of the film. In-incorporation into the film is highest closest to the interface, leading to the depletion of the InGaAs buffer surface. This causes a greater relaxation of misfit strain at the interface than at the film surface. Further relaxation occurs at higher film growth temperatures, due to roughening.

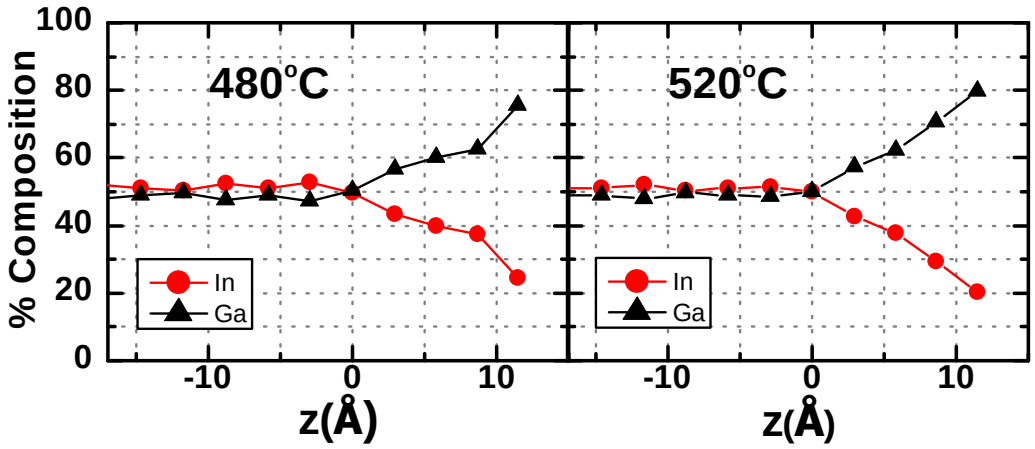

Figure 4.7: In and Ga composition profiles for the 2 ML GaAs/InGaAs system grown at (a)480^o C and (b)520^o C.

The total film In content is estimated from Fig. 4.6(a) to be about 0.7 ML for the 480^o C sample. No significant In depletion is observed in the buffer layers therefore the In in the film comes not from an In-Ga exchange with the buffer, but from the incorporation of an In floating layer. It is therefore plausible to postulate that the following processes occur during growth.

- The initial InGaAs buffer has an In-rich surface with composition $In_{0.70}Ga_{0.30}As$.
- On deposition of the initial layers of GaAs, coarsening occurs due to the motion of mobile In atoms towards the GaAs nucleation sites to reduce mismatch strain. The In incorporation is driven by both strain and diffusion.
- As more GaAs is deposited there is less In to be incorporated and thus, the mismatch strain increases and further coarsening occurs.

Strain fields less than 0.1% are observed extending 4MLs deep into the InGaAs buffer. Finite element analysis calculations on compressively strained InAs quantum

dots show that tensile strain is induced in the substrate [78]. The converse is true for the nominal GaAs/InGaAs: a tensile film is expected to induce compressive strain in the surface layers of the underlying buffer. The small, but significant tensile strain shown in Fig. 4.6(b) lends credence to the role of the dissolution of the floating In layer in relaxing strain in this system. It is therefore clear that to correctly model strain in these systems, theoretical calculations would have to take into consideration the role of In surface segregation.

The technique presented here provides valuable information about the chemical composition and distribution of strain in ultra-thin films of tensile-strained GaAs/$In_{0.53}Ga_{0.47}As$ for two growth temperatures. In-incorporation into the film serves as an effective mechanism for strain relaxation in this system.

CHAPTER V

Results and Discussion - Stranski Krastanow InAs dots on GaAs

5.1 Introduction

The spontaneous transition of strained two dimensional films into three dimensional homogeneous nano-islands, has attracted much scientific attention. This is referred to as the Stranski-Krastanow growth mode. The formation of the islands allows the system to reduce its energy by relaxing strain at the island surfaces. Finite element calculations indicate that the formation of islands also induces distortions in the substrate[56, 79, 80].

In addition to the island formation, an exchange of material between the deposited epilayer and the surrounding material occurs, resulting in modifications of the island composition and the surrounding material (i.e. capping layer and underlying substrate). The tendency of some of the constituent elements such as indium and antimony to preferentially segregate also leads to a complex structure of these systems.

To carefully control the growth of quantum dots and more precisely predict their opto-electronic behavior, a better understanding of the final structural states is required. The efficacy of the anomalous-COBRA method is studied to determine the atomic structure of Stranski-Krastanow grown InAs quantum dots and their inter-

faces.

5.2 Experimental Details

5.2.1 Sample Preparation

The InAs/GaAs QD samples were grown by the Goldman group at the University of Michigan on epiready [001] oriented GaAs substrates by molecular beam epitaxy, using solid Ga, In, and As_4 sources. The substrate temperature was monitored using an optical pyrometer. An initial 500 nm thick GaAs buffer layer was grown at 580^o C with a V/III beam-equivalent pressure ratio of 30. The GaAs buffer was annealed at 580 ^{o} C with As_4 followed by annealing at 530^o C with half the original As_4 flux and at 370^o C without As_4. After the buffer annealing treatment, 2.6 ML of InAs was deposited at 500^o C forming a high density of uniform QDs with dimensions on the order of 5-8 nm (height) and 50±5 nm (width)[81]. The 2D-3D transition was evidenced by a transition in the reflection high-energy electron diffraction pattern from streaks to spots.

Atomic Force Microscope Measurements

AFM measurements were carried out the University of Michigan Electron Microbeam Analysis laboratory using a Digital Instruments Nanoscope IIIa atomic force microscope in tapping mode. An AFM image of the sample is shown in Fig.5.2. The dots have high uniformity in shape and size with a density of about 1.25×10^{10} dots/cm^2. The dot heights are about 6-8 nm and with widths of about 50±5 nm. The dot dimensions are expected to be somewhat smaller than these numbers imply due to the overestimation by AFM as a result of the tip convolution.

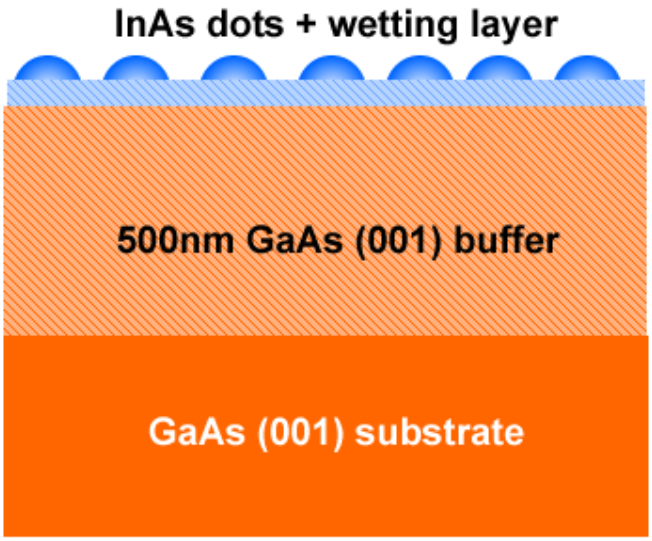

Figure 5.1: Schematic of Stranski-Krastanow InAs/GaAs sample

5.2.2 X-ray Diffraction Experiments

Surface diffraction experiments were carried out at the Sector 7-ID undulator beamline at the Advanced Photon Source, Argonne National Laboratory. Nine symmetry-inequivalent rods were obtained at each of the energies; 10.362 keV and 11.862 keV, 5 eV below the Ga and As absorption edges, respectively. The rods measured were the 00L, 11L, $1\bar{1}$L, 20L, 22L, 31L, $3\bar{1}$L, 33L, $3\bar{3}$L rods with L_{max}=4.5 r.l.u. and a sampling density of 40 points per GaAs reciprocal lattice unit. Diffraction intensities were recorded using the Pilatus 100K pixel detector with appropriate energy threshold settings. Samples were placed in an evacuated chamber with a beryllium window during data collection to prevent sample oxidation. The angle of incidence of the incoming beam was fixed at 5^o for the off-specular rods. The large angle was chosen in this case to minimize the footprint of the incident beam on the

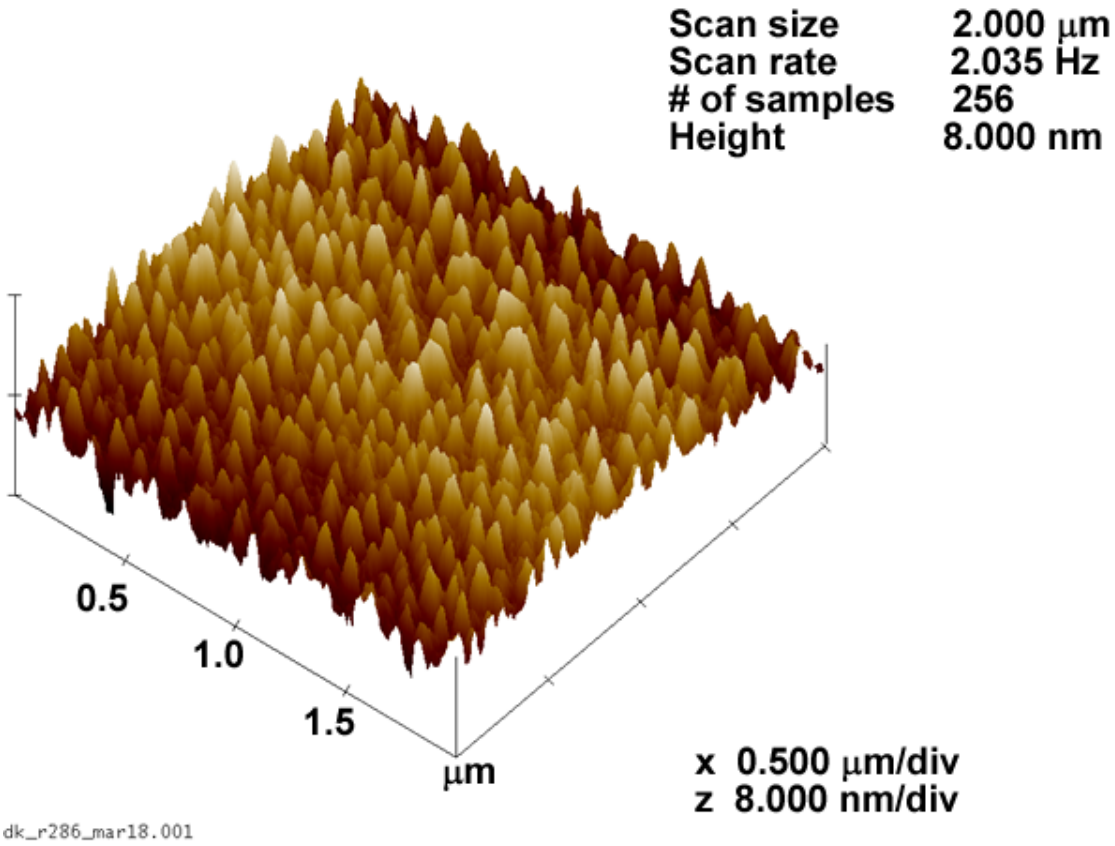

Figure 5.2: 2 μm x 2 μm AFM image of Stranski-Krastanow InAs dots grown on GaAs by molecular beam epitaxy. The dot density is estimated to be 1.25x10^{10} dots/$cm^2$with an average width of 50$\pm$5 nm

sample.

5.2.3 Anomalous-COBRA Analysis

The initial reference model was chosen to consist of a GaAs substrate with an exponentially decaying InAs film. This model did not take into consideration any information about the dot characteristics. As pointed out earlier, this is only the initial reference; details emerge from the COBRA phasing procedure, essentially independent of the initial reference. Convergence was obtained after 12-13 phasing iterations.

Refining the a-COBRA result by subsequent fitting is possible if the ED map

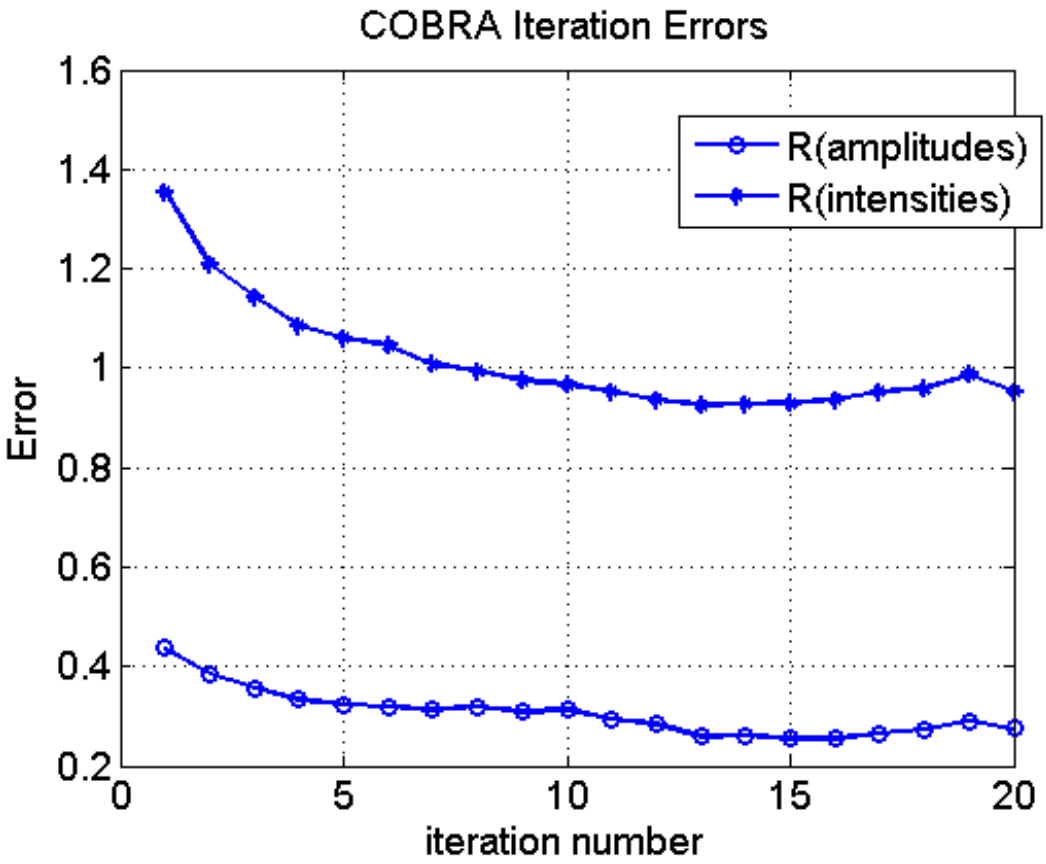

Figure 5.3: Progression of error parameters (defined in Chapter 2) with number of COBRA phasing iterations. Convergence occurred around iteration 13; however, more iterations are shown to illustrate that there are no further changes in the error parameters. After iteration 13, no further changes were also observed in the electron density maps.

consists of atomic (Gaussian-like) peaks which can be easily modeled. The profiles obtained for the quantum dots revealed a complicated folded structure which could not be easily refined by fitting.

An alternate approach to refining the COBRA results was to use the iterated projection difference map method[40] with the initial COBRA-derived electron density as the starting point without the constraint of atomicity. The sum of square errors were reduced by about 40% when IPDM analysis was applied, indicating a better fit to the measured data than when COBRA was used alone.

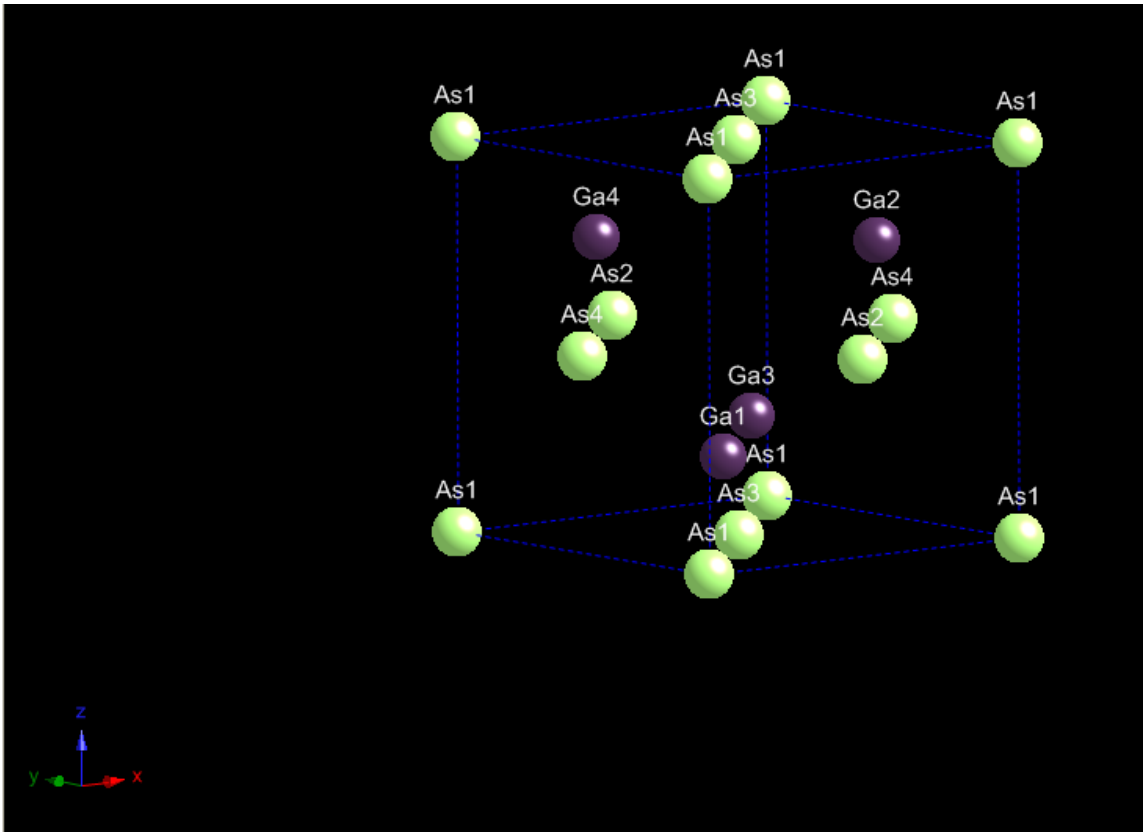

Figure 5.4: Schematic of GaAs unit cell. The lines represented in Fig.5.5 pass vertically through the corresponding atoms in the unit cell. The As-1 line passes through the As1 atom and so on. Atoms with the same labels are symmetry related.

5.3 Results and Discussion

Determination of Composition Profile

A comparison of ED profiles taken in the vertical direction along symmetry-inequivalent lattice sites for the two probe wavelengths is shown in Fig. 5.5. The As-1 and As-2 lines pass through the inequivalent group V atomic sites while the Ga-1 and Ga-2 lines pass through the group III sites. Expressed in GaAs unit cell coordinates, the As-1 line is along the coordinate directions [0,0, z], As-2 is along [0.5,0.0, z], Ga-1 is along [0.25,0.25, z] and Ga-2 is along [0.75,0.25, z][1].

The line profiles show two distinct regions of the system. The large narrow peaks

[1]In these directions, the spacing between the peaks is equivalent to one unit cell

below 65 Å correspond to the substrate atoms. The smaller broader peaks above 65 Å correspond to the dot region. The dot peak heights are smaller because the dots occupy only a fraction of the surface. The dot peaks extend to a height of about 50 Å (9 unit cells) in good agreement with the AFM results.

The two energies are compared for each line to illustrate the effect of the anomalous response of the atomic scattering factors (ASF). The ASF of As is 31 electrons at the x-ray energy 10.362 keV and 21.99 electrons at 11.862 keV, thus the As-like peaks would be expected to be higher close to the Ga edge than when the x-ray energy is close to the As edge. The ASF of Ga is 19 electrons at 10.362 keV and 30 electrons at 11.862 keV; thus the reverse would be expected for peaks containing mostly Ga. In has the same ASF(49 electrons) at both energies, thus peaks corresponding to mostly In would have peaks of approximate equal heights.

The As lines shown in Fig. 5.5 are higher at the As edge both within the substrate regions and the dot regions as expected. The ratio of the As peak heights at the two energies is equivalent to the ratio of the As atomic scattering factors at the two energies.

The line profiles through the G-III sites (Ga-line1 and Ga-line2) shown in the lower two panels of Fig. 5.5 show a different and more interesting behavior. Deep in the substrate region, the ratio of the peaks at the two energies indicate pure Ga. At the dot-substrate interface where the peak intensities start to fall off, a clear change in the ratio of the peak heights is observed indicative of an In-Ga alloy in the bottom 3 unit cells of the dot. Counting from the left, the 8th peaks in the two profiles along the G-III lines are determined to have average compositions of roughly $In_{0.50}Ga_{0.50}As$. These two MLs may be considered to constitute the wetting layer (WL).

The dot peaks begin immediately after the WL peaks. Due to the low intensity of the dot peaks and their non-Gaussian shapes, a determination of their composition from integrating their intensities is difficult and not reliable. We can however infer, qualitatively, from observing the profiles, what the expected composition distribution is. The relative intensity of the preceding 3 peaks after the WL peaks in both G-III profiles have ratios at the two energies consistent with an In-Ga alloy with the In content increasing away from the dot-substrate interface. In the topmost 5-6 unit cells in the dot region, the G-III peaks have approximately equal intensities at the two energies, indicating that they are mostly In.

Analysis of peak widths

The atomic root mean square displacement (MSD) contains information about the thermal Debye-Waller factor, the amount of disorder in the system and also the deviation from the substrate periodicity (since the ED is the folded structure). The MSD is determined from the full width at half maximum, $FWHM$, of the atomic peaks.

$$MSD = \sqrt{FWHM^2 - (\frac{DW_{art}}{a})^2} \tag{5.1}$$

where a is the substrate lattice constant and DW_{art} is an artificial Debye-Waller term introduced during the COBRA analysis to suppress high frequency noise. The peak FWHM is determined by fitting the peaks to a three-dimensional Gaussian function.

The in-plane (x and y) and out-of-plane (z) MSDs as a function of ML are compared in Fig. 5.6. In the substrate region, the peaks are strongly localized with MSDs of less than 0.3 Å. The in-plane MSDs in the dot region increase slightly compared to those deep in the substrate peaks with the largest increase in the top 5 UCs of the dot. Coincidentally, we observe more In in Fig.5.5 in this same region suggesting

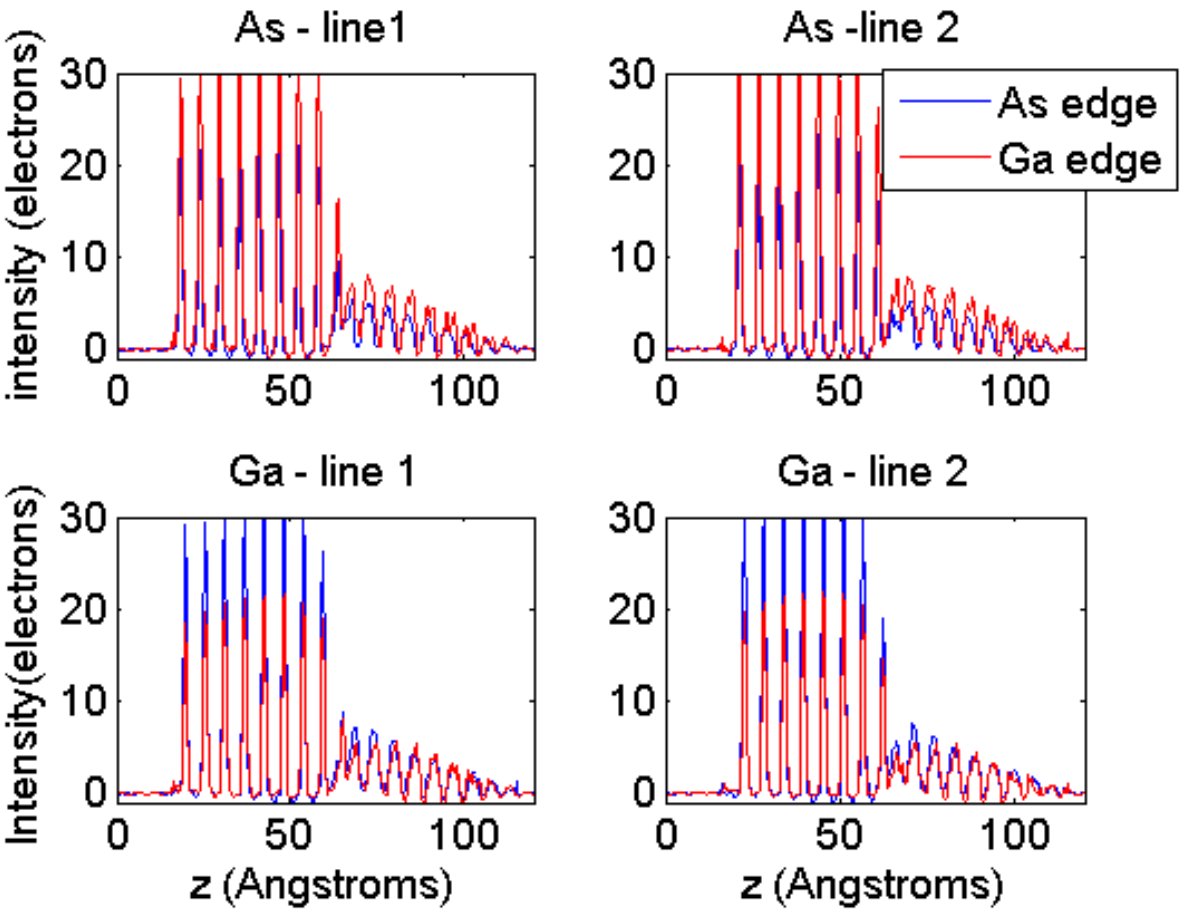

Figure 5.5: Comparison of line profiles along symmetry inequivalent lines in the GaAs unit cell from ED maps obtained from measurements at 10.362 keV (5 eV below Ga edge) and 11.862 keV (5 eV below As edge)

that the top parts of the dots have the most in-plane strain relaxation.

At the dot-substrate interface, there is a jump in the MSD in the vertical direction to about 1.2 Å. This value remains more or less constant in the dot region to about an average value of 1.1 Å and then falls to about 0.8 Å at the top of the dots indicating more inplane relaxation in these regions. This observation is consistent with curved crystal planes bowing upward with the base-to-top length being on the order of 0.5-1 Å (If this is true, it should be seen in an XSTM, unless the relaxation of strain in the thinned sample changes the shape). Since the rods were only measured up to 4.5 GaAs reciprocal lattice units due to experimental constraints, we are limited in resolution of about 0.6 Å. This effective resolution is less than the curvature of the planes, thus, we observe a single broadened peak for each layer.

Interestingly, although the crystal planes seem to be curved, there is still excellent registry between the in-plane positions of the atoms in the dots with the substrate as is evidenced by the relatively small change in the dot in-plane MSDs. The curvature of the planes serves a way to increase the inplane dot-to-dot spacing

The difference between the GaAs unit cell size and InAs is about 0.4 Å so it is plausible to conclude that the dots have a highly strained In enriched core with the dots becoming more GaAs-like as one moves out radially to the periphery of the dots. The top parts of the dots have a larger fraction of surface area to relax strain outward, hence they are able to accommodate more In than the lower sections of the dots.

Analysis of peak spacings

The distance between the peaks in the ED profiles in Fig. 5.5 provides information about the stacking of the atomic planes in the vertical direction. The spacings of

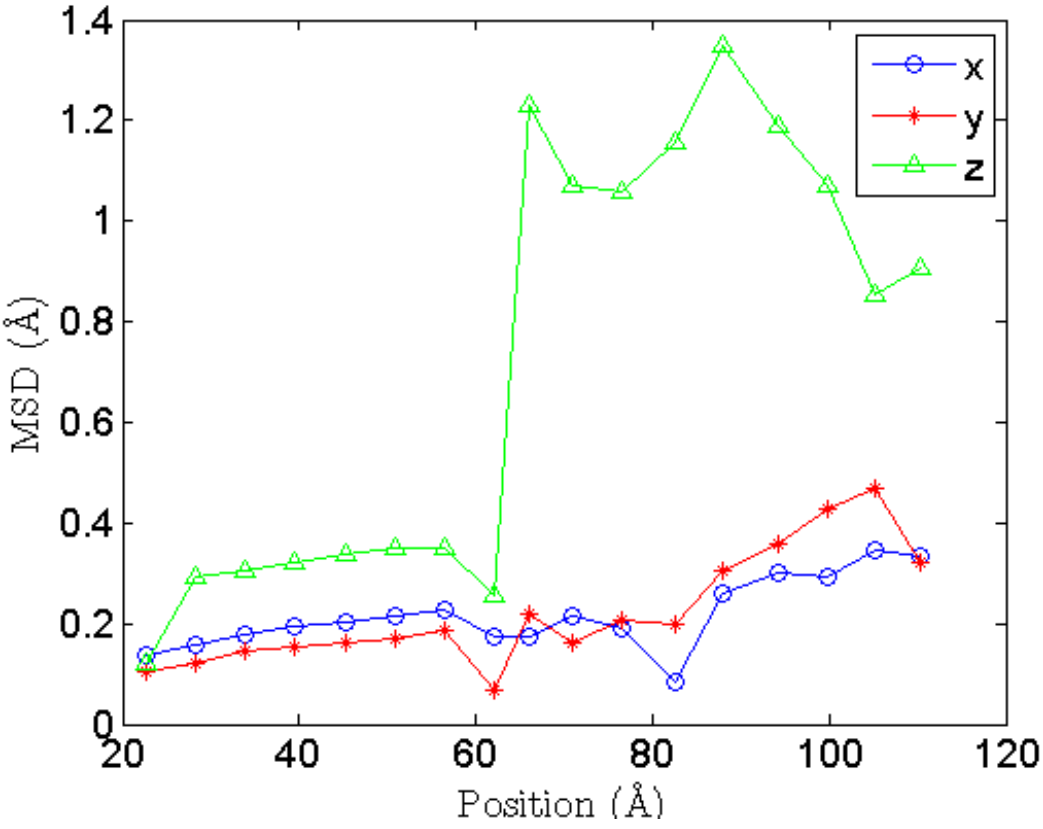

Figure 5.6: Root mean square displacement of the electron density peaks of the folded structure

the peaks in the 4 inequivalent lines are compared in Fig. 5.7. The spacings along the substrate region are 5.65 Å, as expected for GaAs. At the interface, there is a decrease in the spacings to about 4.5 Å for one G-III line and 3.5 Å for the other lines. The spacings then recover to, approximately, the GaAs lattice parameter in the dot region.

The dip in the lattice spacing at the interface and the GaAs-like lattice spacing in the dot region are unexpected. The contraction at the interface may be due to an atomic reconstruction which arises to accommodate the curved crystal planes in the quantum dots although the details of this mechanism are not immediately clear from the COBRA results.

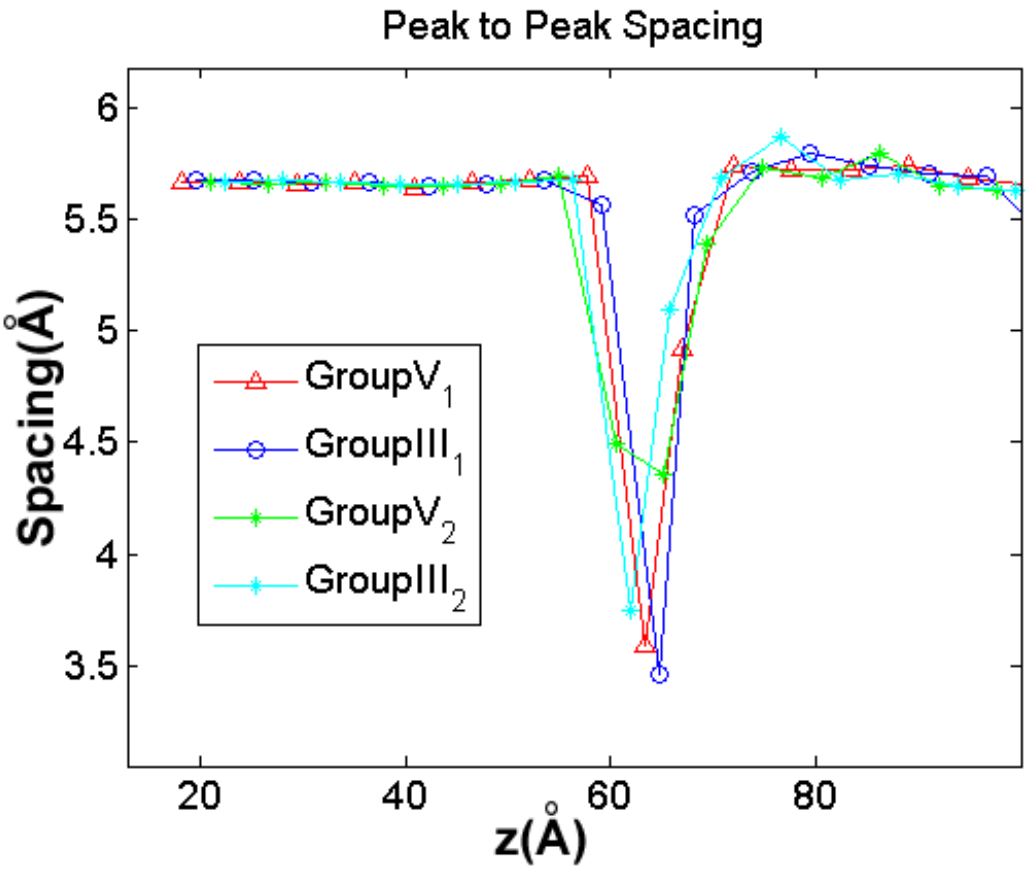

Figure 5.7: Comparison of out-of-plane atomic spacings along symmetry inequivalent lines in the GaAs unit cell from ED maps. The G-III lines are along lattice sites corresponding to In and Ga and the G-V lines are along lattice sites corresponding to As. The atomic spacing in the dot regions are on average about 5.71 Å compared to 5.65 Å in the substrate. Note the decrease in the spacings at the interface (between 60-70 Å)

A model of the stacking order at the interface based on the layer spacings is shown in Fig. 5.8. From this model, it is clearly seen that, in addition to the observed contraction at the dot-substrate interface, there is a layer in which the group III and group V sub-lattices overlap. Again, It is not directly clear if this overlap is due to laterally separated regions .

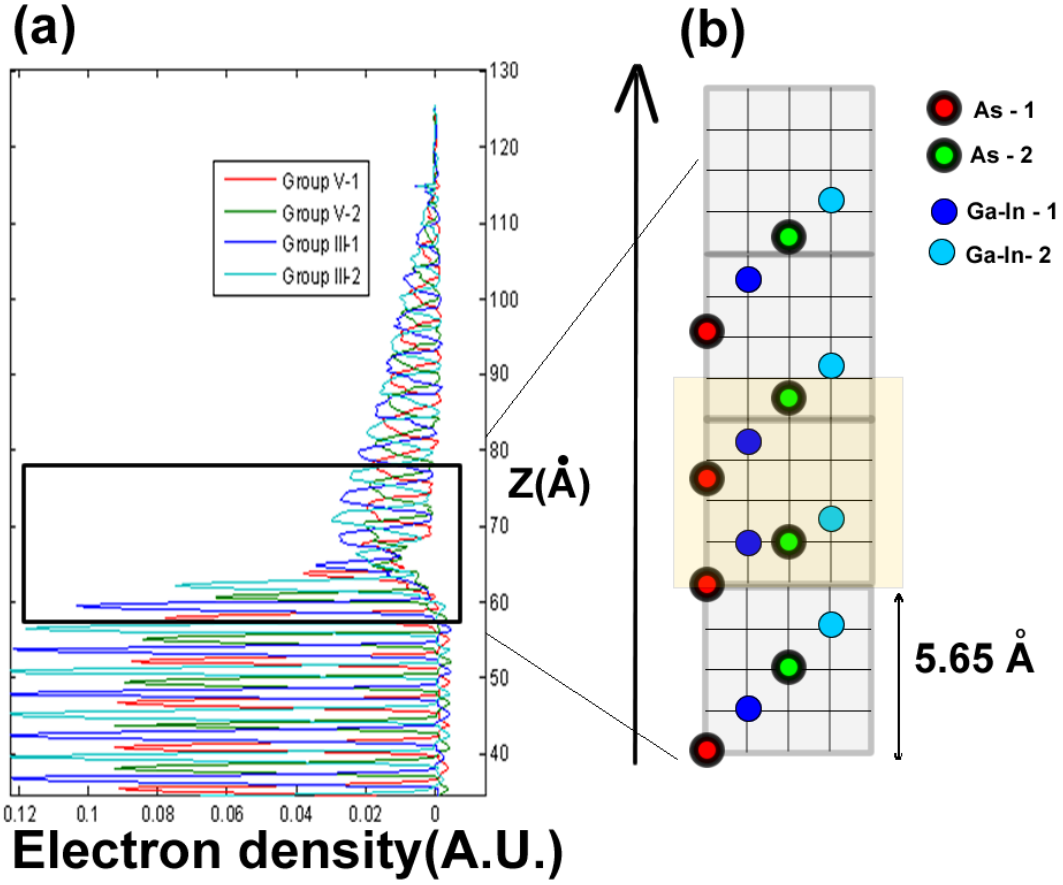

Figure 5.8: A model of the stacking order at the dot-substrate interface region (indicated by the square box) in ED intensities profiles in (a) is shown in (b). At the dot-substrate interface, a contraction of the unit cell is observed in addition to a change in the stacking sequence of the GIII-GV sublattices. The correct stacking sequence is recovered in the quantum dot.

Determination of Dot Shape

The ED profiles give the total areal coverage per layer. To determine the individual dot widths, the square root of the coverage and the dot-density obtained from

AFM are required. For a given dot density, ρ (in units of number of dots per cm^2) and an areal coverage $\theta(z)$ at height z, the width of an individual dot, $w(z)$ (in cm) at that height can be calculated from the equation:

$$w(z) = \sqrt{\frac{\theta(z)}{\rho}} \tag{5.2}$$

A schematic of the dot shape inferred from this analysis is shown in Fig. 5.9.

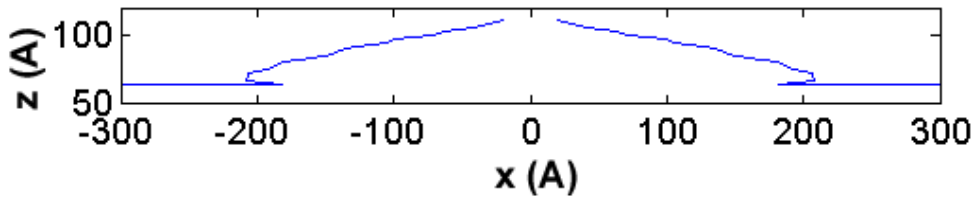

Figure 5.9: A schematic of individual dot shape drawn to scale as determined by COBRA. The diameter is 45 nm and height is 5 nm.

5.4 Conclusions

The anomalous-COBRA method has been applied successfully to study high density uncapped coherent InAs quantum dots grown on a GaAs substrate. An analysis of ED maps obtained close the Ga and As K-edges has revealed directly, the vertical composition profiles of the constituent elements in the dots, the dot-substrate interface and the top 12 MLs of the substrate.

The results obtained indicate that the dots are in coherent registry with the substrate since the folded structure obtained gives electron densities in the dots which are correlated with the lattice sites in the substrate.

The dots are observed to have an In rich core and an In-enriched top surface in agreement with previously published x-ray isostrain measurements[17] and cross-sectional STM measurements[54]. A $In_{0.50}Ga_{0.50}As$ wetting layer was observed at the

dot-substrate interface. The average In composition as a function of distance from the interface was found to increase from about 50% at the dot-substrate interface to about 100% at the top of the dots.

A change in the stacking sequence is observed at the dot-substrate interface . This shift, which has not been directly observed before, appears to play a critical role in relaxing interfacial strain in this system. This shift is also observed in InSb/GaAs dots grown by the DHE method[82].

We can rule out the possibility that this shift is due to interfacial dislocations since atomic registry is maintained in the dots. Cross-section TEM results samples grown under similar conditions show these systems to be free of dislocations.

The possibility then remains that an interfacial reconstruction coupled with a bending of the crystal planes in the dots occurs to relieve strain. Whether this reconstruction occurs before or after the dot formation cannot be discerned from our results. Carrying out the diffraction experiments in-situ to study the different stages of growth would provide more insight into this process.

Studying ensembles of the dots also presents an intrinsic limitation on the interpretation of the obtained results. While it is shown that we can obtain reliable information about the average composition as a function of height, it cannot be directly discerned if the averages are over non-uniformities within the dots or between inhomogeneous dots. However, the trends we observe in the in-plane widths of the dots suggests that there is excellent dot-to-dot homogeneity in the samples studied. This technique has provided valuable information inaccessible by other established characterization techniques.

The observed curvature may be resolved in finer detail if further measurements are performed to include a higher range in the $\vec{q}_z$ direction. For the wavelengths

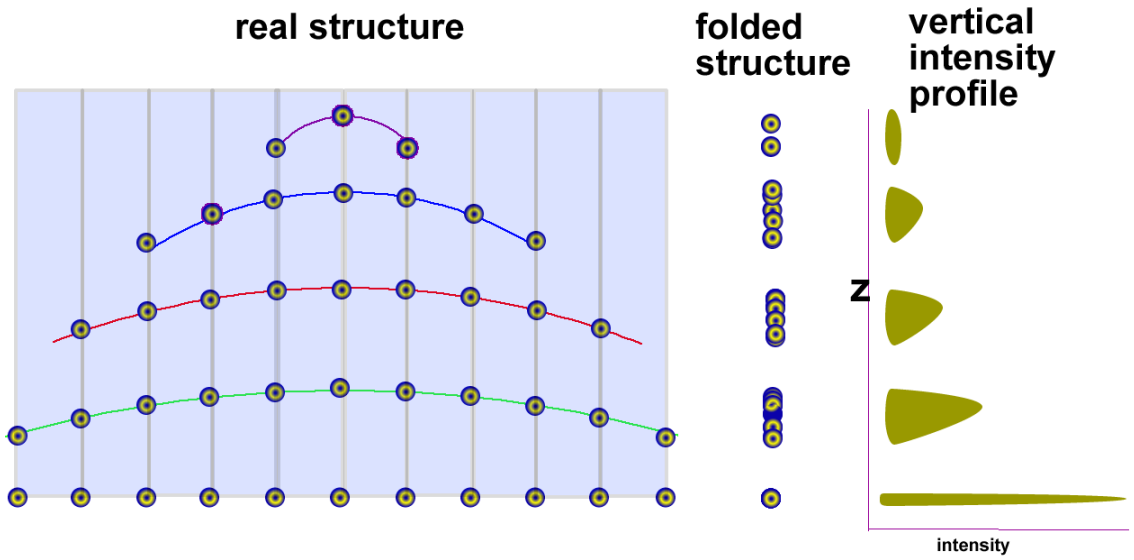

Figure 5.10: Schematic of folded structure of curved atomic planes in the quantum dots. In the center of the dots where the In segregates, the lattice spacing in the vertical direction is expanded relative to the edges of the island where there is more Ga. The overlap of the atoms due to the curved planes in the folded structure produces peaks broadened in the vertical direction. There is significantly less broadening in the horizontal direction because the atoms in the dots are in vertical registry with the atoms in the GaAs substrate.

used, we were restricted by geometrical constraints on the diffractometer setup. Evidence for long range corrugation of crystal planes has been observed in vertically ordered multilayers of InAs QDs from STM studies with the degree of undulation intensifying with increasing layers[83, 84]. This undulation is concluded to arise from the curvature of the crystal planes within the individual dots. At the present time, it remains unclear why the observed out-of-plane lattice spacing in the dots is more GaAs-like than InAs-like.

Theoretical calculations to determine the electronic properties of the COBRA-determined structure of the InAs quantum dots are left for future studies.

CHAPTER VI

Results and Discussion - Droplet Heteroepitaxy InSb dots on GaAs

6.1 Introduction

The Droplet Heteroepitaxy(DHE) technique has emerged as a viable alternate method to grow epitaxial quantum dots [85, 59, 86]. The DHE technique does not require mismatch strain and is therefore potentially more relaxed in the combination of materials that can be used to form QDs.

At present, little is known about the atomistic mechanism of QD formation especially those formed by DHE[58]. In particular, one would like to know what are the detailed structural and compositional characteristics of this process as a first step towards the controlled growth of DHE QDs. The answers to this question also have relevance to the growth of quantum wires, which grow catalytically underneath a metal nano-cap (e.g., Au)[87].

Results are presented in this chapter on the application of the anomalous-COBRA method to study a III-V DHE system, In/GaAs exposed to Sb, which illuminates essential details of the dot formation mechanism revealing a complex interplay of thermodynamic and kinetic processes, resulting in a high density of relatively uniform QDs. For the system under consideration, it is found that droplet QDs are formed epitaxially, i.e., the dot structure is in atomic registry with the substrate,

and that a substrate-dot exchange of group III species takes place. This occurs without the presence of a wetting layer, in the conventional sense of the continuous, pseudomorphic few-monolayer substrate coverage that precedes QD formation in their S-K counterparts[88]. The oblate, rounded shape of the QDs we observe, exhibiting obtuse contact angles, is a striking feature of this particular DHE system. Clearly the dot-substrate interface is of key importance in this case, and one of the most intriguing findings reported here relates to the symbiotic nature of the structure immediately underneath the dots. Our work provides the first atomic-scale mapping.

6.2 Experimental Details

6.2.1 Sample Preparation

The DHE system chosen for this study consists of In droplets deposited on a GaAs (100) substrate and subsequently exposed to Sb vapor to form QDs with a nominal composition of InSb. Two samples, prepared under similar deposition conditions but with different dot sizes, were measured in order to verify the reliability of the results.

The deposition was carried out in a Metallorganic Vapor Phase Epitaxy reactor,[59]. The growth involved epitaxially-ready GaAs substrate heated to 390^{o}C followed by an As pre-growth treatment using tertiarybutylarsine (TBA) in order to prevent substrate thermal etching. In the first sample, liquid In droplets were formed while supplying 2 secs of 150cc TMIn (trimethylindium) at a rotation speed of 200 rpm. In the second sample, to give smaller droplets, the rotation speed was increased to 300 rpm; all other conditions were the same. After cooling the substrate down to 350^o C, keeping the rotation speed constant, the droplets were exposed to 45 cc TMSb (trimethylantimony) for 15 sec, forming the final structure. The method is very sensitive to the growth parameters and gives great flexibility in realizing high density

QD growth on different lattice-matched and mismatched substrates.

Fig.6.1(a) shows an Atom Force Microscopy (AFM) image of the larger dots (sample 1). In both samples, the QD density measured by AFM is higher than 10^{10} cm^{-2}. The rounded shape of the dots has been imaged using high resolution scanning electron microscopy (SEM) in a glancing geometry [Fig. 6.1(b)] on a sample in which the substrate was pre-treated with Sb to give larger dots and a less dense coverage. Such measurements could not be performed on the actual samples we studied because of the very high dot density that leads to image occlusion. In addition, it is difficult to quantify the QD geometry in this way, even with the highest resolution SEM currently available. More challenging is the fact that the dots have a substructure extending a few atomic layers beneath the substrate surface. COBRA overcomes both of these difficulties.

6.2.2 X-ray Diffraction Experiments

Measurements of the QD structures were performed in Bragg rod geometry at the Advanced Photon Source on an undulator beamline (XOR/UNI 33-ID), which provides a highly intense, tunable beam of x-rays. The beam was focused to a spot size of 200 μm x 300 μm. Diffraction intensities were recorded along substrate-defined Bragg rods using a Pilatus 100K 2D pixel detector mounted 1m away from the sample. This pixel detector has essentially no electronic noise. Background due to air scattering and diffuse scattering from the sample were later removed at each point. Polarization and Lorenz corrections were applied to the extracted intensities. For each sample and at each energy, nine inequivalent rods were measured over a range from 0.5 to 4.5 GaAs reciprocal lattice units.

Data were obtained at two different x-ray energies corresponding to the absorption

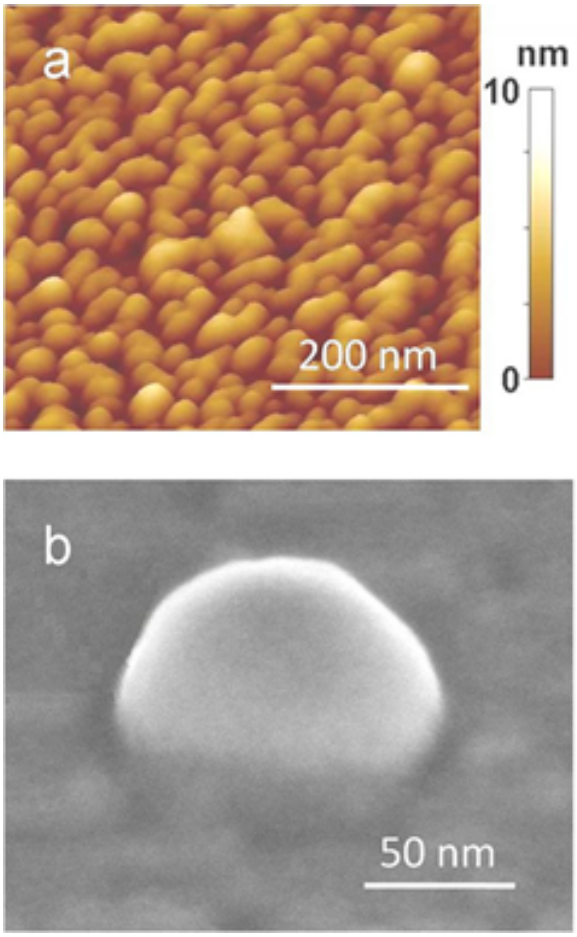

Figure 6.1: In-droplet-grown nanostructures formed on a GaAs (100) substrate: a) AFM image of sample 1. The variance in dot height over the scan area shown is $\sim$ 0.5 nm; b) high resolution SEM image of droplet QD morphology.

edges of Ga and As. These resonant conditions considerably enhanced the chemical contrast between two species (Ga and As) which would otherwise have very similar scattering cross-sections.

6.2.3 Anomalous-COBRA analysis

The analysis of the Bragg rod data was accomplished using COBRA as explained in the previous chapters. The first step in a COBRA structure determination is to choose a reference structure that defines an initial known ED. Since the dots cover only a fraction of the area, it was reasonable to assume a reference structure

that consists of the GaAs substrate and an InSb film with exponentially decreasing coverage towards the top surface. As seen below, the actual ED obtained is much more complex and interesting. This is the advantage of using a direct method. The final results converge to the correct solution even though the initial reference structure is incorrect.

The iterative projection difference map method was used to refine the COBRA results at each energy without the atomicity constraint because, as seen from the results below, the folded structure cannot be described as composed of discrete atoms. Starting from this COBRA-phased structure, the difference map algorithm converged quickly, in about 20 iterations, to the exact solution yielding excellent agreement with the experimentally measured Bragg-rod intensity profiles.

6.3 Results and Discussion

The tunability of the synchrotron source x-ray energy was exploited to enhance the scattering contrast of Ga and As and to determine the relative concentrations of all four constituents of this quaternary system. The first sample, with the larger dots, was measured using x-ray photons of energy E^1 = 10.362 keV (5 eV below the Ga K-edge). At this energy the scattering cross sections of Ga and As are f^1_{Ga} =19.44 andf^1_{As} = 31.28 electrons, respectively. The second sample was measured at both E^1 and at a second energy, E^2 = 11.862 keV (5 eV below the As K-edge). At E^2, the Ga and As cross-sections are $f^2_{Ga} = 29.96$ and $f^2_{As} = 21.24$ electrons, respectively. These energies were selected to maximize the difference between the scattering factors of Ga and As.

The determination of the composition was performed as described in the preceding chapters for each monolayer slice of the ED map as a function of distance from the

interface.

The ED of the first sample, along 4 inequivalent lines perpendicular to the surface, each going through one of the atoms of the GaAs substrate unit cell, is shown in Fig. 6.2. Several features can be clearly seen: first, the ED is positive definite; second, the large peaks towards the left correspond to atoms in the substrate. The calculation was limited to 7 substrate unit cells below the interface; beyond this depth the ED is bulk-like. The ED towards the right, with a Gaussian-like profile centered on 20 Å, corresponds to the dot structure. Note that the ED associated with the dots reaches a maximum to the right of the interface and then decays to zero in a way consistent with the dot height distribution [Fig. 6.1(a)]. This ED profile is a direct signature of the non-wetting geometry of the dots.

The ED peaks corresponding to the Ga atoms in Fig. 6.2 are smaller than those of the As both in the substrate and in the dots. We expect this in the substrate because, at the x-ray energy used, the Ga cross-section is significantly smaller than that of As. Since the scattering cross sections of In and Sb are almost equal, the difference in peak heights also seen in the dots means that they are not simply composed of In and Sb: there must be a significant concentration of GaAs in the dots.

In the inset of Fig. 6.2, we show an enlarged display of the ED along the line going through Ga1. Two sets of peaks are evident. The first set, (shaded) are associated with the substrate; they are narrow and follow the sequence of the substrate peaks, decreasing towards the sample surface (on the right). The second set, corresponding to the dots, are split and decrease going into the substrate and towards the sample surface. These two sets of overlapping peaks show very clearly that the lower part of the dots penetrate a small distance (2nm) into the substrate. This is consistent with earlier observations on In and Ga[89] droplets nanodrilling into GaAs substrates. The

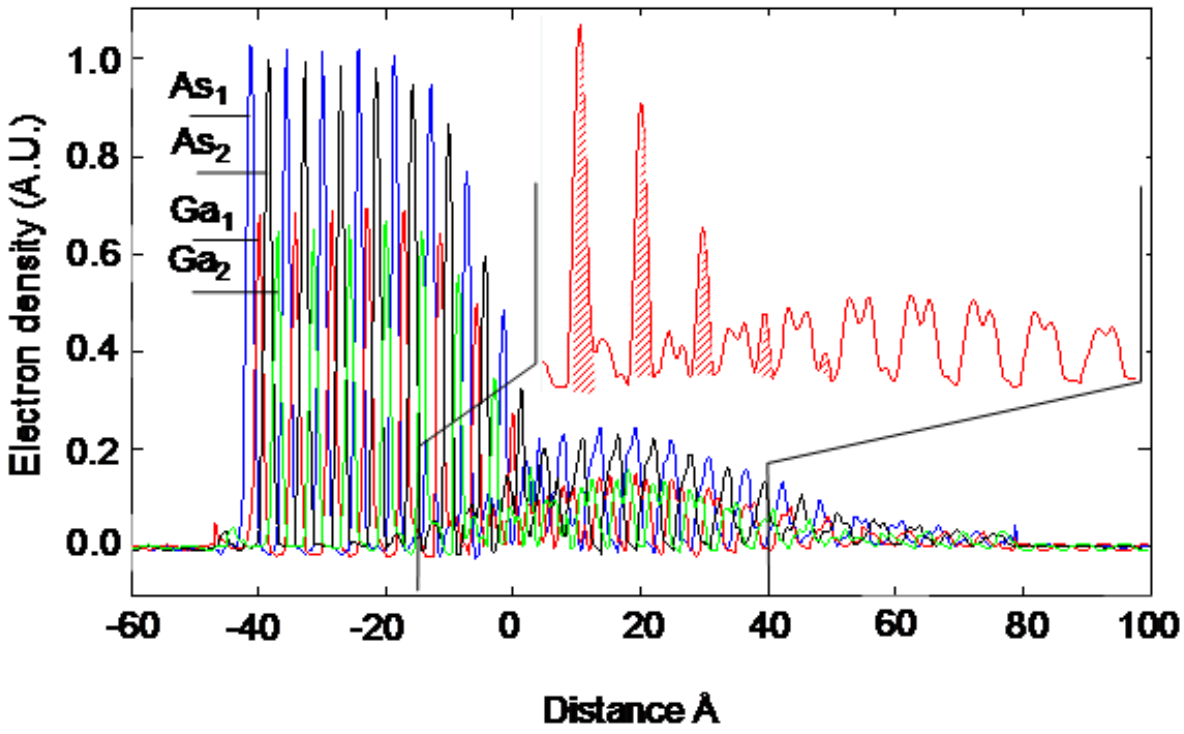

Figure 6.2: [001] ED profile of sample 1 through all four inequivalent atomic rows of the GaAs substrate unit cell as a function of distance from the interface. Inset: ED profile through Ga1. Substrate like peaks are shaded.

same main features were observed in the second sample (see Fig. 6.3), indicating that the results are repeatable and reliable.

We have compared the ED profiles of the second sample along lines of G-III [Fig. 6.3(a)] andG-V [Fig. 6.3(b)] atoms in the (110) plane, measured at the Ga and As K-edges. In this way we are able to determine the distribution of chemical species as a function of distance from the nominal interface. Note that the sizes of all substrate G-V peaks measured at the As edge are smaller than those measured at the Ga edge, and the ratio is about equal to the ratio of the scattering cross sections. On the other hand, in the dot region above the first two unit cells, the sizes of the left component of the peak pairs [Fig. 6.3(b)] are about equal for the two energies, indicating that this

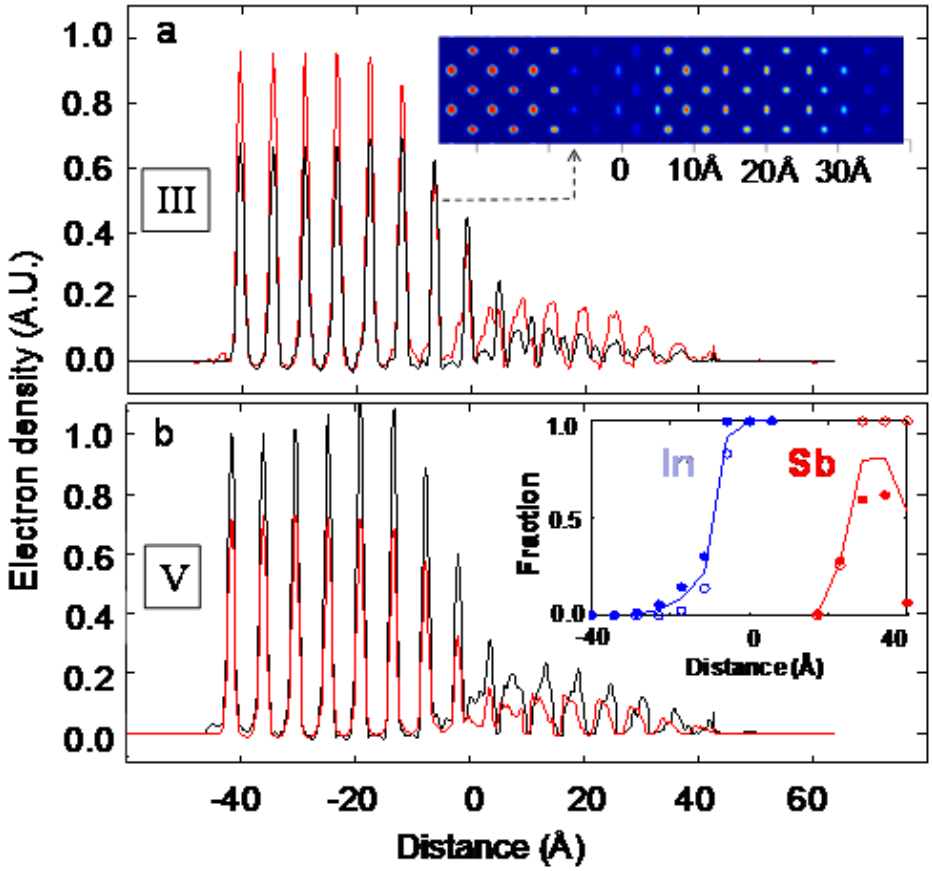

Figure 6.3: [001] ED profile of sample 2 through (a) Ga1 and (b) As1 determined using the Ga edge (black line) and the As edge (red line) x-ray photon energies. Inset (a): (110) map of the differential electron density for Group III species, measured at these two energies. Inset (b): In occupancy fraction in sample 2 in the substrate (blue), and of Sb in the left Gaussian components of the dot peaks (red). The open and solid blue dots for each cell represent the values obtained from the Ga1 and Ga2 lines, while the red dots were obtained from the As1 and As2 lines The solid lines are the averages.

component has a large Sb content. The ED along the Ga1 line (group III) is shown in Fig. 6.3(a). Here, for the two unit cells below the nominal interface, the sizes of the substrate-like peaks measured by both energies are equal within the experimental accuracy. This means there is a significant concentration of In at the substrate-dot interface. This is vividly highlighted in the differential electron density map shown in the inset of Fig 6.3(a), where the interface (arrowed) shows up as a region of low Ga concentration. In contrast, the magnitude of the dot-like peaks measured at the

two energies are all different, showing there is actually very little Indium in the dots themselves.

The EDs along the As2 and Ga2 lines are also analyzed in a similar way;. Symmetry does not require these EDs to be equal to the EDs along the As1 and Ga1 lines. Indeed the EDs are slightly different, but the features described above are clearly the same. The unit-cell-by-unit-cell In and Sb concentrations are shown in the inset of Fig. 6.3(b). These values are based on a quantitative analysis of the 3D integration of the EDs. That only a little In is present in the dot is quite unexpected. This is in contrast to the results on the S-K InAs/GaAs system in the previous chapter where In is found in the dots.

In the dots, both group III and group V peaks are split. The peak positions are determined by fitting one Gaussian to each peak in the substrate and two Gaussians to each peak in the dot. The substrate is used as a frame of reference to determine the vertical displacement of each Gaussian relative to the position of the corresponding atom in the reference GaAs unit cell as a function of the distance of the atom from the nominal interface. It is found that the Gaussians of each peak in the dot sequence deviate by about one-quarter and one-half of a unit cell relative to the reference, respectively. We therefore associate these displacements with a change in the stacking sequence going from the substrate into the dot. It is not yet known the details of this stacking shift (see Fig. 6.3); it could be due to a double group III layer at the dot-substrate interface, or possibly an interface reconstruction[90]. Interestingly, since this stacking shift allows us to distinguish the atomic structure of the dots from that of the substrate, we can tell that the high concentration of InAs noted in Fig.6.3(a), is associated with the top 2 unit cells of the substrate and not with the dots per se.

That the dot peaks are split (Fig. 2, inset) suggests that there are either two types of dots or each dot has two distinct regions. Kelvin probe measurements[58] on a similar dot system show no evidence of two types of dots, which implies that there are two different compositional regions in each dot. Within experimental uncertainty, the substrate does not contain any Sb; the left components of the dot peaks (Fig. 6.2, inset) do not contain any In, and the right components of the dot peaks contain only Ga and As.

We cannot tell for sure which part of the dots corresponds to the left or right components of the ED peak pairs. However, it is plausible that the Sb is mainly on the outside and top part of the dots, because it is these regions that come into direct contact with the Sb vapor and the Sb, being relatively large, tends to go to the surface. This is consistent with the well-known role of Sb as a surfactant layer[91]. Photoluminescence measurements performed on the same uncapped dots show clear peaks fitting to the GaSb band gap in agreement with the suggested picture[59].

The ED maps on planes parallel to the interface provide important information on lateral strain relaxation. For example, if the size of the unit cell on a given plane is different from that of the substrate, the folded-structure ED peaks in that plane will be broader than those of the substrate. After removing the instrumental broadening, the in-plane ED associated with a given atom as a function of position [see Fig. 6.4(a)] measured from the center of the corresponding atom in the substrate, is proportional to the probability that the atom is laterally displaced by relative to the corresponding substrate atom.

The average difference between the cell sizes Δa in a given plane and in a plane deep in the substrate is thus approximately equal to:

$$\Delta a \approx \frac{2w}{N} \tag{6.1}$$

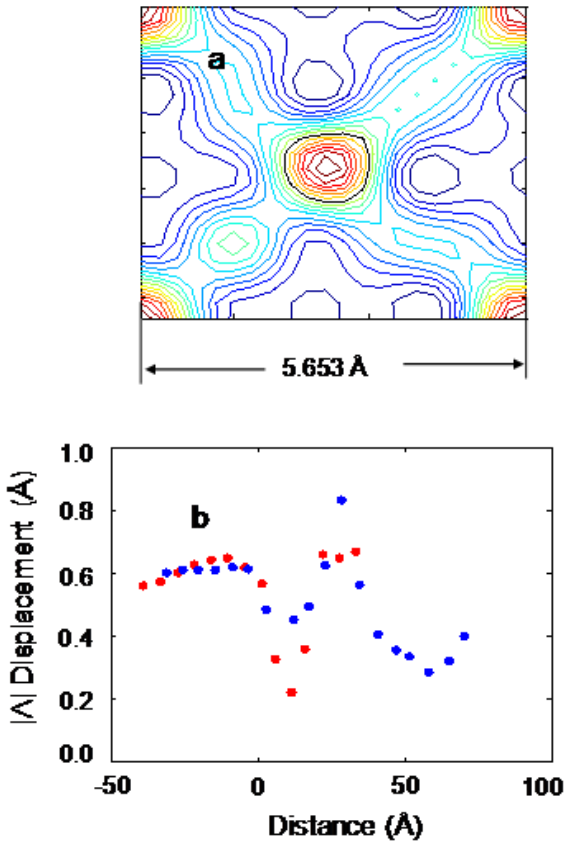

Figure 6.4: (a)ED map over one lateral unit cell on a plane perpendicular to [001] 13 Å away from the interface. The black contour is at half the center peak height; (b) the lateral displacement of atoms at distribution half maximum relative to the corresponding atoms deep in the substrate as a function of distance from the interface. Sample 1-blue; sample 2-red.

Where w is the full width at half maximum (FWHM) of the ED peak and N is the average width of the dot measured in unit cells. Dislocations have been shown to decrease the displacements of atoms in the dots relative to the corresponding atoms in the substrate[92]. The unit cell size difference in the presence of dislocations is:

$$\Delta a \approx \frac{2w}{N_d} \tag{6.2}$$

where N_d is the average number of unit cells between two edge dislocations, or a dislocation and the dot edge.

An example of the in-plane ED on a plane 3 unit cells above the nominal interface is shown in Fig. 6.4(a). At the center we see an As atom. The black contour is at the half maximum level. Thus the average diameter of this contour is the measured FWHM of this peak. The instrumental FWHM is ∼1.1 Å, resulting mainly from the limited range of measured diffraction in reciprocal space. The lateral displacements of the atoms, relative to the corresponding atoms in the substrate at half maximum of the distribution, are equal to half the peak width at half maximum. After removing the instrumental contribution, the displacements are shown for both samples in Fig. 6.4(b) as a function of the distance from the interface. First, note that both samples behave in a qualitatively similar way. In the topmost substrate unit cells (mostly InAs) these displacements are about 0.65 Å. Since the dot spacing is ∼200 Å, the average increase of the unit cell in the substrate region between the dots is about $\Delta a = 2 \cdot 2 \cdot 0.65/(200/5.65) = 0.074$ Å. This value is much smaller than the nominal difference between InAs ($a_0 = 6.06$ Å) and GaAs ($a_0 = 5.65$ Å) unit cells, implying that the topmost substrate layer is under strong compressive stress.

The oscillatory behavior of the displacements shown in Fig. 6.4(b) is interesting and most likely is related to the rounded, non-wetting geometry of the QDs. Namely, the minimum corresponds to a narrow waist at the base of the dot while the peak corresponds to the maximum diameter about 3 nm above the base. Note that dislocations could also affect the in-plane lattice spacing close to the dot-substrate interface[58]. An overall plausible, but perhaps simplistic, picture consistent with the observed results is as follows: Indium attacks the top GaAs substrate layers replacing Ga in the substrate. At the growth temperature, As has a significant vapor pressure. The released Ga interacts with the As, forming the dots cores. The remaining Ga interacts with the Sb vapor, forming the dots outer shells. The quarter and half

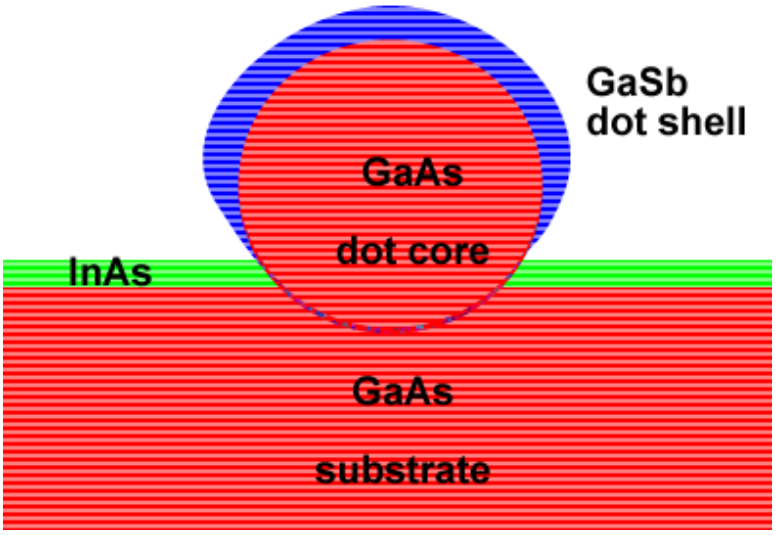

Figure 6.5: Schematic of dot structure (not drawn to scale). The dots have two regions: a GaAs core and a GaSb outer shell. The base of the dot subtends below the GaAs substrate surface. Indium replaces the Ga in the top surface of the substrate forming an InAs on the surface.

unit cell displacements can be thought of as stacking faults which serve to relieve the strain.

6.4 Conclusions

While the interaction of group III droplets with III-V substrates is relatively well studied[89, 90], our measurements reveal new atomic-scale details of the mechanism of III-V dot formation in DHE resulting from the crystallization process following exposure of GaAs-supported In droplets to Sb. In particular, COBRA is able to directly probe the substructure of the dots where they penetrate into the substrate. In the present system, we observe a complex process in which atomic species are exchanged between the substrate and the droplet. This results in droplet QDs that have a shell-like structure (GaSb) and a core (GaAs) which is more an extension of the substrate than the intended InSb composition. For small enough dots, there is very little Indium in the resulting QD, even though the deposition started with

In droplets. We also find a high degree of lattice coherence between the QD and the substrate. These findings together suggest that the mechanism of droplet QD formation in the system studied is an interplay between kinetic (interdiffusion) and thermodynamic (surface energy) processes.

The generality of these findings can be explored in the context of other QD systems. For example, the ability to quantify structural and chemical distributions in QD systems at the atomic level can help resolve long-standing puzzles relating to the inverted electron-hole alignment[93] observed in some III-V QD systems.

The power of COBRA for detailed mapping of chemical, strain and structural aspects of a broad range of epitaxial QD systems provides a new capability that should have a significant impact on nanotechnology as QD systems continue to be refined and controlled for many applications.

CHAPTER VII

Conclusions and Future Directions

The application of the anomalous-COBRA technique to solving the structure of alloyed island epitaxial systems has been successfully demonstrated for the first time, revealing new and exciting details which would be of interest to device engineers, theorists and material growers.

This is the first study of its kind and its importance lies in the general applicability of the COBRA phasing method for epitaxial heterostructures. This class of materials is at the heart of most modern electronic devices such as high electron mobility transistors (HEMTs), quantum dot lasers, and new designs for high efficiency photovoltaic solar cells.

The main advantage of the anomalous-COBRA technique is that it provides an unambiguous and direct non-invasive way of obtaining quantitative information about the sub-surface composition and atomic structure of systems which are commensurate with an underlying substrate. The level of detail attainable using this method is not easily obtained using traditional microscopic techniques which may lack atomic resolution, lack chemical sensitivity, be restricted by surface morphology and cleavage planes or require complicated interpretation of data.

7.1 Summary of Results

On of the main achievements of this work is to extend the COBRA technique from epitaxial thin film structures into a new regime in which the relevant structures are not continuous films but consist of laterally separated islands or nanostructures. These structures are nevertheless still commensurate with the supporting substrate (i.e., the atoms in the nanostructure are in atomic registry with the those in the substrate. The work therefore makes contact with important new nanostructures in the form of quantum dots.

The island morphology of the GaAs/InGaAs/InP system as a function of growth temperature independently determined by a-COBRA is in excellent agreement with STM measurements on this system. In addition to the morphology, the a-COBRA method reveals detailed information about the distribution of strain and composition in this system with sub-atomic precision revealing how an interplay between island formation and atomic intermixing, lead to dislocation-free strain relaxation. The strain is found to increase continuously from the interface, where most of the strain is relieved due to In incorporation from an initially Indium-rich InGaAs buffer surface, to a maximum at the top of the film of 0.7%($T_{deposition}(GaAs)$=480^o C) and 1.0%($T_{deposition}(GaAs)$=520^o C).

The application of the a-COBRA method to InAs quantum dots grown by the Stranski-Krastanow method has revealed an intricate picture of the structure of the dots and the dot-substrate interface. The method provides a non-destructive way of obtaining information about the shape, size, composition and atomic structure of the system. It is found that the wetting layer and dots contain significant amounts of Ga with the Ga content in the dots decreasing from about 50% at the base of the

dots to 0% at the top of the dots. Evidence is also seen for a lateral composition gradient in the dots with the dots having In rich cores with the In content decreasing radially outward. From the intensity profiles, the average dot shape and size can also be directly determined. The dot width and height are determined to be 45 nm and 5 nm respectively, in good agreement with atomic force measurements on the sample. A change in the stacking order at the dot-substrate interface points towards a reconstruction to accommodate strain. This reconstruction has not been observed before and more work needs to be done to understand this observation in more detail. An analysis of the out-of-plane widths of the atomic peaks in the dot reveal that the planes in the dots are curved outward. This curvature is interpreted as further evidence for how strain is relaxed without the formation of dislocations in the dots.

In the study of the DHE InSb dots on GaAs, a complex process in which atomic species are exchanged between the substrate and the droplet is revealed. This results in droplet QDs that have a shell-like structure (GaSb) and a core (GaAs) which is more an extension of the substrate than the intended InSb composition. For small enough dots, there is very little Indium in the resulting QD, even though the deposition started with In droplets.

7.2 Limitations of the a-COBRA method

Unfolding the folded structure

The information provided by the folded structure is unprecedented. The interpretation of the folded structure is challenging, and several examples were presented in this work to illustrate the usefulness of the method. In particular, we have demonstrated that, in the case of lattice mismatched QDs, the broadening of the folded

electron density peaks in the plane of the substrate can give valuable information about the strain relaxation that QD's can experience to relieve lattice mismatch. This is a unique feature of transversely patterned nanostructures, and it offers the advantage that such relaxation processes can occur without the formation of misfit dislocations, which would other wise act as strong charge carrier scattering centers. In this way the nanostructured devices can retain the high electron mobility and low trapping density necessary for optimal device operation.

However, the difficulty in 'unfolding' the COBRA electron density to determine the real properties of the system may be reduced if superstructure (i.e., non-integer h and k) rods are measured and the information contained in the diffuse scattering around the Bragg rods are analyzed in addition to the Bragg rods used for COBRA.

Access to Synchrotron Sources

The limited availability of synchrotron sources for the diffraction measurements is the main drawback for the wide utilization of the COBRA method. The precision required for these measurements means that a good fraction of the beam time obtained is spent in alignment alone. The new research directions developed in this dissertation have helped to propel the application of COBRA techniques at several locations in the US and around the world, including Argonne National Labs, Oak Ridge National Lab, and the Swiss Light Source. As more facilities are developing dedicated beamline for surface diffraction experiments, this accessibility is becoming less of an issue.

Long scan times

The collection of a set of Bragg rods for one sample currently takes between 12-24 hours. About 50% of the measurement time is dead time spent inserting filters

and moving the sample and the detector. The use of filters are required to due to the large dynamic range (> 5 orders of magnitude) along the Bragg rods. Possible setups to speed up the insertion and removal of filters such as mounting the filters on a motorized wheel instead of the current pneumatic system which is currently used, would greatly speed up the data collection time.

7.3 Future Directions

Other Systems

By demonstrating the power of the anomalous-COBRA method in investigating non-planar systems and alloyed systems, the door has now been opened to study a wide range of systems including quantum wire structures and other capped structures.

The presence of an overlayer significantly modifies the strain and composition of the buried nanostructures and it would be interesting to image their structure using a-COBRA. The added complexity in analyzing such a system would be that the folded structure would include the both the nanostructures and the capping material between them.

X-ray Microfocusing and Single Dot Studies

While much can be learned from studying ensembles of quantum dots, the ability to study individual dots would beneficial in further understanding the fine structure of the individual dots. This would enable a direct correlation of the structure of the dots to the results obtained on single-dot optical measurement[94, 95]. This is important for studying the uniformity of QD structures: uniform size distribution would greatly aid in applications such a quantum information processing which require well defines electronic states from the confinement of the electronic wavefunction.

Using advanced x-ray microfocusing techniques and higher brilliant sources such as the Free Electron Laser coming online at the Linac Coherent Light Source (LCLS)[96] the study of individual dots would be possible.

In-situ studies

In-situ studies a-COBRA during the growth would provide invaluable information in understanding the dynamics involved in the growth of these systems.

Direct Phase Measurements?

The quest still continues in finding a truly direct and fast way to retrieve lost x-ray phases from measured diffraction intensities. The COBRA method has proven to be a reliable method for epitaxial systems, however, more work needs to be directed at developing techniques for non-epitaxial systems. A possible approach would be to directly determine the phases by measuring at multiple wavelengths in the vicinity of the resonant edges of the system where there are significant changes in both the real and the imaginary parts of the atomic scattering factor (note that the current study only considers the change in the real part of the scattering factors). Theoretically, the phases can be directly determined in this situation, however, very stringent requirements are required in measuring the intensities and correcting the background to less than a few percent error.

7.4 Final Conclusions

By studying a wider range of growth conditions for these nano-structures, the hope is that a more comprehensive and general theoretical framework may be obtained to fully understand how they form and function. The detailed atomic scale structure a-COBRA provides would serve as invaluable input for semi-empirical and an ab-

initio theoretical calculations of strain relaxation in highly strained systems and would provide a more accurate way of explaining and predicting the opto-electronic properties of these systems.

BIBLIOGRAPHY

BIBLIOGRAPHY

[1] Y. Yacoby, M. Sowwan, E. Stern, J.O. Cross, D. Brewe, R. Pindak, J. Pitney, E. M. Dufresne, and R. Clarke. Direct determination of epitaxial interface structure in Gd_2O_3 passivation of GaAs. *Nature Materials*, 1:99–101, October 2002.

[2] P. B. Joyce, T. J. Krzyzewski, G. R. Bell, B. A. Joyce, and T. S. Jones. Composition of InAs quantum dots on GaAs(001)Direct evidence for (In,Ga)As alloying. *Physical Review B*, 58(24):981, December 1998.

[3] P. M. Petroff and S. P. DenBaars. MBE and MOCVD Growth and Properties of Self-Assembling Quantum Dot Arrays in III-V Semiconductor Structures. *Superlattices and Microstructures*, 15(1):15, 1994.

[4] J.Y. Lee and C. Pearson and J.M. Millunchick. InGaAs/GaAs morphology. *Journal of Applied Physics*, 103:104309, 2008.

[5] A.D. Yoffe. Semiconductor quantum dots and related systems: electronic, optical, luminescence and related properties of low dimensional systems. *Advances in Physics*, 50(1):1–208, JAN 2001.

[6] H.T. Jiang and J. Singh. Self-assembled semiconductor structures: Electronic and optoelectronic properties. *IEEE Journal Of Quantum Electronics*, 34(7):1188–1196, JUL 1998.

[7] C.S. Lent and P.D. Tougaw. Device architecture for computing with quantum dots. *Proceedings of IEEE*, 85(4):541–557, APR 1997.

[8] V. Cerletti, W.A. Coish, O. Gywat, and D. Loss. Recipes for spin-based quantum computing. *Nanotechnology*, 16(4):R27–R49, APR 2005.

[9] D.M.T. Kuo and Y.C. Chang. Tunneling current and emission spectrum of a single-electron transistor under optical pumping. *Physical Review B*, 72(8):085334, AUG 2005.

[10] E. G. Emiroglu, D. G. Hasko, and D. A. Williams. Isolated double quantum dot capacitively coupled to a single quantum dot single-electron transistor in silicon. *Applied Physics Letters*, 83(19):3942–3944, 2003.

[11] W.H. Chang, W.Y. Chen, H.S. Chang, T.P. Hsieh, J.I. Chyi, and T.M. Hsu. Efficient single-photon sources based on low-density quantum dots in photonic-crystal nanocavities. *Physical Review Letters*, 96(11):117401, MAR 24 2006.

[12] S. Kako, C. Santori, K. Hoshino, S. Goetzinger, Y Yamamoto, and Y. Arakawa. A gallium-nitride single-photon source operating at 200K. *Nature Materials*, 5(11):887–892, NOV 2006.

[13] S. Franchi, G. Trevisi, L. Seravalli, and P. Frigeri. Quantum dot nanostructures and molecular beam epitaxy. *Progress in Crystal Growth and Characterization of Materials*, 47:166–195, 2003.

[14] Z. Mi, J. Yang, P. Bhattacharya, P. K. L. Chan, and K. P. Pipe. High performance self-organized InGaAs quantum dot lasers on silicon. *Journal of Vacuum Science and Technology B*, 24(3):1519, 2006.

[15] P. Bhattacharya, D. Klotzkin, O. Qasaimeh, W. Zhou, S. Krishna, and D. Zhu. High-speed modulation and switching characteristics of In(Ga)AsAl(Ga)As self-organized quantum-dot lasers. *IEEE Journal Of Selected Topics In Quantum Electronics*, 6(3):426, May 2000.

[16] P. Guyot-Sionnest. Quantum dots: A new quantum state? *Nature Materials*, 4(9):653–654, SEP 2005.

[17] G. Wei and S.R. Forrest. Intermediate-band solar cells employing quantum dots embedded in an energy fence barrier. *Nano Letters*, 7(1):218–222, 2007.

[18] A. Luque and A. Martí. Increasing the efficiency of ideal solar cells by photon induced transitions at intermediate levels. *Physical Review Letters*, 78(26):5014–5017, Jun 1997.

[19] D. Zhi, H. Davock, R. Murray, C. Roberts, T.S. Jones, D.W. Pashley, P.J. Goodhew, and B.A. Joyce. Quantitative compositional analysis of InAs/GaAs quantum dots by scanning transmission electron microscopy. *Journal of Applied Physics*, 89:2079, 2001.

[20] I. Kegel, T. H. Metzger, A. Lorke, J. Peisl, J. Stangl, G. Bauer, J. M. Garca, and P. M. Petroff. Nanometer-Scale Resolution of Strain and Interdiffusion in Self-Assembled $InAs/GaAs$ Quantum Dots. *Physical Review Letters*, 85(8):1694, August 2000.

[21] I. Kegel, T. H. Metzger, P. Fratzl, J. Peisl, A. Lorke, J. M. Garcia, and P. M. Petroff. Interdependence of strain and shape in self-assembled coherent inas islands on gaas. *Europhysics Letters*, 45(2):222–227, 1999.

[22] Ch. Heyn, A. Bolz, T. Maltezopoulos, R.L. Johnson, and W. Hansen. Ga/In-intermixing and segregation during InAs quantum dot formation. *Journal of Crystal Growth*, 251(1-4):140 – 144, 2003.

[23] Ch. Heyn and W. Hansen. Intermixing in self-assembled InAs quantum dot formation. *Journal of Crystal Growth*, 278(1-4):46 – 50, 2005.

[24] J.A. Venables. Atomic processes in crystal growth. *Surface Science*, 299-300:798 – 817, 1994.

[25] R. Koch. The Intrinsic Stress Of Polycrystalline And Epitaxial Thin Metal-Films. *Journal Of Physics-Condensed Matter*, 6(45):9519–9550, NOV 7 1994.

[26] S.C. Seel, C.V. Thompson, S.J. Hearne, and J.A. Floro. Tensile stress evolution during deposition of volmer–weber thin films. *Journal of Applied Physics*, 88(12):7079–7088, 2000.

[27] A. Bhandari, B.W. Sheldon, and S.J. Hearne. Competition between tensile and compressive stress creation during constrained thin film island coalescence. *Journal of Applied Physics*, 101(3):033528, 2007.

[28] N. Koguchi, S. Takahashi, and T. Chikyow. New MBE growth method for InSb quantum well boxes. *Journal of Crystal Growth*, 111(1-4):688 – 692, 1991.

[29] S. Sanguinetti, T. Mano, M. Oshima, T. Tateno, and M. Wakaki N. Koguchi. Temperature dependence of the photoluminescence of InGaAs/GaAs quantum dot structures without wetting layer. *Applied Physics Letters*, 81(16):3067–3069, OCT 14 2002.

[30] D.A. Muller, L.F. Kourkoutis, M. Murfitt, J.H. Song, H.Y. Hwang, J. Silcox, N. Dellby, and O.L. Krivanek. Atomic-scale chemical imaging of composition and bonding by aberration-corrected microscopy. *Science*, 319(5866):1073–1076, FEB 22 2008.

[31] C. M. Schlepütz and R. Herger and P. R. Willmott and B. D. Patterson and O. Bunk and Ch. Brönnimann and B. Henrich and G. Hülsen and E. F. Eikenberry. Improved data acquisition in grazing-incidence X-ray scattering experiments using a pixel detector. *Acta Crystallographica A*, 61:418, 2005.

[32] M. Sowan, Y. Yacoby, J. Pitney, R. MacHarrie, and R. Clarke et. al. Direct atomic structure determination of epitaxially grown films: Gd_2O_3 on $GaAs(100)$. *Physical Review B*, 66(20):205311, 2002.

[33] D.D. Fong, C. Cionca, Y. Yacoby, and G.B. Stephenson. Direct structural determination in ultrathin ferroelectric films by analysis of synchrotron x-ray scattering measurements. *Physical Review B*, 71:144112, 2005.

[34] Codrin Cionca. *Imaging Interfaces in Epitaxial Heterostructures*. PhD thesis, University of Michigan, 2005.

[35] C. N. Cionca, D. A. Walko, Y. Yacoby, C. Dorin, J. Mirecki-Millunchick, and R. Clarke. Interfacial structure, bonding and composition of InAs and GaSb thin films determined using coherent Bragg rod analysis. *Physical Review B*, 75(11):115306, 2007.

[36] P. R. Willmott and S.A. Pauli and R. Herger and C. M. Schlepütz and D. Martoccia and B. D. Patterson and B. Delley and R. Clarke and D. Kumah and C. Cionca and Y. Yacoby. Structural Basis for the Conducting Interface between LaAlO3 and SrTiO3. *Physical Review Letters*, 99(15):155502, 2007.

[37] W.A. Hendrickson. Determination Of Macromolecular Structures From Anomalous Diffraction Of Synchrotron Radiation. *Science*, 254(5028):51–58, OCT 4 1991.

[38] E. Prince, editor. *International Tables for Crystallography,Volume C Mathematical, Physical and Chemical Tables*. International Tables for Crystallography , Vol. C. Springer, 3 edition, 2004.

[39] R. Fung, V. L. Shneerson, P. F. Lyman, S. S. Parihar, H. T. Johnson-Steigelman, and D. K. Saldin. Phase and amplitude recovery and diffraction image generation method: structure of Sb/Au(110)-$\sqrt{3}$ x $\sqrt{3}$ R54.7 degrees from surface X-ray diffraction. *Acta Crystallographica Section A*, 63(Part 3):239–250, MAY 2007.

[40] O. Bunk. PhD thesis.

[41] R. Herger, P. R. Willmott, O. Bunk, C. M. Schlepütz, B. D. Patterson, and B. Delley. Surface of strontium titanate. *Physical Review Letters*, 98(7):076102, 2007.

[42] V. Elser. Solution of the crystallographic phase problem by iterated projections. *Acta Crystallographica A*, 59(Part 3):201–209, MAY 2003.

[43] T. Walther, A. G. Cullis, D. J. Norris, and M. Hopkinson. Nature of the Stranski-Krastanow Transition during Epitaxy of InGaAs on GaAs. *Physical Review Letters*, 86(11):2381, March 2001.

[44] E. Pehlke, N. Moll, A. Kley, and M. Scheffler. Shape and stability of quantum dots. *Applied Physics A*, 65:525, August 1997.

[45] B. Lita, R. S. Goldman, J. D. Phillips, and P. K. Bhattacharya. Interdiffusion and surface segregation in stacked self-assembled InAs/GaAs quantum dots. *Applied Physics Letters*, 75(18):2797, November 1999.

[46] R. Notzel. Self-organized growth of quantum-dot structures. *Semiconductor Science and Technology*, 11:1365–1379, June 1996.

[47] N. Grandjean and J. Massies. Epitaxial growth of highly strained $In_xGa_{1-x}As$ on GaAs(100): the role of surface diffusion length. *Journ. of Cryst. Growth*, 134:51, 1993.

[48] J. M. Moison, F. Houzay, F. Barthe, L. Leprince, E. Andre, and 0. Vatel. Self-organized growth of regular nanometer-scale InAs dots on GaAs. *Applied Physics Letters*, 64(2):196, January 1994.

[49] M.S. Skolnick and D.J. Mowbray. Recent developments in the physics and applications of self-assembled quantum dots. *Physica E*, (21):155 163, 2004.

[50] J. Tersoff, C. Teichert, and M. G. Lagally. Self-organization in growth of quantum dot superlattices. *Physical Review Letters*, 76(10):1675, March 1996.

[51] J. Tersoff. Enhanced Nucleation and Enrichment of Strianed-Alloy Quantum Dots. *Physical Review Letters*, 81(15):3183, October 1998.

[52] M. Galluppi, A. Frova, M. Capizzia, F. Boscherini, P. Frigeri, S. Franchi, and A. Passaseo. Atomic equilibrium concentrations in (InGa)As quantum dots. *Applied Physics Letters*, 78(20):3122, May 2001.

[53] A. Rosenauer, D. Gerthsen, D. Van Dyck, M. Arzberger, G. Bohm, and G. Abstreiter. Quantification of segregation and mass transport in $In_xGa_{1-x}As/GaAs$ Stranski-Krastanow layers. *Physical Review B*, 64(24):245334, 2001.

[54] N. Liu, J. Tersoff, O. Baklenov, Jr. A. L. Holmes, and C. K. Shih. Nonuniform Composition Profile in In0.5Ga0.5As Alloy Quantum Dots. *Physical Review Letters*, 84(2):334, January 2000.

[55] J. H. Blokland, M. Bozkurt, J. M. Ulloa, D. Reuter, A. D. Wieck, P. M. Koenraad, P. C. M. Christianen, and J. C. Maan. Ellipsoidal InAs quantum dots observed by cross-sectional scanning tunneling microscopy. *Applied Physics Letters*, 94(2):023107, 2009.

[56] O. V. Kolosov, C. D. Marsh M. R. Castell, G. D. Briggs, T. I. Kamins, and R. S. Williams. Imaging the Elastic Nanostructure of Ge Islands by Ultrasonic Force Microscopy. *Physical Review Letters*, 81(5):1046, 1998.

[57] J. Stangl, V. Holy, and G. Bauer. Structural properties of self-organized semiconductor nanostructures. *Review of Modern Physics*, 76(3):725, July 2004.

[58] I. K. Robinson, I. A. Vartanyants, G. J. Williams, M. A. Pfeifer, and J.A. Pitney. Reconstruction of the Shapes of Gold Nanocrystals Using Coherent X-Ray Diffraction. *Physical Review Letters*, 87(19):195505, November 2001.

[59] S. Shusterman, A. Raizman, A. Sher, Y. Paltiel, A. Schwarzman, E. Lepkifker, and Y. Rosenwaks. Nanoscale mapping of strain and composition in quantum dots using kelvin probe force microscopy. *Nano Letters*, 7(7):2089–2093, 2007.

[60] S. Shusterman, Y. Paltiel, A. Sher, V. Ezersky, and Y. Rosenwaks. High-density nanometer-scale InSb dots formation using droplet heteroepitaxial growth by MOVPE. *Journal of Crystal Growth*, 291:363, 2006.

[61] Y. Suzuki and A. Takeuchi and H. Takano and H. Takenaka. Performance test of fresnel zone plate with 50nm outermost zone width in hard x-ray region. *Japanese Journal of Applied Physics*, 44(4A):1994, 2005.

[62] O. Hignette, P. Cloetens, G. Rostaing, P. Bernard, and C. Morawe. Efficient sub 100 nm focusing of hard x rays. *Review of Scientific Instrumentation*, 76(6):63709, 2005.

[63] H. C. Kang, J. Maser, G. B. Stephenson, C. Liu, R. Conley, A. T. Macrander, and S. Vogt. Nanometer linear focusing of hard x rays by a multilayer laue lens. *Physical Review Letters*, 96(12):127401, March 2006.

[64] E.F. Eikenberry, C. Bronnimann, G. Hulsen, H. Toyokawa, R. Horisberger, B. Schmitt, C. Schulze-Briese, and T. Tomizaki. PILATUS: a two-dimensional X-ray detector for macromolecular crystallography. *Nuclear Instruments & Methods In Physics Research Section A-Accelerators Spectrometers Detectors And Associated Equipments*, 501(1):260–266, MAR 21 2003. 10th International Workshop on Vertex Detectors, BRUNNEN, SWITZERLAND, SEP 23-28, 2001.

[65] Y. Yacoby and M. Sowwan and E. Stern and J. O. Cross and D. Brewe and R. Pindak and J. Pitney and E. M. Dufresne and R. Clarke. Direct determination of epitaxial interface structure in Gd2O. *Nature Materials*, 1:99, 2002.

[66] Krapf, P. and Robach, Y. and Gendry, M. and Porte, L. Influence of step edges elastic relaxation on the morphology of compressively and tensilely strained In1- xGaxAs layers epitaxially grown on InP. *Journal of Crystal Growth*, 181(4):337, April 1997.

[67] Gendry, M. and Grenet, G. and Robach, Y. and Krapf, P. and Porte, L. and Hollinger, G. . Role of surface energy and surface reconstructions on the 2D-to-3D growth-mode transition of strained $InxGa1 - xAs$ layers on InP(001). *Physical Review B*, 56(15):9271–9274, Oct 1997.

[68] R.J. Asaro and W.A. Tiller. Interface Morphology Development During Stress-Corrosion Cracking Via Surface Diffusion. *Metallurgical Transactions*, 3(7):1789, 1972.

[69] N. Grandjean and J. Massies and O. Tottereau. Surface segregation in (Ga,In)As/GaAs quantum boxes. *Physical Review B*, 55(16):10189–10192, APR 15 1997.

[70] K. Muraki and S. Fukatsu and Y. Shiraki and R. Ito. Surface segregation of In atoms during molecular beam epitaxy and its influence on the energy levels in InGaAs/GaAs quantum wells. *Applied Physics Letters*, 61(5):557–559, 1992.

[71] K. Muraki, S. Fukatsu, Y. Shiraki, and R. Ito. Surface segregation of In atoms and its influence on the quantized levels in InGaAs/GaAs quantum wells. *Journal of Crystal Growth*, 127(1-4):546 – 549, 1993.

[72] M. Hanke and D. Grigoriev and M. Schmidbauer and P. Schäfer and R. Köhler and R. L. Sellin and U. W. Pohl and D. Bimberg. Vertical composition gradient in InGaAs/GaAs alloy quantum dots as revealed by high-resolution x-ray diffraction. *Applied Physics Letters*, 85(15):3062, 2004.

[73] L.N. Coelho and R. Magalhäes-Paniago and A. Malachias and J.G. Zelcovit and M. A. Cotta. Resonant x-ray scattering from self-assembled InP/GaAs(001) islands: Understanding the chemical structure of quaternary quantum dots. *Applied Physics Letters*, 92(2):021903, 2008.

[74] A. Malachias and S. Kycia and G. Medeiros-Ribeiro and R. Magalhães-Paniago and T.I. Kamins and R.S. Williams. 3D Composition of Epitaxial Nanocrystals by Anomalous X-Ray Diffraction: Observation of a Si-Rich Core in Ge Domes on Si(100). *Physical Review Letters*, 91(17):176101, Oct 2003.

[75] C.N. Cionca and A. Riposan and D. P. Kumah and N. S. Husseini and D.A. Walko and Y. Yacoby and J.M. Millunchick and R. Clarke. Strain and composition mapping of epitaxial nanostructures. *Applied Physics Letters*, 92(15):151914, 2008.

[76] Ch. Heyn and A. Bolz and T. Maltezopoulos and R.L. Johnson and W. Hansen. Intermixing in self-assembled InAs quantum dot formation. *Journal of Crystal Growth*, 278:46, 2005.

[77] A. Riposan and J. Mirecki Millunchick and Chris Pearson. Strain mediated reconstructions and indium segregation on InGaAs/GaAs(001) alloy surfaces at intermediate lattice mismatch. *Journal of Vacuum Science and Technology A*, 24(6):2041, 2006.

[78] T. Benabbas and P. François and Y. Androussi and A. Lefebvre. Stress relaxation in highly strained InAs/GaAs structures as studied by finite element analysis and transmission electron microscopy. *Journal of Applied Physics*, 80(5):2763–2767, 1996.

[79] W. Lee, J.M. Myoung, Y.H. Yoo, and H. Shin. Effect of elastic anisotropy on the strain fields and band edges in stacked InAs/GaAs quantum dot nanostructures. *Solid State Communications*, 132(2):135 – 140, 2004.

[80] T. Benabbas, Y. Androussi, and A. Lefebvre. A finite-element study of strain fields in vertically aligned InAs islands in GaAs. *Journal of Applied Physics*, 86(4):1945–1950, 1999.

[81] W. Ye, S. Hanson, M. Reason, X. Weng, and R.S. Goldman. Control of InAs/GaAs quantum dot density and alignment using modified buffer layers. *Journal Of Vacuum Science & Technology B*, 23(4):1736–1740, JUL-AUG 2005. 32nd Annual Conference on the Physic and Chemistry of Semiconductor Interfaces, Bozeman, MT, JAN 23-27, 2005.

[82] D. Kumah, S. Shusterman, Y. Paltiel, Y. Yacoby, and R. Clarke. Droplet epitaxy: the lowdown on quantum dot formation. to be published.

[83] N.N. Faleev, Y.G. Musikhin, A.A. Suvorova, A.Y. Egorov, A.E. Zhukov, A.R. Kovsh, V.M. Ustinov, M. Tabuchi, and Y. Takeda. Anisotropy of the spatial distribution of In(Ga)As quantum dots in In(Ga)As-GaAs multilayer heterostructures studied by x-ray and synchrotron diffraction and transmission electron microscopy. *Semiconductors*, 35(8):932–940, 2001.

[84] N.N. Faleev, A.Y. Egorov, A.E. Zhukov, A.R. Kovsh, S.S. Mikhrin, V.M. Ustinov, K.M. Pavlov, V.I. Punegov, M. Tabuchi, and Y. Takeda. X-Ray diffraction analysis of multilayer InAs-GaAs heterostructures with InAs quantum dots. *Semiconductors*, 33(11):1229–1237, NOV 1999.

[85] N. Koguchi, K. Ishige, and S. Takahashi. New selective molecular-beam-epitaxial growth method for direct formation of GaAs quantum dots. *Journal of Vacuum Science and Technology B*, 11:787–790, 1993.

[86] K.A. Sablon, J.H. Lee, Z. Wang, J.H. Shultz, and G.J. Salamo. Configuration control of quantum dot molecules by droplet epitaxy. *Applied Physics Letters*, 92:203106, 2008.

[87] J. Johansson, L.S. Karlsson, C.P.T. Svensson, T. Martensson, B.A. Wacaser, K. Deppert, L. Samuelson, and W. Seifert. Structural properties of (111)B-oriented III-V nanowires. *Nature Materials*, 5(7):574–580, JUL 2006.

[88] D.J. Eaglesham and M. Cerullo. Dislocation-Free Stranski-Krastanow Growth Of Ge On Si(100). *Physical Review Letters*, 64(16):1943–1946, Apr 16 1990.

[89] Zh. M. Wang, B. L. Liang, K. A. Sablon, and G. J. Salamo. Nanoholes fabricated by self-assembled gallium nanodrill on GaAs(100). *Applied Physics Letters*, 90(11), MAR 12 2007.

[90] N. Koguchi and K. Ishige. Growth Of Gaas Epitaxial Microcrystals On An S-Terminated Gaas Substrate By Successive Irradiation Of Ga And As Molecular-Beams. *Japanese Journal Of Applied Physics Part 1-Regular Papers Short Notes & Review Papers*, 32(5A):2052–2058, MAY 1993.

[91] R. Timm, H. Eisele, A. Lenz, T.Y. Kim, F. Streicher, K. Potschke, U.W. Pohl, D. Bimberg, and M. Dahne. Structure of InAs/GaAs quantum dots grown with Sb surfactant. *Physica E-Low-Dimensional Systems & Nanostructures*, 32(1-2):25–28, MAY 2006. 12th International Conference on Modulated Semiconductor Structures (MSS12), Albuquerque, NM, JUL 10-15, 2005.

[92] Y. Yacoby, C. Brooks, D. Schlom, J. O. Cross, D. A. Walko, C. N. Cionca, N. S. Husseini, A. Riposan, and R. Clarke. Structural changes induced by metal electrode layers on ultrathin BaTiO3 films. *Physical Review B*, 77(19), MAY 2008.

[93] P.W. Fry, I.E. Itskevich, D.J. Mowbray, M.S. Skolnick, J.J. Finley, J.A. Barker, E.P. O'Reilly, L.R. Wilson, I.A. Larkin, P.A. Maksym, M. Hopkinson, M. Al-Khafaji, J.P.R. David, A.G. Cullis, G. Hill, and J.C. Clark. Inverted electron-hole alignment in InAs-GaAs self-assembled quantum dots. *Physical Review Letters*, 84(4):733–736, JAN 24 2000.

[94] R.M. Stevenson, R.J. Young, P. Atkinson, K. Cooper, D.A. Ritchie, and A.J. Shields. A semiconductor source of triggered entangled photon pairs. *Nature*, 439(7073):179–182, JAN 12 2006.

[95] Y. Wu, E.D. Kim, X. Xu, J. Cheng, D.G. Steel, A.S. Bracker, D. Gammon, S.E. Economou, and L. J. Sham. Selective Optical Control of Electron Spin Coherence in Singly Charged GaAs-$Al_{0.3}Ga_{0.7}As$ Quantum Dots. *Physical Review Letters*, 99(9), 2007.

[96] A. Cho. World's first x-ray laser powers up. *ScienceNOW Daily News*, 21 April 2009. online at "http://sciencenow.sciencemag.org/cgi/content/full/2009/421/2?rss=1".